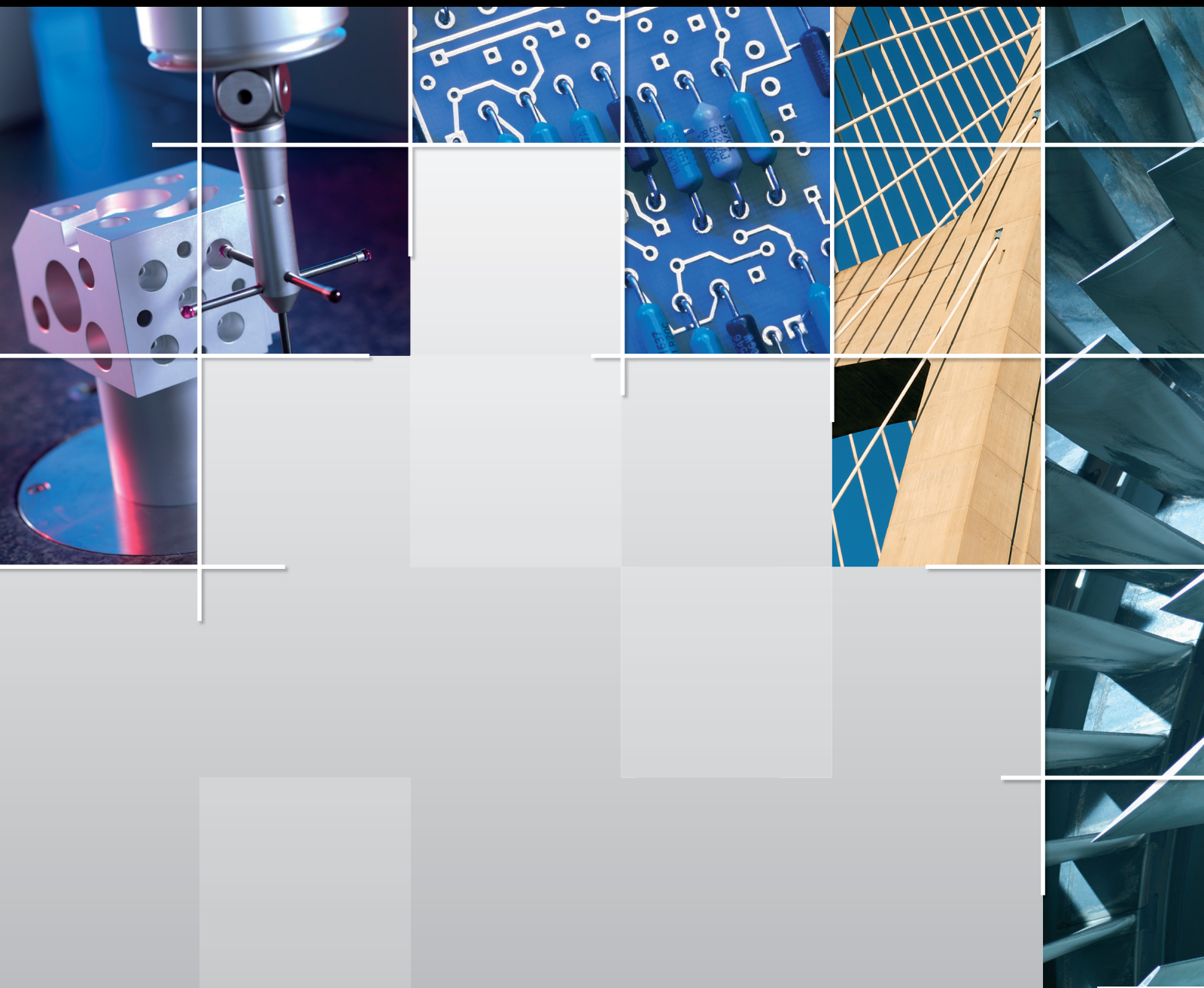


# High Performance Concrete Materials with Applications in Building and Civil Engineering

Guest Editors: Peng Zhang, Song Han, Serina Ng, and Xuhao Wang





---

# **High Performance Concrete Materials with Applications in Building and Civil Engineering**

Journal of Engineering

---

# **High Performance Concrete Materials with Applications in Building and Civil Engineering**

Guest Editors: Peng Zhang, Song Han, Serina Ng,  
and Xuhao Wang



---

Copyright © 2017 Hindawi Publishing Corporation. All rights reserved.

This is a special issue published in “Journal of Engineering.” All articles are open access articles distributed under the Creative Commons Attribution License, which permits unrestricted use, distribution, and reproduction in any medium, provided the original work is properly cited.

## Editorial Board

- H.P.S Abdul Khalil, Malaysia  
M. S. Ab-Rahman, Malaysia  
K. Kwan Ahn, Republic of Korea  
M. Ali, Germany  
Sakir Amiroudine, France  
Panagiota Angeli, UK  
Ibrahim Asi, Jordan  
Francis T. K. Au, Hong Kong  
Eldad J. Avital, UK  
Lavinia Balan, France  
Kantesh Balani, India  
Ibrahim M. Banat, UK  
Uttam C. Banerjee, India  
Alfonso Banos, Spain  
Giuseppe Barbieri, Italy  
Andrzej Bartoszewicz, Poland  
Angelo Basile, Italy  
Giorgio Bellotti, Italy  
Houman Borouchaki, France  
Nizar Bouguila, Canada  
Noureddine Bouhaddi, France  
Christos Bouras, Greece  
Fernando A. Branco, Portugal  
José I. Calvo, Spain  
Marcelo Campo, Argentina  
Jian Cao, China  
Miguel A. Centeno, Spain  
Marko Cepin, Slovenia  
M. Chadli, France  
Gang-Len Chang, USA  
Chung-Liang Chang, Taiwan  
Wen Chen, China  
Guang-Hong Chen, USA  
Jingdong Chen, China  
Weidong Chen, China  
Yongping Chen, China  
Russell C. Chianelli, USA  
Jyh-Horng Chou, Taiwan  
Paolo Colantonio, Italy  
Joaquin Coronas, Spain  
Fu-Zhai Cui, China  
L. D. S. Coelho, Brazil  
Lenore Dai, USA  
Lucian Dascalescu, France  
Pradipta k. Dash, India  
Adil Denizli, Turkey  
Kevser Dincer, Turkey  
Yong Ding, USA  
Guohai Dong, China  
Shad Dowlatshahi, USA  
Wei Du, China  
Mario R. Eden, USA  
F. Ein-Mozaffari, Canada  
Asghar Esmaeeli, USA  
Michael Fairweather, UK  
Mahmood Fathy, Iran  
Hicham Fenniri, Canada  
Mario Ferreira, Portugal  
Paulo Flores, Portugal  
Jerome Fortin, France  
Francesco Frusteri, Italy  
Mohammed K. Gabsi, France  
Maurice Gagnaire, France  
Fabio Galbusera, Germany  
Woon-Seng Gan, Singapore  
Furong Gao, Hong Kong  
Serge Gauthier, France  
Raja Ghosh, Canada  
Ashish Goel, USA  
Mohammed Ashraf Gondal, KSA  
R. S. Goonetilleke, Hong Kong  
Alfio D. Grasso, Italy  
Artyom M. Grigoryan, USA  
Jose M. Guisan, Spain  
Jing-Ming Guo, Taiwan  
Chang Sik Ha, Republic of Korea  
Mohamed Hafidi, Morocco  
Moktar Hamdi, Tunisia  
Oualid Hammi, KSA  
Jie Han, China  
Sang-Min Han, Republic of Korea  
Hai-Chao Han, USA  
Souad Harmand, France  
Toshio Hattori, Japan  
Xiao He, China  
Shuisheng He, UK  
Julio C. Hernandez-Castro, UK  
Hidehiko Higaki, Japan  
Daesik Hong, Republic of Korea  
Jiun-Wei Horng, Taiwan  
Junling Hu, USA  
Ye Huang, UK  
Dongzhou Huang, USA  
Nen-Fu Huang, Taiwan  
Xiaohong Huang, China  
Kang Moo Huh, Republic of Korea  
Yuh-Shyan Hwang, Taiwan  
Mohamed Ichchou, France  
Kamran Iqbal, USA  
Daisuke Ishii, Japan  
Mariatti bt Jaafar, Malaysia  
Radhey S. Jangid, India  
Ping Ji, Hong Kong  
Sheng-Rui Jian, Taiwan  
Long Jiang, USA  
Karim Kabalan, Lebanon  
Yury S. Kachanov, Russia  
Ryutaro Kamijo, Japan  
Toshiyuki Kanamori, Japan  
T. Jin Kang, Republic of Korea  
He-Yau Kang, Taiwan  
Haranath Kar, India  
Abdullah A. Kendoush, USA  
Alireza Khataee, Iran  
Y.A. Khulief, KSA  
D. Ha Kim, Republic of Korea  
Dong-Pyo Kim, Republic of Korea  
Se-Kwon Kim, Republic of Korea  
Sun-il Kim, USA  
Hong Kook Kim, Republic of Korea  
Margaritis Kostoglou, Greece  
Stavros Koubias, Greece  
Zoubeir Lafhaj, France  
Shang-Hong Lai, Taiwan  
Mickaël Lallart, France  
K. C. Lam, Hong Kong  
Ruediger Lange, Germany  
Guy Lauriat, France  
Khoa Le, Australia  
S.-K. Lee, Republic of Korea  
Junhwan Lee, Republic of Korea  
Jungwoo Lee, Republic of Korea  
Gang Li, China  
You-Rong Li, China  
Jerome Z. Liang, USA

H. Liu, China  
Ying-Ling Liu, Taiwan  
Bo Liu, UK  
Tian-Hua Liu, Taiwan  
Justo Lobato, Spain  
Dusan Losic, Australia  
Christophe Loyez, France  
Paul Luckham, UK  
Junhe Ma, USA  
A. S. Madhukumar, Singapore  
Soliman A. Mahmoud, UAE  
Parviz Malekzadeh, Iran  
Pierre-yves Manach, France  
Oronzio Manca, Italy  
Alessandro Marzani, Italy  
Claudio Mazzotti, Italy  
Yuezhong Meng, China  
Ahmed Mezrhab, Morocco  
Aki Mikkola, Finland  
Gabriele Milani, Italy  
Geyong Min, UK  
Hossein Moayedi, Iran  
S. Ali A. Moosavian, Iran  
Franck Morfin, France  
Vasily Moshnyaga, Japan  
Daniela Munteanu, France  
Dmitry Murzin, Finland  
Masato Nagata, Japan  
Salah Naili, France  
Paul Nancarrow, UK  
Krishnaswamy Nandakumar, USA  
D. Na-Ranong, Thailand  
Sergio Nardini, Italy  
C. Nataraj, USA  
Rufino M. Navarro, Spain  
Yi-Qing Ni, Hong Kong  
Wei Ni, Australia  
Hong Nie, USA  
Li Niu, China  
Hidetaka Noritomi, Japan  
Makoto Obata, Japan  
Kwang Oh, USA  
Haruhiko Ohta, Japan  
Homayoon Oraizi, Iran  
Belkacem Ould Bouamama, France  
Puren Ouyang, Canada  
E. Palaneeswaran, Australia  
Kannappan K. Palaniappan, USA  
Issa Panahi, USA  
Sreekanth Pannala, USA  
Lazaros G. Papageorgiou, UK  
Jong M. Park, Republic of Korea  
Pedro Peris-Lopez, Spain  
Samuel Pierre, Canada  
Chin Ping Tan, Malaysia  
Sofie Pollin, Belgium  
Gang Qian, USA  
J. Manuel R.S. Tavares, Portugal  
Luis Carlos Rabelo, USA  
Mohamed Rachik, France  
Navin K. Rastogi, India  
Giuseppe Ricci, Italy  
Yong Man Ro, Republic of Korea  
Damien C. Rodger, USA  
Hyun Seog Roh, Republic of Korea  
Sergio Rojas, Spain  
Elsa de Sá Caetano, Portugal  
Ziad Saghir, Canada  
Gokhan Sahin, USA  
Konstantinos Salonitis, UK  
Abdülkadir Sezai Sarac, Turkey  
Sami Sayadi, Tunisia  
Pierre Schaetzel, France  
Christophe A. Serra, France  
Éric Serre, France  
Amy Shen, USA  
Li Shi, China  
Jonathan Shi, USA  
Kuei-Ping Shih, Taiwan  
Georgiy B. Shul'pin, Russia  
Jyoti Sinha, UK  
Ray W. Snidle, UK  
Liming Song, China  
M'hamed Souli, France  
E. Specht, Germany  
Bao-Lian Su, Belgium  
Hang Su, USA  
Runcang Sun, China  
Bhimappa Suresha, India  
Lakhdar Taleb, France  
C. M. Tam, China  
Daniele Tarchi, Italy  
Jerome Thibonnet, France  
Sébastien Thomas, France  
İlker Bekir Topçu, Turkey  
Jiyuan Tu, Australia  
Gülfem Tuzkaya, Turkey  
Ugur Tuzun, UK  
Minoru Uehara, Japan  
Yoshio Utaka, Japan  
Guy A. E. Vandenbosch, Belgium  
A. Vanelli-Coralli, Italy  
M. Ahmer Wadee, UK  
Shaobin Wang, Australia  
Fei Wang, China  
Bing Wang, China  
Qudong Wang, China  
Laurence R. Weatherley, USA  
WaiKeung Wong, Hong Kong  
Chuan-Yu Wu, UK  
Xiaodong Wu, China  
Chase Wu, USA  
Renbiao Wu, China  
Wenchuan Wu, China  
Shuo-Jye Wu, Taiwan  
He Xia, China  
Tian Xia, USA  
Huining Xiao, Canada  
Guangming Xie, China  
Zhichuan Xu, USA  
René Yamapi, Cameroon  
Mo Yang, Hong Kong  
Yanhui Yang, Singapore  
Yaowen Yang, Singapore  
Fan Yang, France  
Ching-Chow Yang, Taiwan  
Davood Younesian, Iran  
Zhong-Yong Yuan, China  
YoungSu Yun, Republic of Korea  
Yonghong Zeng, Singapore  
Jiujun Zhang, Canada  
Zhibing Zhang, UK  
Guangjun Zhang, China  
Lihong Zhang, Canada  
Wei-Qiang Zhang, China  
Xuejing Zheng, China  
Jianjun Zheng, China  
Minghua Zhou, China  
Zhi Zhou, China  
Jie Zhou, China  
Yuanxin Zhou, USA

# Contents

---

**High Performance Concrete Materials with Applications in Building and Civil Engineering**

Peng Zhang, Song Han, Serina Ng, and Xu-Hao Wang  
Volume 2017, Article ID 8161026, 3 pages

**Model of the Mechanical Behavior of Cementitious Matrices Reinforced with Nanomaterials**

Victor D. Balopoulos, Nikolaos Archontas, and Stavroula J. Pantazopoulou  
Volume 2017, Article ID 7329540, 10 pages

**Flexural Behavior of High-Volume Steel Fiber Cementitious Composite Externally Reinforced with Basalt FRP Sheet**

Seungwon Kim and Cheolwoo Park  
Volume 2016, Article ID 2857270, 9 pages

**Bending and Shear Experimental Tests and Numerical Analysis of Composite Slabs Made Up of Lightweight Concrete**

F. P. Alvarez Rabanal, J. Guerrero-Muñoz,  
M. Alonso-Martinez, and J. E. Martinez-Martinez  
Volume 2016, Article ID 6819190, 10 pages

***In Situ* Determination of the Transport Properties of Near-Surface Concrete Using AC Impedance Spectroscopy Techniques**

Lipeng Wu, Peng Dai, and Yong Li  
Volume 2016, Article ID 6547391, 7 pages

**The Hysteresis Performance and Restoring Force Model for Corroded Reinforced Concrete Frame Columns**

Guifeng Zhao, Meng Zhang, Yaoliang Li, and Dawang Li  
Volume 2016, Article ID 7615385, 19 pages

**Determination of the Transport Properties of Structural Concrete Using AC Impedance Spectroscopy Techniques**

Lipeng Wu, Peng Dai, and Yong Li  
Volume 2016, Article ID 2630186, 8 pages

**The Mechanical Properties of the Concrete Using Metakaolin Additive and Polymer Admixture**

Adel Al Menhosh, Yan Wang, and Yu Wang  
Volume 2016, Article ID 1670615, 6 pages

**An Improved Micromechanical Framework for Saturated Concrete Repaired by the Electrochemical Deposition Method considering the Imperfect Bonding**

Qing Chen, Zhengwu Jiang, Hehua Zhu, J. Woody Ju, Zhiguo Yan, and Yaqiong Wang  
Volume 2016, Article ID 1894027, 11 pages

## Editorial

# High Performance Concrete Materials with Applications in Building and Civil Engineering

**Peng Zhang,<sup>1</sup> Song Han,<sup>2</sup> Serina Ng,<sup>3</sup> and Xu-Hao Wang<sup>4</sup>**

<sup>1</sup>*School of Water Conservancy and Environment Engineering, Zhengzhou University, Zhengzhou 450001, China*

<sup>2</sup>*School of Civil Engineering, Beijing Jiaotong University, Beijing 100044, China*

<sup>3</sup>*Department of Materials and Structures, SINTEF Building and Infrastructure, 7465 Trondheim, Norway*

<sup>4</sup>*National Concrete Pavement Technology Center, Iowa State University, Ames, IA 50011, USA*

Correspondence should be addressed to Peng Zhang; [zhangpeng@zzu.edu.cn](mailto:zhangpeng@zzu.edu.cn)

Received 9 March 2017; Accepted 20 March 2017; Published 19 April 2017

Copyright © 2017 Peng Zhang et al. This is an open access article distributed under the Creative Commons Attribution License, which permits unrestricted use, distribution, and reproduction in any medium, provided the original work is properly cited.

Concrete materials are the most widely used and most consumable building material in the world and have grown tremendously in recent years due to the high strength, high elasticity modulus, well plasticity, and workability. The development tendency of the modern civil engineering structures is high strength, high rise, and long design lifetime, which has higher requirements on concrete. High performance concrete can be defined as the concrete that can meet special combinations of properties and uniformity requirements, which can not always be achieved routinely using traditional raw materials and conventional mixing, placing, and curing methods [1]. The development of high performance concrete materials, especially the ultra high performance concrete, will provide better materials for specific projects in civil engineering. Compared with the traditional concrete, high performance concrete materials have more excellent mechanical properties and durability, and the use of them in civil engineering is becoming more and more wide [2]. A large number of researchers are targeting developments of high performance concrete and also working on the mechanism research for special properties, preparation technology, testing methods, modeling, and applications of various high performance building materials. Generally, there are many ways to get high performance concrete. Usually, special aggregates, binding materials, and admixtures can be added to the traditional concrete to obtain high performance concrete. For example, some unconventional aggregates [3], mineral admixtures [4],

chemical admixtures [5], and different fibers [6] can be used to produce high performance concrete.

This special issue aims to bring researchers from academia and industry together to report and explore the new preparation methods, new investigations techniques, material properties, and applications in high performance concrete materials and review the latest progress in this field. Out of about seventeen submissions, eight research manuscripts have been selected and included in this special issue because of their good quality and relevance to the theme. The selected articles address various aspects, including an improved micromechanical framework with interfacial transition zone (ITZ) for saturated concrete repaired by the electrochemical deposition method, bending and shear properties of composite slabs made up of lightweight concrete, transport properties of high performance concrete based on AC impedance spectroscopy techniques, flexural properties of steel fiber cementitious composite externally reinforced with basalt FRP sheet, transport properties of near-surface concrete, a model of mechanical properties of nanomaterials reinforced cementitious composites, hysteresis properties and a restoring force model for corroded reinforced concrete frame columns, and mechanical properties of high performance concrete containing metakaolin and polymer admixture.

The paper titled “An Improved Micromechanical Framework for Saturated Concrete Repaired by the Electrochemical Deposition Method Considering the Imperfect Bonding” is

authored by Q. Chen et al. They provided an improved micromechanical framework with interfacial transition zone in order to explain the deposition healing process with micromechanics for saturated concrete. To predict the effective performance of repaired concrete taking the interfacial transition zone effect into account, the new multilevel homogenization schemes were adopted. They also proposed the modification process in reaching the high performance of repaired concrete under dry condition. The comparison of the prediction results gained from the improved model provided in this paper and the results gained from other current models have been carried out to illustrate the reasonability of the improved micromechanical model. Furthermore, the authors discussed the effects of the deposition product and interfacial transition zone on the effectiveness of healing.

The paper titled "Bending and Shear Experimental Tests and Numerical Analysis of Composite Slabs Made Up of Lightweight Concrete" is authored by F. P. A. Rabanal et al. Through a series of m-k experiments with advanced techniques and the numerical simulations on flexural properties of composite slabs with two lengths, which are made of three kinds of lightweight concrete and steel, they investigated the structural strengths of the composite slabs. Based on the test results, the dimensionless coefficients were obtained to compare the effect of different sizes of the slabs on the structural performance. Moreover, the finite element methods were used to perform the nonlinear numerical simulations applying four various multilinear isotropic hardening laws. The friction coefficient between the concrete and steel was modeled using coulomb friction contact. The results indicate that the numerical results are very consistent with the results of the experiments; as a result the numerical models established in this paper can be applied in improving and optimizing the composite slabs produced with lightweight concrete.

The paper titled "Determination of the Transport Properties of Structural Concrete Using AC Impedance Spectroscopy Techniques" is authored by L. Wu et al. They measured the chloride ion diffusion coefficient of high performance concrete using AC impedance spectroscopy technology to investigate the transport performance of high performance concrete. By adopting the equivalent circuit model, they also deduced the relationship between the chloride ion diffusion coefficient and mesostructure parameters and proposed a diffusion coefficient determining measure using AC impedance spectroscopy technique. The results showed that the chloride ion diffusion coefficient could be amended when considering the conductivity difference resulting by different cementitious materials. The comparison of ASTM C1202 method and the method presented in this paper indicated that there is a linear correlation between the two methods due to the fact that the method of ASTM C1202 is affected by the pore solution conductivity, which has small influence on the chloride ion diffusion performance of the concrete compared to the interconnected porosity.

S. Kim and C. Park conducted a study on the flexural properties of basalt FRP externally reinforced high performance cementitious composites containing steel fibers with the volume content of 8%. Their paper is titled "Flexural

Behavior of High-Volume Steel Fiber Cementitious Composite Externally Reinforced with Basalt FRP Sheet." Based on the study results, it is noted that the best reinforcement method of the basalt fiber sheet to the beam structures among the methods mentioned in this paper is single-layered 45° oriented method, and the maximum load ratio can not be increased consequentially with the increase of the layers and thickness of BFRP materials. It can also be concluded that the toughness and strength of the beam could be increasing with the increase of the ductility of the constraint.

L. Wu et al. presented an appropriate method to determine chloride ion diffusion coefficient suitable for in situ, which was based on the relationship between the chloride ion diffusion coefficient and the alternating current impedance spectroscopy parameters. Their paper is titled "In Situ Determination of the Transport Properties of Near-Surface Concrete Using AC Impedance Spectroscopy Techniques." The proposed method well reflects the transport performance of the near-surface concrete and the reinforcing bar will not have any effect on this method. Their experiment results indicate that the new method is exactly consistent with "PERMIT" migration test and it can save more measuring time compared to the traditional method.

The paper titled "Model of the Mechanical Behavior of Cementitious Matrices Reinforced with Nanomaterials" is authored by V. D. Balopoulos et al. They developed a mechanistic computational model to assess the restriction function of the nanoparticles to reinforce the gel microstructure under the common stress state. In order to assess the influence of the reinforcement of the nanomaterials on the phenomenological performance of the composites, the composites were investigated under different common stress states applying the model proposed. The application results show that the modeling process chosen in this study can successfully copy the known tendency in mechanical performance of cementitious composites, which covers the sensitivity of the yield and failure stress to the transverse restriction and the ratio of uniaxial tensile and compression strength.

G. Zhao et al. conducted a numerical simulation of the hysteresis properties of corroded reinforced concrete frame columns. Their paper is titled "The Hysteresis Performance and Restoring Force Model for Corroded Reinforced Concrete Frame Columns." Based on the numerical simulation, the authors established a retrogressive three-linearity restoring force model, which well reflected the hysteresis properties of corroded reinforced concrete frame columns. The analysis indicates that the hysteretic bearing capacity of the frame columns greatly reduces because of the corrosion of the steel rebar. From the hysteresis curves obtained by the model established in this study, it can be concluded that there is similar characters to those of the experimental curves, which proves that the restoring force model founded in this study is accurate, rational, applicable, and simple in usage.

The paper titled "The Mechanical Properties of the Concrete Using Metakaolin Additive and Polymer Admixture" is authored by A. Al Menhosh et al. They reported the influence of the blended addition of polymer and metakaolin on the durability and the mechanical performance of high

performance concrete. In their investigation, various dosages of metakaolin, polymers, and recycled fibers were used as the combinations. Moreover, the influence of curing methods and water to cement ratio on mechanical performance was revealed, and the optimal mix proportion was suggested based on the experiments. The results indicate that the addition of metakaolin can accelerate the setting time of concrete but reduce the flowability of fresh concrete, and the inclusion of plastic and glass fibers obviously enhances the tensile strength of the concrete. The combination of 15% metakaolin and 5% optimal polymer can produce the concrete exhibiting wonderful strength and durability.

## Acknowledgments

We would like to thank the authors who have submitted manuscripts to this special issue. We would also like to acknowledge the referees who have put in the hard work and their valuable time to review each paper in a timely and professional way. The lead editor thanks all the editors for their contribution in reviewing and assigning reviews for the submitted manuscripts.

Peng Zhang  
Song Han  
Serina Ng  
Xu-Hao Wang

## References

- [1] B. J. Olawuyi and W. P. Boshoff, "Influence of SAP content and curing age on air void distribution of high performance concrete using 3D volume analysis," *Construction and Building Materials*, vol. 135, pp. 580–589, 2017.
- [2] P. Zhang, C. Liu, and Q. Li, "Application of gray relational analysis for chloride permeability and freeze-thaw resistance of high-performance concrete containing nanoparticles," *Journal of Materials in Civil Engineering*, vol. 23, no. 12, pp. 1760–1763, 2011.
- [3] N. Flores Medina, D. Flores-Medina, and F. Hernández-Olivares, "Influence of fibers partially coated with rubber from tire recycling as aggregate on the acoustical properties of rubberized concrete," *Construction and Building Materials*, vol. 129, pp. 25–36, 2016.
- [4] P. Zhang, Q.-Y. Guan, C.-H. Liu, and Q.-F. Li, "Study on notch sensitivity of fracture properties of concrete containing nano-SiO<sub>2</sub> particles and fly ash," *Journal of Nanomaterials*, vol. 2013, Article ID 381682, 7 pages, 2013.
- [5] R. Zhang, Q. Wang, L. Ma, Y. Yang, and L. Qi, "Effect of interaction between expanding agent proportion and stress ratio on creep characteristics of concrete filled steel tube," *Journal of Central South University (Science and Technology)*, vol. 45, no. 7, pp. 2416–2423, 2014.
- [6] P. Zhang and Q.-F. Li, "Effect of polypropylene fiber on durability of concrete composite containing fly ash and silica fume," *Composites Part B: Engineering*, vol. 45, no. 1, pp. 1587–1594, 2013.

## Research Article

# Model of the Mechanical Behavior of Cementitious Matrices Reinforced with Nanomaterials

Victor D. Balopoulos,<sup>1</sup> Nikolaos Archontas,<sup>2</sup> and Stavroula J. Pantazopoulou<sup>3</sup>

<sup>1</sup>*Civil Engineering Department, Democritus University of Thrace (DUTH), Xanthi, Greece*

<sup>2</sup>*Department of Civil & Environmental Engineering, University of Cyprus, Nicosia, Cyprus*

<sup>3</sup>*Civil Engineering Department, The Lassonde School of Engineering, York University, Toronto, ON, Canada*

Correspondence should be addressed to Victor D. Balopoulos; vbalop@civil.duth.gr

Received 23 September 2016; Accepted 19 February 2017; Published 20 March 2017

Academic Editor: Peng Zhang

Copyright © 2017 Victor D. Balopoulos et al. This is an open access article distributed under the Creative Commons Attribution License, which permits unrestricted use, distribution, and reproduction in any medium, provided the original work is properly cited.

CNTs and CNFs have been introduced as a nanoscale reinforcing material to cementitious composites, for stiffening and strengthening the microstructure. This technology is motivated by the need to control crack initiation in the cementitious gel before it propagates into visible crack formations. Experimental evidence supports this concept; however, testing at the nanoscale may only be conducted through nanoindentation, which has a limited range only providing localized results that cannot be extrapolated to general stress states. To evaluate the restraining action of nanomaterials in the gel microstructure, a computational mechanistic model has been developed where the material phases (gel, nanotubes, and pores) are modeled explicitly allowing for natural randomness in their distribution and orientation. Repeated analysis with identical input data reproduces the statistical scatter observed in laboratory tests on identical material samples. The formulation uses a discrete element approach; the gel structure is represented by a random network of hydrates and successfully reproduces the known trends in mechanical behavior of cementitious materials (pressure and restraint sensitive material behavior) and the small ratio of tensile to compressive strength. Simulations illustrate that it is possible to computationally reproduce the measured properties and behavior of fiber-reinforced cement composites using information from simple laboratory tests.

## 1. Introduction

New generations of functionally graded cementitious materials have emerged in recent years designed to meet specific performance objectives. These developments in the materials technology open up the prospects of a new era in construction, where the traditional concrete will be displaced in favor of more durable cementitious materials that possess higher fracture energy and are resilient to tensile deformation. An important milestone towards this objective is the new generation of fiber-reinforced matrices that contain a hybrid mix of fibers as a means to enhance the performance through the synergistic effects imparted by the various types of fibers functioning at the various scales of the FRC microstructure [1]. Hybrid mixes usually contain a cocktail of fibers of different materials (synthetic or metallic) and surface properties, with lengths ranging from a few nanometers (CNTs

and CNFs) up to practically any length. In this regard, each fiber length range corresponds to a specific scale of the material: nanofibers can only function to arrest flaws and cracks of size commensurate to their length [2–4]; similarly, microfibers function to restrain the propagation of flaws within the microscale, whereas longer fibers are intended to arrest visible cracks. Naturally, if a crack or flaw surpasses the geometric scale of any given type of fiber, it is expected that the next fiber scale will be mobilized to arrest it. In this stage, smaller fibers are not rendered inactive: each fiber range confines the anchorage of the next, longer scale fiber group. This is macroscopically evident through the enhanced fracture energy of the material; note that the poor tensile resistance of plain cementitious materials is due to the low strain energy storage capacity of the material lattice [5–7]. (The low-strength and limited-range cohesive forces, which bind the various products of cement hydration together in the

gel, diminish fast with increasing separation distance which occurs under tensile strain; this is manifested by the size effects and the independence of failure strain to transverse confining stress in tension-dominated failures of concrete [5].)

Although the synergistic effects of fibers with reinforcement, as well as synthetic and steel fiber cocktails, have been studied, only recently have pioneering efforts to address the flaws at the nanoscale been made through the addition of nanomaterials to the cementitious mix [2–8]. Note that macroscopic cracking is believed to initiate at the nanoscale in the gel structure. Of the additives that have been considered so far, nanoparticles (e.g., nanosilica) are intended to generate a more compact gel structure where flaws are of smaller size whereas the redundancy generated through compaction effectively causes significant redistribution of stress, thereby partially relieving the stress concentrations that lead to flaw propagation. On the other hand, carbon nanotubes (CNTs) and carbon nanofibers (CNFs), whose operating range is at the nanometer scale, are a form of passive reinforcement of the gel nanostructure, having an analogous role, at that scale, with macroscopic reinforcement in concrete. The mechanistic role of this type of reinforcement has been modeled analytically in [5] and it comprises the mere addition of effective reinforcement contribution to tensile resistance,  $\rho_{\text{CNT}} \cdot f_{\text{CNT}}$  in the otherwise plain cementitious material cross section ( $\rho_{\text{CNT}}$  and  $f_{\text{CNT}}$  are the effective area ratio and average stress intensity in the CNT network in the direction of tensile load). Experiments consistently illustrate that these materials effectively mitigate several of the fracture-related effects enhancing by measurable margin the tensile resistance, fracture energy, and most significantly the stiffness (Young's modulus) of the cementitious matrix [2, 5–8].

Studying the nanoreinforced material response to general states of stress requires a calibrated constitutive model that reflects the parametric sensitivities as well as the uncertainties necessarily embedded in the macroscopic properties of the composite. Recall that cementitious materials are amorphous, whereas past works that have published pictures of the nanostructure obtained through electron-scanning microscopy (ESM) reveal that CNTs often are inadequately distributed unless properly treated with surfactants [3, 4]. At best, the material has a random network of CNTs crossing an amorphous solid structure of hydrates. In this regard, the properties of the material have a statistical rather than a uniquely defined deterministic value. To study the effect of this randomness on the macroscopic mechanical properties and to quantify the strength and stiffness enhancement imparted by the addition of CNTs and CNFs, a discrete modeling framework was developed and further calibrated in this paper, mimicking the function of the gel structure. Thus, a statistically generated, continuous network of flaky dendrites comprising cement hydrates growing from partially hydrated cement grains is the background solid structure of the cementitious material in nanoscale. (Dendrites are the solid phase of the cement gel and interconnect to provide strength and stiffness against load.) Fibers such as CNTs are linear elements that span randomly between nodes of the dendrite mesh. Spaces that are not occupied

either by dendrite material or by the nanoreinforcement represent the pores, randomly located throughout the mesh. The idealized solid is subjected to displacement-controlled uniform boundary conditions, thereby simulating various stress states similar to lab tests. In this manner, the model is tested regarding its ability to reproduce the well-established behavioral traits of cementitious materials and to calibrate the experimental evidence regarding the role of reinforcement at the nanoscale. The statistical sensitivity of the model, the stability of the computational algorithm, and the resulting stress-strain curves that represent the material behavior in a macroscopic sense are studied in comparison with the experimental trends.

## 2. Dendrite Structure of the Solid Phase in Cementitious Gel

After hydration, the amount of water that was originally mixed with cement occurs in two different states: chemically bound in the hydrates (nonevaporable) or occupying the volume of pores; water in larger pores (capillary) may flow out easily, whereas water in the smaller pores is held by surface forces in the internal surface area of the hydrate and may be only lost upon heating. Therefore, the entire volume of the porous phase represents space that was originally occupied by water molecules which were subsequently chemically bound in the solid phase of the cement hydrates. The origin of strength and stiffness is due to the cement hydrates. As the chemical reaction proceeds, the solid phase grows radially from the reacting cement grain. During this process, growths from adjacent grains meet and merge in space, developing a solid network of amorphous mass; in the context of the present study, the axis of a branch is modeled by a linear element although it is implicit that it is endowed by hydrate volume that provides it with solid mass; the organization and scale dimension of the hydrates depend very much on the water/binder ratio,  $w_o$ , used during the mixing. The branch-like element, which resembles the structure of a tree, is referred to in the present study as a “dendrite.” Its form has been confirmed by electron-scanning microscopy (ESM) pictures of the microstructure, which show that the branches of solid mass span over gaping voids exactly like a network of truss elements. In the model, the linear elements that represent the dendrites are randomly generated from an initial, random distribution of cement grains, mimicking the chaotic distribution in nature as it is evident in ESM pictures (Figure 1). Dendrites fail in a brittle manner in axial tension whereas they are susceptible to buckling under compression due to their aspect ratio. In such a context, fibers of a scale comparable to the dendrite branches, such as carbon nanotubes (CNTs), added as mass reinforcement and properly anchored in the solid mass, add to the total number of elements bridging voids, thereby contributing (when stretched in tension) to the active links of the space truss that forms the solid phase of the cement hydrate; this may occur for fibers acting parallel to axial tension, or transversely to compression in response to Poisson-type lateral expansion of the macroscopic material [5]. Similarly,

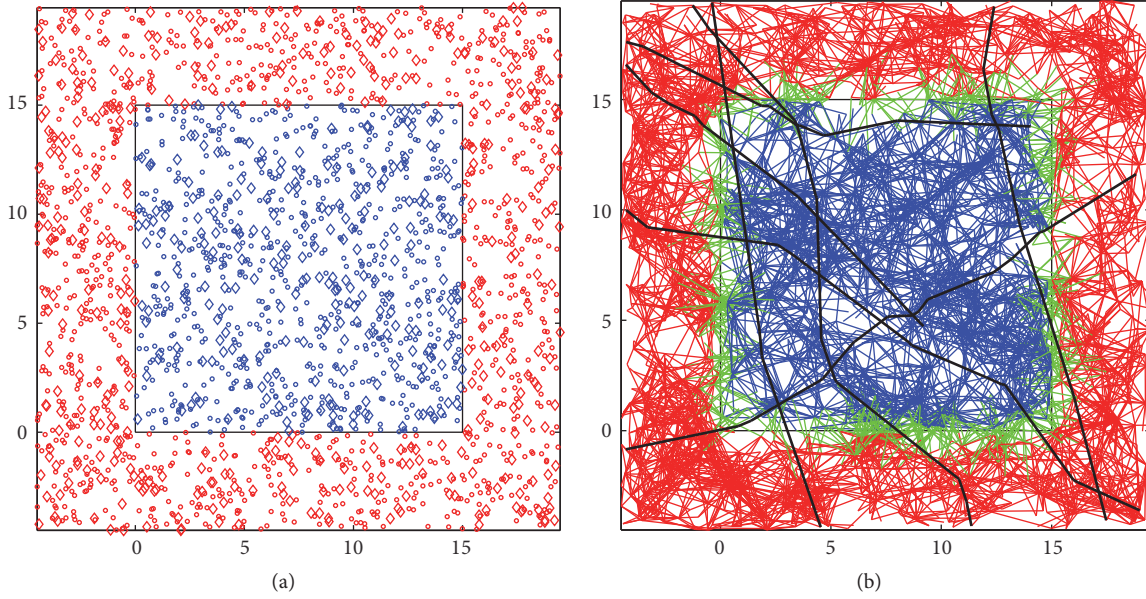


FIGURE 1: Discrete square space  $24 \times 24$  MHD. Central study region  $15 \times 15$  MHD is referred to as the “box.” Nodes and dendrites lie inside the box (blue) or outside the box (red) or across the boundary (green). (a) Source and target nodes for mesh generation. (b) Definition of dendrites and addition of CNTs (shown in black lines).

ESM photographs [4, 8] of the microstructure of CNT-reinforced materials illustrate this function of fibers: longer carbon nanotubes may even pass through several dendrites while at the same time interconnecting the solid flakes.

### 3. Mean Hydraulic Distance as a Measure of Scale in the Nanostructure

A characteristic measure of internal geometry in cementitious solids is the so-called mean hydraulic distance which is an idealized estimate of the mean separation distance between solid particles in the undisturbed (unstressed) condition. Another way to measure this distance is the diameter of the mean pore,  $\delta_o$ , since in reality a pore represents the distance between particles in the solid phase. Of course, such a measure may be misleading if seen as a deterministic geometric variable; it should rather be interpreted in light of the amorphous nature of the solid as a statistical mean distance. The mean pore size, considering that a capillary pore is idealized as a cylindrical slit with cross-sectional radius of  $r_o$  (i.e.,  $\delta_o/2$ ), may be estimated by the total pore volume divided by the pores' internal surface area, both being measurable and characteristic properties of the hydrate. Results from previous research [9] approximate  $r_o$  as the ratio of the evaporable water content of the cement hydrate,  $w_e$ , divided by the internal surface area of the pore structure,  $\Sigma_{\text{BET}}$ . Both variables are intrinsic properties of the hydrate which are expressed in terms of the water : cement ratio of the mix,  $w_o$ . The term  $w_e$  is quantified as the pore water lost on heating to  $110^\circ\text{C}$  and is approximated as  $w_e = 14.673w_oV_m \times 10^{-6}$  (in m), whereas  $\Sigma_{\text{BET}}$  is the internal surface area of the pores, estimated as  $\Sigma_{\text{BET}} = 3570V_m \text{ m}^2/\text{g}$  of anhydrous cement.  $V_m$  is the monolayer capacity of water of the hydrated

gel, assuming that the mean diameter of a water molecule is  $10.6 \text{ \AA}$ ;  $V_m$  is estimated from the chemically bound water  $w_n$  [9]. Thus, the hydraulic mean distance is estimated as

$$\begin{aligned} \delta_o &= 2 \frac{w_e}{\Sigma_{\text{BET}}} = 8.22 \times 10^{-9} w_o \quad (\text{in m}) \\ &= 8.22 w_o \quad (\text{in nm}). \end{aligned} \quad (1)$$

For example, given a water-cement ratio,  $w_o = 0.4$ , it follows that the mean pore diameter in the gel is  $\delta_o = 3.288 \text{ nm}$ , whereas for  $w_o = 0.6$  the characteristic distance is  $\delta_o = 4.932 \text{ nm}$ . Thus, based on the definition of the hydraulic mean distance as a measure of the equilibrium separation distance, a direct link between the density of packing in the cementitious matrix and mechanical strength is possible; a higher water-to-cement ratio leads to a less densely packed structure due to the increase in porosity. Clearly, the smallest unit that might be considered as a representative material sample must be in the order of few tens of nanometers so as to maintain the characteristics of the solid including its porosity while also allowing for statistical variability in the geometric arrangement of the solid phase.

### 4. Discrete Model of Cement Hydrate

**4.1. Mesh Production and Generation of Dendrites.** The problem is idealized in a two-dimensional plane; that is, plane-stress conditions are considered in the model. In principle, the model may be extended to the three dimensions, albeit at significant computational expense. The essential attributes of the solid structure of cementitious gel are emulated by abstracting the solid phase so as to represent it as linear segments spanning along the axes of the dendrites which

emanate from a mesh of nodes which correspond to the initial position of the cement grains.

Therefore, the first step in generating the computational mesh is the random placement of cement grains in a rectangular solid section that extends in  $x$  and  $y$  several times the mean hydraulic distance (MHD = mean pore diameter =  $\delta_o$  in (1)). Each cement grain is a source node, with uniform probability of density  $\text{MHD}^{-2}$  (Figure 1(a)). The number of cement grains that fit in the  $x$ - $y$  space is a function of the cement content per unit volume of the mix. The generic step of the mesh-formation algorithm is to “grow” the solid structure from each partially hydrated cement grain. Next, an independent random set of uniformly distributed destination points is generated and superimposed in the test domain (Figure 1(a)). These nodes are referred to as target nodes, and they occur 3 times as frequently as the source nodes. The two sets of nodes are connected by branches that are generated randomly. However, not all possible connections are enforced. Branches represent hydration products in the form of dendrites growing outwards from the cement grains. Each pair of a source and a target node represents a potential branch, which is actually added to the model only if  $\exp(-L/\text{MHD}) > \text{rand}()$ , where  $L$  is the length of the potential branch in question and  $\text{rand}()$  is a computer-generated pseudorandom number (uniformly distributed in  $[0, 1]$ ). Thus, branch length is an exponentially distributed random variable with expectation MHD. However, a maximum allowed branch length is also enforced and arbitrarily set equal to 3 MHD; higher upper limits to the lengths of the dendrites have also been considered and their effect on the resulting constitutive behavior of the material has been explored. The dendrite branches are assumed to have circular cross section, the area of which is the same at all branch tips. The tip cross section is set arbitrarily equal to  $10^{-8}$  in consistent units and increases linearly with distance from the tip, up to  $1.2 \times 10^{-8}$  at 1 MHD from the tip and to a maximum of  $1.6 \times 10^{-8}$  at 3 MHD from the tip, which is the maximum allowed branch length.

The mesh considered for response analysis under various boundary conditions extends over a square zone with a size that ranges between  $6 \times 6$  and  $30 \times 30$ , in units of MHD, with  $15 \times 15$  being considered a regular specimen size (this is the most common size of samples without fibers that were used to study the behavior of the cementitious material to a variety of stress states). The square zone is referred to hereon as a “box.” Node and branch generation, however, occurs over a much wider area and the exterior boundary of the “box” is centered in the area of source and target node generation, as depicted in Figure 1(b). Dendrite branches that cross the boundary of the “box” are trimmed at the point of intersection with the perimeter (branches in green in Figures 1(b) and 2(b)). New nodes on the boundary of the box generated in the process (green in Figure 2(a)) are related to master nodes. This is a computational device that enables enforcement of constant principal strains (equivalent to affine kinematics) on the whole boundary of the box, while making sure that the computational area is free of boundary artifacts and as representative of “average conditions” as possible.

The dendrite material is considered linear elastic in tension and compression. Basic properties refer to the tensile stress and strain values at rupture,  $\sigma_{bf}$  and  $\varepsilon_{bf}$ . Compressive strength at crushing is taken ten times as high; thus, compression crushing of the branch material is unlikely. Instead, the most prevalent type of failure in compression is linear elastic Euler buckling. This is followed by a brittle response cutoff. The modulus  $E_{bf}$  of the dendrite material is obtained from the ratio  $\sigma_{bf}/\varepsilon_{bf}$ . This value is used in the subsequent study in order to normalize the value of the secant modulus of the “box” to the applied strain. (Input values used in the present study were  $E_{bf} = 10^{+9}$ ,  $\varepsilon_{bf} = 10^{-5}$ , and  $\sigma_{bf} = 10^{+4}$ , in consistent units.) Finally, the branches are treated as if they were cylindrical of “average” cross section, both in force/stiffness state determination and in estimating Euler buckling loads (i.e., the paraboloid taper in the lengthwise direction of the typical dendrite is replaced for these calculations with an equivalent uniform cross section).

A similar generation procedure was used in order to define CNTs in the mesh, so as to enable a random definition of their layout in the sample specimen. Considering the usual CNTs that are currently available on the market, their length is in general about two orders of magnitude longer than dendrites and one order of magnitude longer than the sample region. So, CNTs are defined in the greater generation area and then only those that cross the boundary of the “box” are considered in studying the mechanics of the state of stress of the composite (Figures 1(b) and 2(b)). In placing and orienting the CNTs and in light of the ESM photographic material that shows them to be generally curved in their final position [4, 5], they are modeled as multilinear segments in the material space. This is consistent with the fact that CNTs may be curved in the fresh mix state and “frozen” in that position after hardening. To achieve this from a computational perspective, in the present model, the fibers were assumed to interact with the network of hydrates by being attached to target nodes. Therefore, a typical CNT may comprise a multisegment element attached to several nodes. This model recognizes that the macroscopic effects imparted by the CNTs will be primarily controlled by the volumetric ratio of nanofibers in the mix. The discrete number of fibers within the extended specimen, before trimming, is an integer approximation of their cross-sectional area times their expected length divided by the volume of the extended specimen. The extreme variability of fiber density is expected. This is more so for higher fiber cross-sectional areas, since very few fibers are generated (in some cases as few as five) and even fewer lie within the specimens eventually analyzed. The actual strength and stiffness parameters of the fibers are not particularly relevant in compression as fibers are considered inactive in that direction. Fibers function as one-sided springs that are only engaged in tension. Their modulus of elasticity is at least one order of magnitude higher than that of the hydrate, taken here as  $E_{\text{fib}} = 1e + 10$  in consistent units.

*4.2. Performance of the Idealized “Box” Area under Load.* In the present section, the mechanical behavior of the “box” model is studied under various controlled boundary

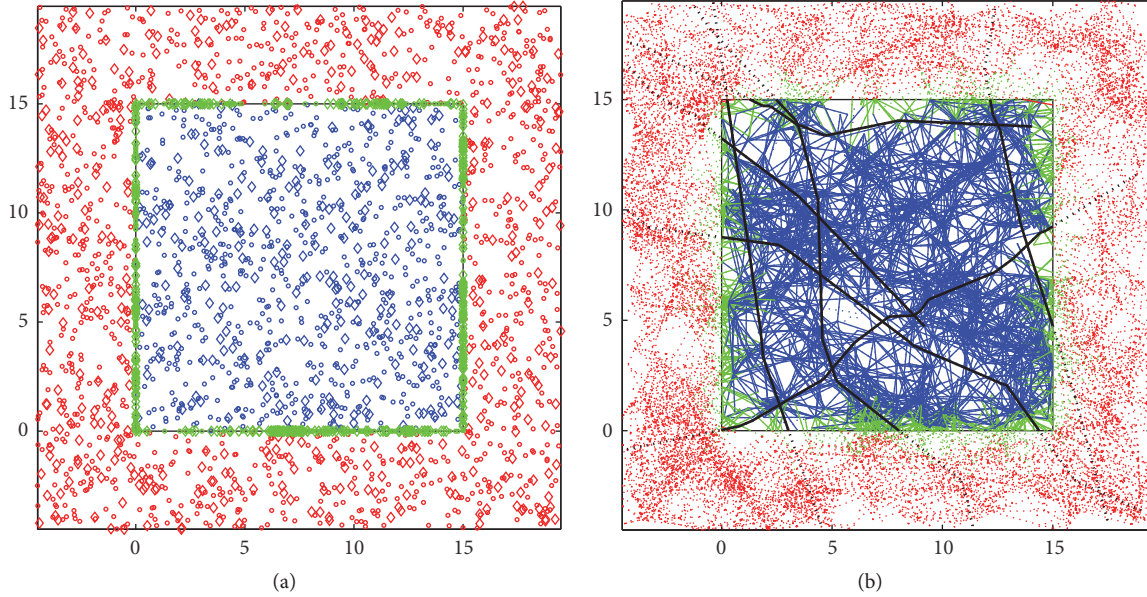


FIGURE 2: Trimming of the  $15 \times 15$  MHD “box.” (a) New boundary nodes (green) are created where branches cross the perimeter of the box. (b) Trimming of elements to the “box.” Dashed lines represent trimmed dendrites (red) and CNTs (black). Space not occupied by the solid structure represents the voids (pores) of the material.

conditions, with the objective of identifying and interpreting the contribution of the CNTs in the apparent properties of the reinforced cementitious matrix. Analysis in 2D is conducted using constant strain increments,  $\Delta\varepsilon_2 = \varepsilon_{bf}/100$  or  $\Delta\varepsilon_2 = \varepsilon_{bf}/200$ , along the direction of displacement control (i.e., along geometric axis 2 in Figure 1), with tolerance of  $10^{-6}$  in both displacement values and loads. A direct stiffness assembly process is used to define the current form of the equation of static equilibrium. Solution is performed using standard nonlinear system solvers (Newton type). With refinement of increments, convergence is improved; the last converged configuration is used as the starting point in each new increment. Note that divergence of the algorithm has occurred in certain cases, due to local singularities that arise after failure of some dendrites.

Loading on the model may be conducted under either load or displacement control using the master nodes which control the kinematics of the boundary nodes as described in Section 4.1. An important reference point that may be used to assess the validity of the model is the relevance of calculated response of the reinforced composite under uniaxial compression and tension to the observed experimental trends [3, 5]. Analysis of the uniaxial stress state is conducted under displacement control along axis 2 that corresponds to the axis of load application. In the transverse direction, the “box” is left to expand or contract freely with the condition that the corresponding stress resultants are zero. Similarly, analysis of the uniaxial strain state (tension or compression along axis 2) is conducted by requiring that zero translation occurs in the transverse direction (boundary conditions along axis 1). Finally, pure shear strains are enforced by requiring the translation in the transverse direction (axis 1) to be the opposite of the controlled displacement (along axis

2). CNT-reinforced samples are only tested under uniaxial stress or strain conditions; further experiments are underway to calibrate the CNT-model performance under arbitrary states of stress. Figures 4(a) and 4(b) plot the corresponding stress-strain relationships that characterize the response of the composite (as does Figure 3 for plain paste). Here, each principal strain is obtained by dividing the displacement with the corresponding “box” dimension, and each stress is defined as the ratio of the resultant traction force divided by the area presented to load (=breadth of the “box” times its thickness of one MHD). Plots include smeared axial-stress-strain relationship in the direction of loading. In all cases, the stress terms are nondimensionalized with respect to the material properties of the branches, that is, with respect to the ideal properties of the cementitious solid. Furthermore, for the sake of comparison of results from specimens of different material densities, stresses are further normalized by division with the volume ratio of the gel in the “box.”

Each time the program is run with the same input values, a different random truss is created, owing to the random generation process. Hence, two otherwise identical execution instances of the algorithm will not lead to identical results. Variability occurs not only in the net magnitude of the values but also in the state of convergence of the algorithm at various levels of applied displacement. This is reflected in the occasional digressions from the calculated stress-strain curves, most of which are “local” and swiftly return to the backbone curve. Nevertheless, all calculated stress-strain envelopes (Figures 3, 4(a), and 4(b)) have very clear backbones that follow qualitatively the expected shape of compressive and tensile stress-strain response of semibrittle materials as is known from experimental experience [1, 2, 4, 5, 9, 10]. Even for loading conditions that do not give

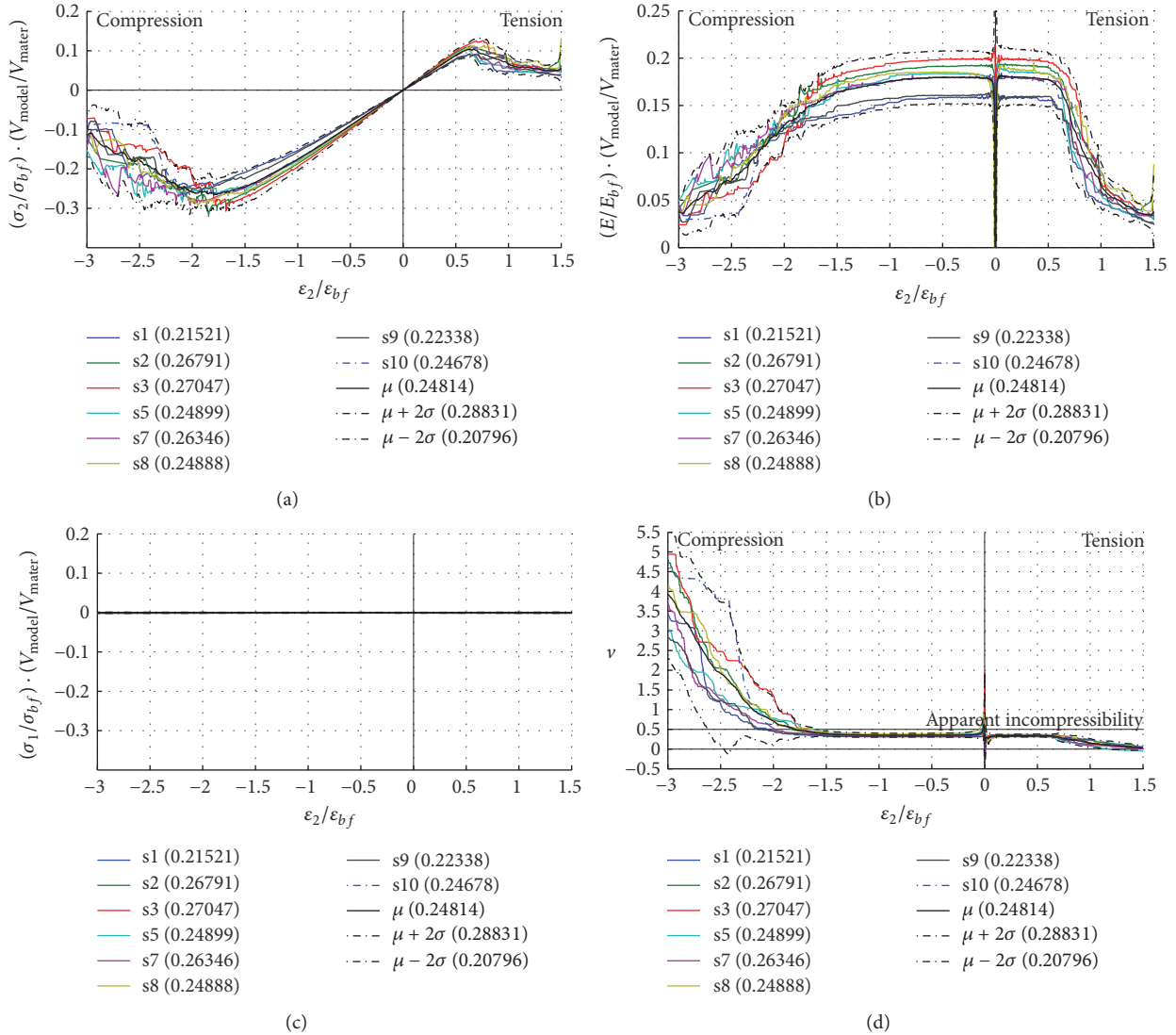


FIGURE 3: Individual response curves of unreinforced discrete specimens ( $15 \times 15$  MHD) to uniaxial plane-stress loading, along with sample mean response curves (solid black line) and  $2\sigma$ -envelopes (dashed dotted black line). Stresses and moduli of elasticity are made comparable across samples by division with the observed volume density  $V_{\text{mater}}/V_{\text{model}}$  of each specimen (given in parenthesis in the legend). (a) Stress in direction of loading. (b) Secant modulus of elasticity. (c) Stress across loading (zero throughout). (d) Secant Poisson ratio (apparent incompressibility observed at limit point in compression).

rise to macroscopic stretching, internal equilibrium of the random truss dictates that many elements must be in tension, and usually these fail first (leading to redistribution of tension to decreasingly capable elements). The characteristic of the softening postpeak branch occurs when tensile fracture of dendrites orients in the direction of prevalent tension, followed by an avalanche of buckled dendrites oriented in the direction of prevalent compression.

**4.3. Discussion of Results.** The parametric performance of the discrete material model is illustrated in the graphs of Figures 3, 4(a), and 4(b). Each figure comprises four graphs that present in 2D the relationship between smeared stresses and the axial and lateral strain for the case study considered.

The  $x$ -axis represents the applied controlling strain (i.e., the displacement normalized with the “box” dimensions so as to have the physical significance of infinitesimal strain),  $\epsilon_2$ ; this variable is normalized further with the rupture strain of the basic dendrite material,  $\epsilon_{bf}$ . In the four graphs shown, the  $y$ -axis has the following significance: in case (a), it is the average value of stress,  $\sigma_2$ , which is collinear to the applied strain  $\epsilon_2$ ; again,  $\sigma_2$  is plotted after being normalized by  $\sigma_{bf}$  and by the volume fraction of gel solid in the “box.” In case (c), the plotted variable is the lateral stress  $\sigma_1$ , after having been normalized in the same manner. In case (b), the  $y$ -axis represents the secant modulus of elasticity normalized by the dendrite material modulus,  $E_{bf}$ , and by the volume fraction of gel solid in the “box.” In case (d), the plotted variable is the secant value of Poisson’s ratio,  $\nu$ .

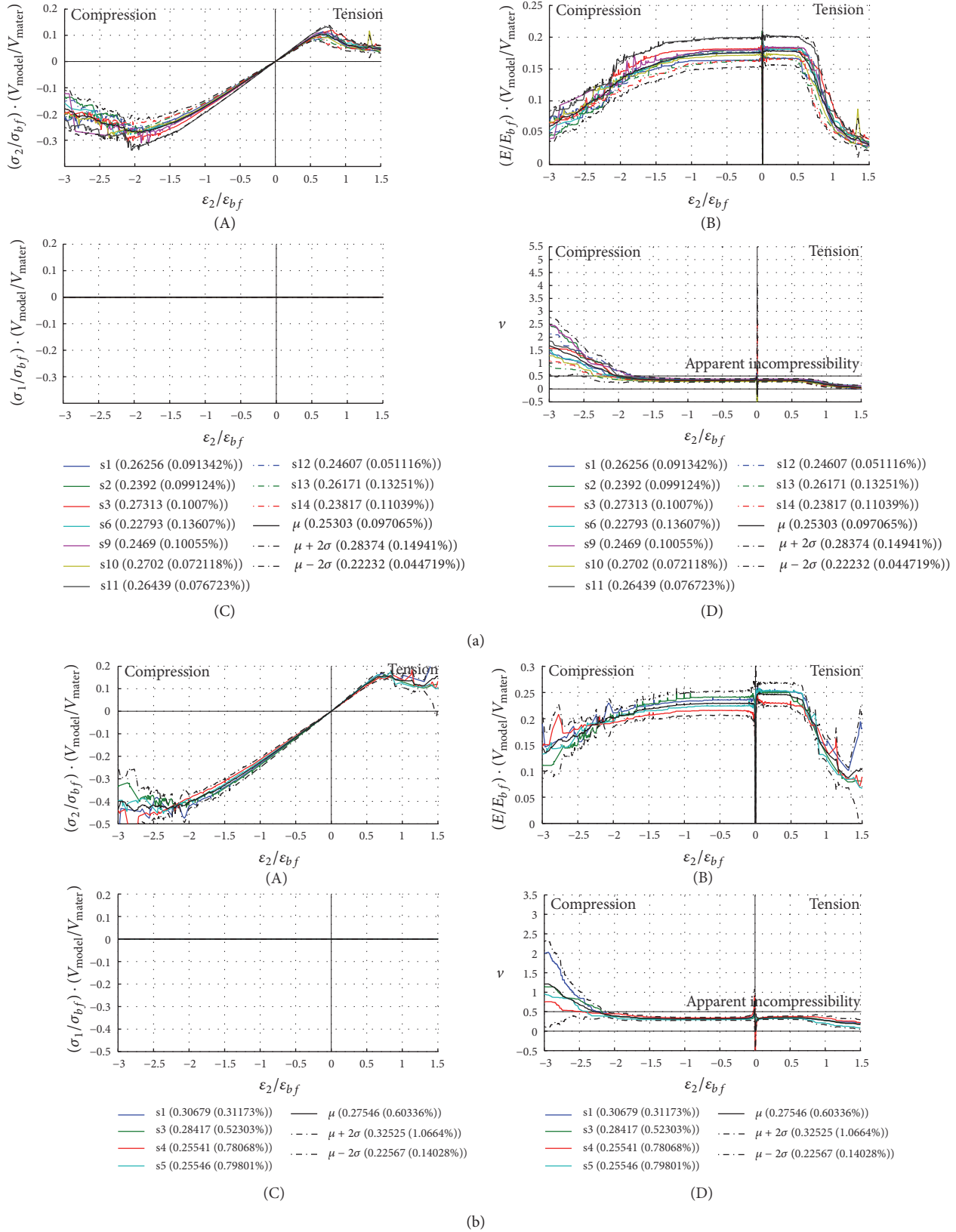


FIGURE 4: Individual response curves, along with sample mean response curves (in solid black) and  $2\sigma$ -envelopes (in dashed dotted black), for uniaxial plane-stress loading of discrete specimens ( $15 \times 15$  MHD) reinforced with CNTs. Stresses and moduli of elasticity are divided by the observed volume density  $V_{mater}/V_{model}$  of each specimen (given in parenthesis in the legend, along with the actual CNT content per solid volume of specimen). (A) Stress in direction of loading. (B) Secant modulus of elasticity. (C) Stress across loading (zero throughout). (D) Secant Poisson ratio (apparent incompressibility observed at limit point in compression). The two groups differ with respect to the targeted CNT content, which is (a) 0.1% per volume of paste and (b) 1% per volume of paste.

Each example material and stress state is studied with several analytical specimens, as discussed earlier. Therefore, the bundle of curves depicted in any given type of plot has been obtained by randomly generating a study “box” each time and repeating the solution using identical input values for each run. So, samples 1, 2, 3, and so forth represent cases that are in principle identical but are practically different, since they have been randomly generated. Note that the observed variability between curves is expected and represents the analytical analogue of the statistical variability witnessed in real lab work, whenever a group of identical specimens is physically tested. Each specimen is codified in the legend of the figure by a composite ID, which includes the specimen number, its volume density, and the corresponding CNT volume ratio ( $V_{\text{CNT}}/V_{\text{mater}}$ ), if any; here  $V_{\text{CNT}}$  and  $V_{\text{mater}}$  are the volume of CNTs and the volume of hydrates, respectively, contained in a “box.” Volume density is defined as the ratio of the volume of solid material in the “box,”  $V_{\text{mater}}$ , to the volume of the “box” itself (i.e.,  $V_{\text{model}} = A_{\text{model}} \times \text{MHD}$ ). For example, a code of s1 (0.26256 (0.091342%)) refers to specimen number 1 from the batch in question, containing dendrites that account for 26.3% of its volume (which is  $15 \times 15 \times 1 \text{ MHD}^3$  in all three figures). This number (0.26256) divides the stress and stiffness values measured from the specimen to make them comparable with those of other specimens (of different density). The measured volume ratio of CNTs to dendrites is 0.091% (whereas the targeted value for the batch is 0.1%). Note that if a specimen number is missing in the sequence, this implies that global divergence occurred in the simulation of its response, so its results are not available.

An important open issue of the investigation is to determine whether the computational results are susceptible to mesh sensitivity. Towards this objective, several groups of specimens of plain paste (nominally differing only in box dimensions) were examined in uniaxial compression, uniaxial tension, and pure shear. Results are summarized in Table 1. Subscripts  $ct$  and  $cc$  refer to tensile and compressive terms of the cementitious composites, respectively, whereas  $cv$  refers to shearing of the same (applied kinematically under shear-strain control). In the first column,  $N$  represents the linear dimensions of numerical specimens ranging from 6 to 30 MHD. Mean values of limit-point responses for each group of samples studied are listed (with the coefficient of variation given in parentheses). Clearly, scale effects are significant and may be attributed both to the nature of the model (brittle dendrites making up the solid structure) and to numerical considerations (kinematic boundary constraints). In all simulations, the (secant) Poisson ratio is strikingly consistent, regardless of sample parameters or loading considered. Its initial values are estimated at  $\nu = 1/3$  and remain approximately constant in tension tests up to the limit point. Its effective value rises to  $\nu = 0.5$  near the limit points in compression regardless of the boundary condition, consistent with experimental results from previous studies on confined plain concrete [9–11]. It is therefore concluded that using  $\nu = 0.5$  as the criterion of compressive failure complies with the experimental evidence.

It was observed that, in cases dominated by *tensile strain*, behavior is almost linear up to the limit point. For  $15 \times 15 \text{ MHD}$

specimens, the coordinates of the limit point are as follows: (a) in uniaxial tension,  $\bar{\epsilon}_{ct} = 0.67 (\pm 11\%)$  with  $\bar{\sigma}_{ct} = 0.11 (\pm 10\%)$ ; (b) in kinematic shearing,  $\bar{\epsilon}_{cv} = 0.68 (\pm 10\%)$  with  $\bar{\sigma}_{cv} = 0.077 (\pm 10\%)$ ; (c) in uniaxial stretching (where it is found that  $\sigma_1 \approx \sigma_2/3$  up to the limit point) at the onset of the tensile stress-strain postpeak branch,  $\bar{\epsilon}_{ct} = 0.62 (\pm 8\%)$  with  $\bar{\sigma}_{ct} = 0.11 (\pm 5\%)$ ; and (d) in biaxial tension with  $\sigma_1 \approx \sigma_2/2$ ,  $\bar{\epsilon}_{ct} = 0.63 (\pm 9\%)$  with  $\bar{\sigma}_{ct} = 0.12 (\pm 12\%)$ . The results indicate failure at an ultimate tensile *stress* in loading cases with  $\sigma_1\sigma_2 \geq 0$  and failure at an ultimate tensile *strain* in loading cases with  $\sigma_1\sigma_2 \leq 0$ . Transition between the two failure criteria occurs at the point of uniaxial tension with  $\sigma_1\sigma_2 = 0$ , where both  $\sigma_2 = f_{ctu}$  and  $\epsilon_2 = \epsilon_{ctu}$  apply.

Consistent with the apparent uniaxial stress-strain response recorded during tests, analyses of computational samples where compressive stresses dominate failure are marked by pronounced nonlinearity before the limit point. For  $15 \times 15 \text{ MHD}$  specimens and failure defined by  $\nu \approx 0.5$ , the following results are obtained for the limit point: (a) under uniaxial compression,  $\bar{\epsilon}_{cc} = -1.90 (\pm 6\%)$  with  $\bar{\sigma}_{cc} = -0.30 (\pm 3\%)$ ; (b) under uniaxial contraction,  $\bar{\epsilon}_{cc} = -4.83 (\pm 20\%)$  with  $\bar{\sigma}_{cc} = -0.64 (\pm 17\%)$ , where  $\sigma_1 = \sigma_2/2$  at failure; and (c) under biaxial compression with  $\sigma_1 = \sigma_2/2$ ,  $\bar{\epsilon}_{cc} = -5.05 (\pm 10\%)$  with  $\bar{\sigma}_{cc} = -0.69 (\pm 21\%)$ . Note that the last two cases lead to essentially the same limit point (the differences in both stress and strain being statistically insignificant) but trace different paths in stress and strain. Note that, consistent with the experimentally documented effects of confinement, this limit point is roughly 2.3 times higher in stress and 2.8 times higher in strain than the one in uniaxial compression. Also, the ratio of compressive to tensile strength ( $\sigma_{cc}/\sigma_{ct}$ ) is about 3, owing to the absence of aggregates in the model (the ratio is appropriate for paste only as modeled here).

Analysis under *kinematic shearing* (i.e., external load is applied under shear-strain control in a state of pure shear strain) yields a limit state of stress where the compressive stress is higher than the tensile one, by 5% in one direction of loading and by 13% in the reverse. If this difference were due to the anisotropy of the random specimens, it should have roughly zero mean value over the sample. Since this is not the case, some disintegration is clearly present at the limit point. Using all samples, the estimated mean values are  $\bar{\epsilon}_{cv} = 0.68 (\pm 10\%)$  with  $\bar{\sigma}_{cv} = -0.077 (\pm 8\%)$ , where  $\bar{\sigma}_{ccv} = -0.080 (\pm 8\%)$  and  $\bar{\sigma}_{ctv} = +0.074 (\pm 8\%)$ . The physical significance of this result is that the limit value of shear strength is 70% of the tensile strength  $\bar{\sigma}_{ct} = 0.11 (\pm 10\%)$ , which is within the bounds of the expected magnitude.

To assess the contribution of CNT reinforcement on the mechanical properties of the material, different CNT contents were considered in the study; nominal CNT volumetric ratios, calculated with reference to the final material volume, were targeted to values of 1%, 0.5%, and 0.1%. These are usual contents that have been tried in tests [5–7] (parameter  $A_{\text{fib}}$  represents the cross-sectional area of the CNTs). Due to the manner of their generation (see Section 3), the actual yield of CNTs in the mix differed from the targeted ratios (Table 2).

Comparison of results at these levels of reinforcement with results from plain paste samples indicates the following effects (Figures 4(a) and 4(b)). (a) When using unrealistically

TABLE 1: Summary of mesh sensitivity study: normalized stresses and strains at limit points.

Mesh size in MHD multiples $N$	$\bar{\varepsilon}_{ct} = \frac{\varepsilon_{ct}}{\varepsilon_{bf}}$	$\bar{\sigma}_{ct} = \frac{\sigma_{ct}}{\sigma_{bf}} \frac{V_{model}}{V_{mater}}$	$\bar{\varepsilon}_{cc} = \frac{\varepsilon_{cc}}{\varepsilon_{bf}}$	$\bar{\sigma}_{cc} = \frac{\sigma_{cc}}{\sigma_{bf}} \frac{V_{model}}{V_{mater}}$	$\bar{\varepsilon}_{cv} = \frac{\varepsilon_{cv}}{\varepsilon_{bf}}$	$\bar{\sigma}_{cv} = \frac{\sigma_{cv}}{\sigma_{bf}} \frac{V_{model}}{V_{mater}}$
6	0.80 ( $\pm 12\%$ )	0.15 ( $\pm 13\%$ )	-2.30 ( $\pm 8\%$ )	-0.38 ( $\pm 15\%$ )	-2.12 ( $\pm 13\%$ )	-0.35 ( $\pm 16\%$ )
9	0.75 ( $\pm 8\%$ )	0.13 ( $\pm 11\%$ )	-2.09 ( $\pm 6\%$ )	-0.34 ( $\pm 10\%$ )	-1.99 ( $\pm 10\%$ )	-0.31 ( $\pm 10\%$ )
15	0.68 ( $\pm 11\%$ )	0.11 ( $\pm 10\%$ )	-1.92 ( $\pm 5\%$ )	-0.30 ( $\pm 3\%$ )	-1.90 ( $\pm 6\%$ )	-0.30 ( $\pm 3\%$ )
21	0.58 ( $\pm 6\%$ )	0.091 ( $\pm 5\%$ )	-1.89 ( $\pm 3\%$ )	-0.25 ( $\pm 8\%$ )	-1.84 ( $\pm 5\%$ )	-0.25 ( $\pm 8\%$ )
30	0.57 ( $\pm 6\%$ )	0.088 ( $\pm 5\%$ )	-1.74 ( $\pm 4\%$ )	-0.23 ( $\pm 3\%$ )	-1.72 ( $\pm 4\%$ )	-0.23 ( $\pm 4\%$ )

TABLE 2: Calculated effect of CNT reinforcement in the cementitious matrix.

Target CNT per vol.	Actual CNT per vol.	$\sigma_{ct}$ increase	$\sigma_{cc}$ increase	$E$ increase
1%	0.3%–0.8%	25%	40%	30%
0.5%	0.28%–0.41%	10%	10%	10%
0.1%	0.03–0.1%	—	—	1%

high CNT content (a theoretical limit), the peak load-bearing capacity is effectively doubled, presenting the behavior of passively confined concrete (Figure 4(b)); note that past work has illustrated the role of CNT or CNF reinforcement as effective internal confinement [5, 11]. This is quantified not only by the increased compressive strength of the composite, but also by the reduced dilation rate (apparent values of the secant Poisson ratio,  $\nu$ ). It is worth noting that the sample variability in this respect is very low (less than 10%) confirming that the mechanistic confining contribution of the fibers is a consistent, repeatable finding. For lower ratios, the effects of the CNT addition on stiffness and strength of the composite are proportionately attenuated becoming insignificant for very low amounts of CNT content, although the modulus of elasticity in tension is higher than that in compression, underscoring the CNT contribution even if the CNT contents are low (Figure 4(a)). In all cases, however, the postlimit behavior was significantly improved, marked again by smaller values of apparent secant  $\nu$  as compared to the unreinforced counterpart. This behavior is the same as that of FRC under unconfined compression [1] and is very similar to that of confined conventional concrete [9, 11]; a mechanistic-based interpretation of the effective confinement provided by CNT fibers in the gel has been derived and corroborated with experimental results in [5]. Generally, better overall convergence and stability of deformation were observed. The CNT-reinforced samples were able to maintain 35% to 40% of their peak load-bearing capacity even at very high levels of sample deformation, again illustrating the confining effect imparted by the CNT reinforcement in the cementitious matrix. At that stage, the CNTs function as continuity reinforcement where load transfer may follow a roundabout path through the fibers if a cluster of dendrites has encountered either rupture or buckling.

## 5. Conclusions

This paper presents results from computational simulations of the mechanical behavior of cementitious matrices

reinforced by the addition of carbon nanotubes. These additives operate at the nanoscale of the matter and are intended to control the creation of flaws (cracks) within the gel structure, well before these may propagate to higher geometric scales (micro- and mesoscales), where larger, visible steel or synthetic fibers may operate. Simulations are carried out using a novel discrete representation of the nanostructure of the gel, which has been developed in the present paper from first principles. In deriving the model, the intent was to reproduce and highlight the interactions occurring between cementitious material particles and nanoreinforcement such as CNTs and CNFs. In this regard, a novel approach is used to model the hydrates as randomly generated dendrites emanating from partially hydrated cement grains and intertwining to create load and resistance paths randomly oriented in the solid. Dendrite geometric properties and cement grain positioning are randomly generated, so that responses obtained are quantified by the mean values and dispersion as occurs in laboratory testing of several identical specimens. The model provides a testbed for the study of the material behavior under stress and strain. For this purpose, the material model is subjected to constraints that mimic various controlled laboratory experiments that are conducted for material characterization (uniaxial tension/compression, uniaxial stretching/contraction, and pure kinematic shear). Calibrated to fit the macroscopic physical characteristics of the matrix (density and mean pore size), the model reproduces successfully several known macroscopic behavioral traits of cementitious materials, including the characteristics of the yield and failure surfaces under states of plane stress/strain. The discrete model is combined with a random network of CNTs of known geometric and mechanical properties to computationally reproduce the parametric sensitivities and measured properties of nanoreinforced cement-based composites successfully. It is shown that CNTs effectively confine the material passively, leading to increased strength and stiffness in compression with a much slower rate of degradation and lateral dilation (phenomenological Poisson's ratio), consistently with experimental evidence of

a significant confining effect occurring in the microstructure of the matrix and effectively increasing the apparent material stiffness [1, 4, 5, 11].

## Conflicts of Interest

The authors declare that there are no conflicts of interest regarding the publication of this article.

## Acknowledgments

This research was cofinanced by the EU (European Social Fund, ESF) and Greek national funds through the Operational Program “Education and Lifelong Learning” of the National Strategic Reference Framework (NSRF), Research Funding Program: “Thales-Democritus University of Thrace-Center for Multifunctional Nanocomposite Construction Materials” (MIS 379496).

## References

- [1] S. J. Pantazopoulou and M. Zanganeh, “Triaxial tests of fiber-reinforced concrete,” *Journal of Materials in Civil Engineering*, vol. 13, no. 5, pp. 340–348, 2001.
- [2] G. Y. Li, P. M. Wang, and X. Zhao, “Mechanical behavior and microstructure of cement composites incorporating surface-treated MWCNTs,” *Carbon*, vol. 43, pp. 1239–1245, 2005.
- [3] M. S. Konsta-Gdoutos, “Nanomaterials in self-consolidating concrete: a state-of-the-art review,” *Journal of Sustainable Cement-Based Materials*, vol. 3, no. 3-4, pp. 167–180, 2014.
- [4] Z. S. Metaxa, M. S. Konsta-Gdoutos, and S. P. Shah, “Carbon nanotubes reinforced concrete,” *ACI Special Publication*, vol. 276, no. 2, pp. 11–19, 2009.
- [5] N. D. Archontas and S. J. Pantazopoulou, “Microstructural behavior and mechanics of nano-modified cementitious materials,” *Advances in concrete construction*, vol. 3, no. 1, pp. 15–37, 2015.
- [6] P. A. Danoglidis, M. S. Konsta-Gdoutos, E. E. Gdoutos, and S. P. Shah, “Strength, energy absorption capability and self-sensing properties of multifunctional carbon nanotube reinforced mortars,” *Construction and Building Materials*, vol. 120, pp. 265–274, 2016.
- [7] E. E. Gdoutos, M. S. Konsta-Gdoutos, P. A. Danoglidis, and S. P. Shah, “Advanced cement based nanocomposites reinforced with MWCNTs and CNFs,” *Frontiers of Structural and Civil Engineering*, vol. 10, no. 2, pp. 142–149, 2016.
- [8] L. I. Nasibulina, I. V. Anoshkin, S. D. Shandakov et al., “Direct synthesis of carbon nanofibers on cement particles,” *Transportation Research Record*, vol. 2142, pp. 96–101, 2010.
- [9] S. J. Pantazopoulou and R. H. Mills, “Microstructural aspects of the mechanical response of plain concrete,” *ACI Materials Journal*, vol. 92, no. 6, pp. 605–616, 1995.
- [10] I. Imran and S. J. Pantazopoulou, “Experimental study of plain concrete under triaxial stress,” *ACI Materials Journal*, vol. 93, no. 6, pp. 589–601, 1996.
- [11] S. P. Tastani, M. S. Konsta-Gdoutos, S. J. Pantazopoulou, and V. Balopoulos, “The effect of carbon nanotubes and polypropylene fibers on bond of reinforcing bars in strain resilient cementitious composites,” *Frontiers of Structural and Civil Engineering*, vol. 10, no. 2, pp. 214–223, 2016.

## Research Article

# Flexural Behavior of High-Volume Steel Fiber Cementitious Composite Externally Reinforced with Basalt FRP Sheet

**Seungwon Kim and Cheolwoo Park**

*Department of Civil Engineering, Kangwon National University, 346 Choongang-ro, Samcheok 25913, Republic of Korea*

Correspondence should be addressed to Cheolwoo Park; tigerpark@kangwon.ac.kr

Received 23 September 2016; Accepted 20 November 2016

Academic Editor: Peng Zhang

Copyright © 2016 S. Kim and C. Park. This is an open access article distributed under the Creative Commons Attribution License, which permits unrestricted use, distribution, and reproduction in any medium, provided the original work is properly cited.

High-performance fiber-reinforced cementitious composites (HPFRCCs) are characterized by unique tensile strain hardening and multiple microcracking behaviors. The HPFRCC, which demonstrates remarkable properties such as strength, ductility, toughness, durability, stiffness, and thermal resistance, is a class of fiber cement composite with fine aggregates. It can withstand tensile stresses by forming distributed microcracks owing to the embedded fibers in the concrete, which improve the energy absorption capacity and apparent ductility. This high energy absorbing capacity can be enhanced further by an external stiff fiber-reinforced polymer (FRP). Basalt fabric is externally bonded as a sheet on concrete materials to enhance the durability and resistance to fire and other environmental attacks. This study investigates the flexural performance of an HPFRCC that is externally reinforced with multiple layers of basalt FRP. The HPFRCC considered in the study contains steel fibers at a volume fraction of 8%.

## 1. Introduction

The high-performance fiber-reinforced cementitious composite (HPFRCC) is a class of fiber cement composite with fine aggregates that exhibits remarkable properties such as strength, ductility, toughness, durability, stiffness, and thermal resistance. It can withstand tensile stresses by forming distributed microcracks owing to the embedded fibers in the concrete, which improve the energy absorption capacity and apparent ductility [1]. Fiber-reinforced polymer (FRP) composites are attractive and advantageous lightweight materials used for the rehabilitation and retrofitting of reinforced concrete and prestressed concrete structures. In the past few decades, the externally bonded FRP has evolved into an advanced and well-established technology. Lightweight FRP strips are easy to handle and can be installed without heavy equipment. This study investigates the flexural performance of an HPFRCC that is externally reinforced with multiple layers of basalt FRP with different strip orientations.

Currently, the service life extension of structures is an important concern that must be addressed. The choice of the strengthening systems directly depends on the performance, which is based on requirements such as increasing flexural,

shear, torsion strength, or ductility of the structures. In addition to ongoing construction works of civil engineering infrastructure, existing structures should be considered as well. The complete replacement of structures is not an option owing to the financial burden and effort involved during construction in the past.

Terrorist attacks are one of the most pressing issues confronting the world today [2], and civil engineering structures are the most vulnerable to the destructive effects of such attack. For this reason, there has been an increased interest in developing materials with high toughness that resist impacts and blast loading. Recently, there have been a number of explosion accidents involving structures of nuclear facilities and refinery plant facilities, which resulted in very severe damage to human lives and properties. This type of unexpected loading in the form of blast or impact may cause serious fire accidents as well. In order to prevent or reduce the damage from such unexpected loadings, innovation in the cement concrete technology is considered to be one of the most practical engineering solutions.

The HPFRCC is a recent development that can provide a possible solution for localized severe wide cracks [3] because of its unique ability to induce a number of finely

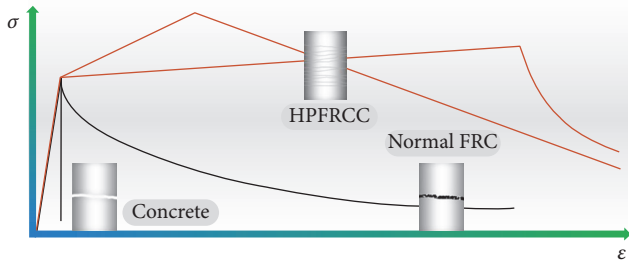


FIGURE 1: Pseudo-strain hardening behavior of HPRC.

distributed cracks. The other characteristics of HPRCCs include the crack width controlling capability by keeping the width within a permissible range. In addition, an appropriate use of its tensile performance can result in a structural component that is excellent in both durability and mechanical performance. Such materials are suitable in defense shelter blast proofing and retrofitting schemes and in structures that are routinely subjected to energy-intensive dynamic incidents [4]. The HPRCC functions as the most effective alternative to all other previous materials that were being used to resist high impact energy. Figure 1 shows the pseudo-strain hardening behavior of HPRCC in comparison with normal concrete and normal fiber reinforced concrete.

Further strengthening this high-performance concrete material would be a good move to make it a perfect structure that can resist various damaging factors. For this purpose, FRP can be applied to the HPRCC as protection against the external environment, fiber corrosion, and so forth. Moreover, the FRP can provide a greater durability and resistance to the HPRCC because of the externally bonded reinforcement [5].

Epoxy adhesives are used to bond FRPs to HPRCCs. The viscosity of epoxy adhesive is sufficient to hold the self-weight of the polymer. Furthermore, highly advanced manufacturing technologies can produce polymers with accurate alignment and minimum voids. However, there is a drawback—the reduction in ductility of the strengthened member. This loss in ductility has led to the formulation of various design guidelines for the external strengthening of FRP composites [6, 7].

The service life of a concrete structure is often shorter than planned. This is mainly due to environmental interactions that may occur. Because of its high strength and superior resistance against environmental agents, the use of the advanced basalt fiber-reinforced polymer (BFRP) as a structural reinforcement is a promising alternative, particularly as an externally bonded reinforcement for concrete structures [8]. Strengthening of concrete structures using the BFRP external reinforcement is an interesting topic, because studies of flexural strengthening with cement-based material as a bonding agent are relatively new, and therefore, it is important to investigate the suitability of such a material as a bonding agent. To achieve this, a full-scale test will be performed to demonstrate the actual behavior of the retrofitted structure in order to gain a better understanding of the performance of the system as a whole.

TABLE 1: Chemical composition and physical properties of cement and silica fume.

Chemical composition (%)	Cement	Silica fume
CaO	60.12	0.38
Al <sub>2</sub> O <sub>3</sub>	6.59	0.25
SiO <sub>2</sub>	21.95	96.00
Fe <sub>2</sub> O <sub>3</sub>	2.81	0.12
MgO	3.32	0.10
SO <sub>3</sub>	2.11	—
Particle size (cm <sup>2</sup> /g)	3,400	200,000
Specific gravity	3.15	2.10

## 2. Material Properties and Experimental Method

### 2.1. Materials

**2.1.1. Ordinary Portland Cement.** Ordinary Portland cement used in this experiment is one of the most widely used construction materials in civil engineering projects worldwide. This type of cement is made from calcareous materials such as limestone or chalk and from alumina and silica obtained as clay or shale. The major constituents of this cement are categorized into four compounds as shown in Table 1.

**2.1.2. Silica Fume.** Silica fume with the composition shown in Table 1 is an enhancer that substantially improves the mechanical properties. It is an extremely fine powder, with particles approximately 100 times smaller than cement. The particles of such a material pack tightly against the surface of the aggregate and fit in between the cement particles, greatly improving the packing [9].

**2.1.3. Steel Fiber.** The quantity of steel fibers required for a concrete mix is normally determined as a percentage of the total volume of the composite materials. The fibers are bonded to the material to produce a fiber-reinforced concrete that can withstand considerable stresses during the postcracking stage. The actual effect of the fibers is to increase the concrete toughness. The hooked end steel fiber used in this study which is shown in Figure 2 has a density of 7.8 g/cm<sup>3</sup>, length of 30 mm, diameter of 0.5 mm, aspect ratio of 60, and tensile strength of 1,200 MPa. It is used to improve the fracture toughness under the application of tensile and bending stresses.

**2.1.4. Superplasticizer.** To improve the workability of the concrete, a superplasticizer was added during the mixing operations. Superplasticizers, also known as high-range water reducers, are chemical admixtures used where well-dispersed particle suspension is required.

**2.1.5. Adhesive.** Strong adhesives are available for FRP plate bonding, and their strength generally exceeds that of the concrete. Therefore, failure in the adhesive is rare. However, if substandard adhesives are used or if adhesives are not properly applied, the failure may occur within the adhesive

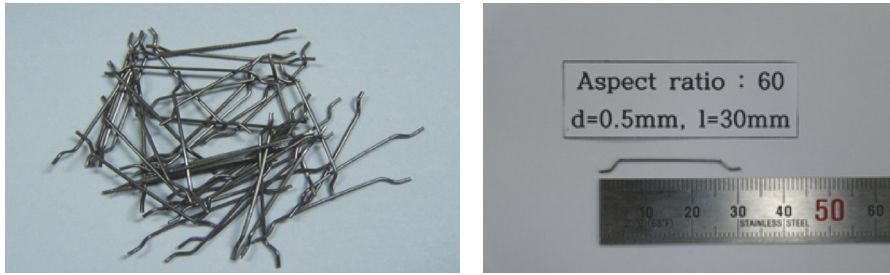


FIGURE 2: Type of steel fiber (hooked end).

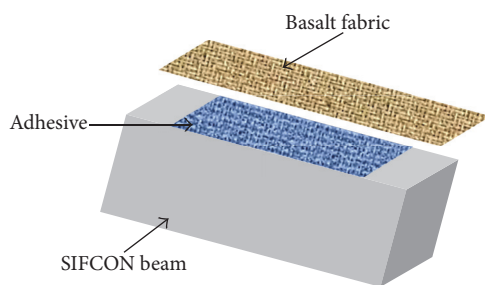


FIGURE 3: Single-layered basalt fabric applied over the HPFRCC beam with adhesive layer.



FIGURE 4: Basalt fiber sheet.

layer, adjacent to the adhesive-to-concrete interface, and adjacent to the FRP plate-to-adhesive interface [10–12]. The adhesive also acts as the matrix of the FRP, and this creates a strong bond with the beam. EFH 100S, EFR 100S, EFH 200S, and EFR 200S were used as adhesives in this experiment. Figure 3 shows the application of adhesive between the basalt sheet and HPFRCC beam.

**2.1.6. Basalt Fiber-Reinforced Polymer Sheet.** Figure 4 represents the basalt fiber sheet used in the study. Basalt (solidified volcanic lava) is known for its resistance to high temperatures, strength, and durability. BFRP is extruded from molten basalt rock at diameters generally between 13 and 20  $\mu\text{m}$ . It is environmentally and ecologically harmless and is free from carcinogens and other health hazards. Compared with other fiber polymers, BFRP is similar to carbon fiber and fiberglass. However, it has better physic-mechanical properties than fiberglass and is comparatively cheaper than carbon fiber. It is used as a fireproof textile in the aerospace and automotive industries. Basalt fiber has a superior range of thermal performance ( $-260^{\circ}\text{C}$  to  $960^{\circ}\text{C}$ ), and in addition, it has a

TABLE 2: Basalt fiber sheet properties.

Specific gravity	2.6
Tensile strength	2,500 MPa (360 ksi)
Elastic modulus	89 GPa (12,900 ksi)
Rupture strain	3.15%

TABLE 3: Experimental variables in slurry mix matrix.

Materials	Variables	Unit and remarks
W/B ratio	0.4	—
Silica fume	15	%, binder weight (cement replacement)
Fine aggregate content	50	%, binder weight
Superplasticizer	2.5	%, binder weight
Steel fiber	8	%, volume ratio

high tensile strength, high resistance to alkalis and acids, and excellent electromagnetic properties. Furthermore, it is inert and has a high resistance to corrosion, radiation, UV light, and good resistance to vibration [13]. Some relevant mechanical properties of basalt fibers are summarized in Table 2.

**2.2. Mixing Process.** The ordinary Portland cement, fine aggregate, water, superplasticizer, and additional silica fume were mixed to prepare the slurry. The water content was fixed using a binder-to-water ratio of 0.4. Silica fume is typically used to increase the strength and durability in the more densely packed microstructure of the cement matrix. For a better performance of the slurry, the ordinary Portland cement was replaced with silica fume by 15% in cement weight. To improve the performance and resistance to segregation, the weight ratio of cement to fine aggregate was fixed at 0.5 : 1. Furthermore, 2.5% (of the cement weight) superplasticizer was added [14]. Table 3 summarizes the experimental variables for an optimum mix proportion of the slurry matrix.

First, molds for flexural strength specimens with dimensions of  $100 \times 100 \times 400$  mm were filled with steel fiber at a volume fraction of 8%. The randomly sprinkled steel fibers should not overfill the depth of the mold, and the steel fibers should be leveled up as much as possible. The slurry, as prepared after mixing the contents, was poured from one end of the flexural beam in order to let it flow from one end to the other within the cluster of steel fiber. The slurry was poured

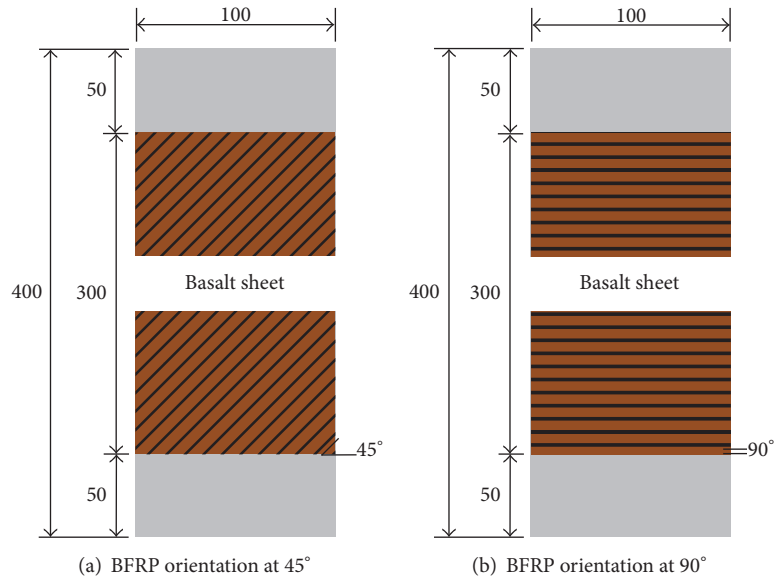


FIGURE 5: Top view of orientation of FRP sheets to the axis of beam (tension zone).

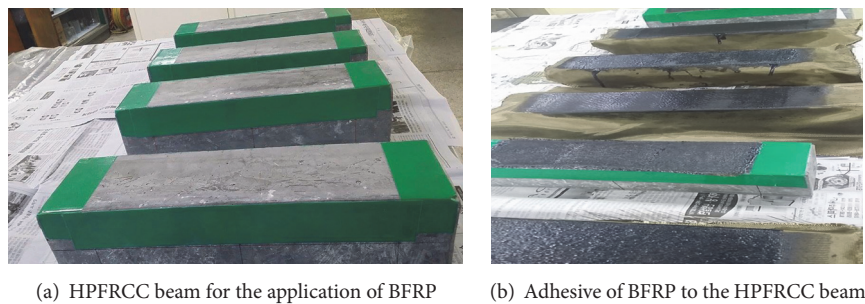


FIGURE 6: Ready-to-laminate and laminated beam with basalt sheet.

until bubbles were no longer observed to ensure infiltration of the slurry into the fibers as voids have a negative effect on the strength of concrete.

**2.3. Concrete Specimen Preparation.** After 24 h, the specimens were demolded and transferred to a curing container. After curing the specimen for 28 d under a normal laboratory temperature of 23°C, the specimens were taken out for the next process. A basalt fabric was cut with a dimension of 100 mm × 300 mm with respect to the strip orientation of 45° and 90° angles. An adhesive was used to bind the beam surface with the fabric. We have prepared a total of nine variables from a single, double, and triple layer of basalt sheet laminated on the lower surface of the beam. Specimens were left for several days to ensure that the adhesive was perfectly set to bond the fabric with the beam surface, and then the next testing process was implemented. Here, Figure 5 shows the two different orientations of FRP sheets attached to the axis of beam in the tension zone and Figure 6 shows laboratory process of preparation and adhesion of BFRP sheet in the HPFRCC beam. Table 4 represents all the fiber orientation and combination that has been applied for research in this study.

**2.4. Flexural Strength and Toughness Test.** Figure 7 shows the four-point bending test performed in the laboratory and failure in the beams under the loading. The 100 × 100 × 400 mm flexural strength test specimens with 100 × 300 mm basalt fabric bonded at the bending zone with different layers and fiber orientation were tested under a four-point bending test configuration following ASTM C1609, flexural testing of fiber-reinforced concrete beams. The method for conducting the test usually involves a specified test fixture on a universal testing machine (UTM). Specimens were loaded at four points by a 200-ton-class UTM, where the loaded power was applied by the displacement control at a speed of 1 mm/min [15]. Details of the test preparation, conditioning, and procedure affect the test results. The vertical deflection was measured using Japanese yoke linear variable differential transformers on both sides simultaneously with the applied loading. A highly sensitive data logging instrument was used to collect the precise data for further analysis.

### 3. Test Result Analysis and Discussion

**3.1. Flexural Strength and Toughness.** The attachment of FRP sheet with adhesives is used to increase the flexural strength,



FIGURE 7: Load testing and failure under load.

TABLE 4: Variable specimens.

Layer	Fiber orientation	Layup
Single	45° 90°	
Two	90°-90° 45°-45° 90°-45°	
Three	90°-90°-90° 90°-45°-90° 45°-90°-45° 45°-45°-45°	

shear strength, and, to an extent, the flexural stiffness of the existing conventional slurry infiltrated fibrous concrete (SIFCON) beam. It is well known that the addition of the FRP external reinforcement decreases the deformity, that is, the deflection and curvature of failure of the member, and that the failure is brittle. Almost all the variable specimens showed a concrete failure. Compressive crushing of concrete was the dominant failure mode in all three layers of basalt retrofitted HPRCC beams. The test results of flexural strength and the flexural toughness of the specimens are shown in Figures 8 and 9, respectively.

Flexural toughness was calculated by using the load-deflection graph of each variable. The limitation of ASTM C1609 was already considered, where the toughness was compared with the area under the curve up to a deflection of 15 mm (versus  $L/20$ ) [16].

3.1.1. *HPFRCC Beam without BFRP*. Figure 10 shows the load-mid span deflection curves of HPFRCC beams without BFRP. The result of the specimen without BFRP retrofit is the normal condition specimen. With respect to this result, the variable specimens with BFRP retrofit were compared.

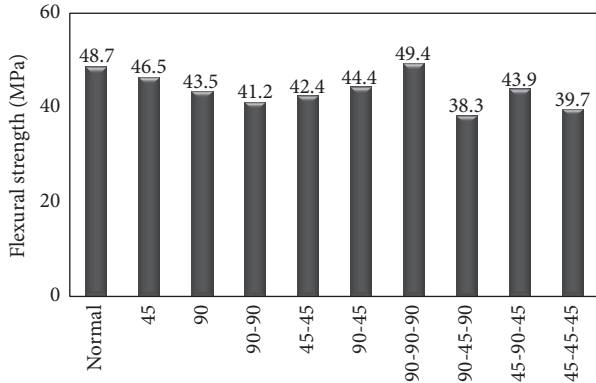


FIGURE 8: Flexural strength of the BFRP HPFRCC beam.

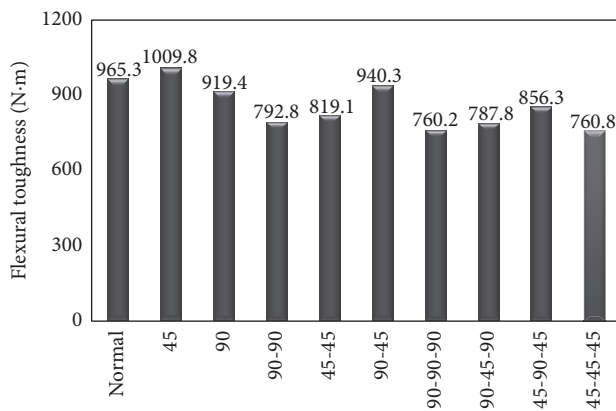


FIGURE 9: Flexural toughness of the BFRP HPFRCC beam.

Based on the research target, specimens retrofitted with layers of BFRP were expected to achieve better results. Here, the average flexural strength of the normal specimen was 48.7 MPa, where the toughness calculated from the load-deflection curve was 965.3 N·m. The HPFRCC beam with a steel volume fraction of 8% is considered as a high strength concrete, and there are no differences in the strength and toughness.

**3.1.2. Single-Layered BFRP HPFRCC Beam.** Figure 11 shows the load-mid span deflection curves of single-layered BFRP HPFRCC beams. Beams with single-layered basalt polymer at different fiber angle orientations showed almost similar results. By examining the numerical values, the specimen with a 45° fiber orientation, which has a toughness of 1009.8 N·m, is observed to have the highest value compared with the others. The two single-layered specimens with different fiber orientations have better results compared with other specimens. Here, the specimen retrofitted with 45° single-layer BFRP showed a higher value in comparison with the 90°. The optimum orientation of the FRP strips, as determined by Pantelides et al. (1999) [17], is 45° owing to the cyclic nature of earthquakes. The fiber orientation at 45° provided in both diagonal directions showed a better stiffness. The fiber orientation at 45° provided in both diagonal direction orientations would limit the stiffness and

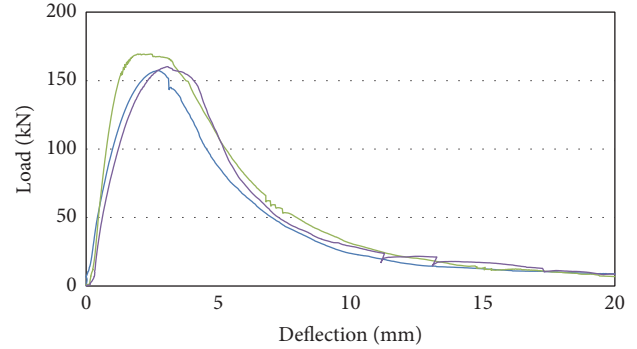


FIGURE 10: Load-mid span deflection curves of HPFRCC beam without BFRP.

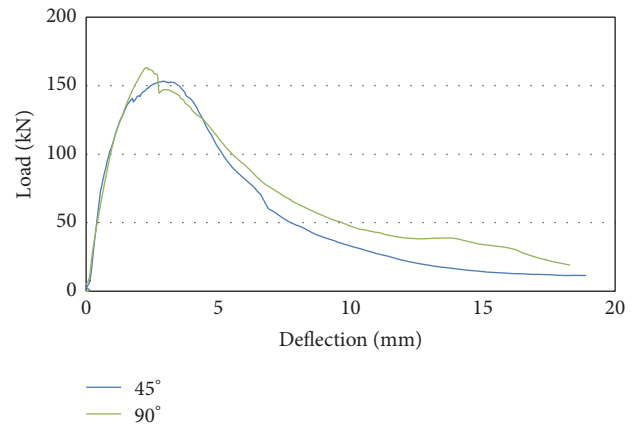


FIGURE 11: Load-mid span deflection curves of single-layered BFRP HPFRCC beam.

improve the shear capacity thus resulting in much more ductile behavior and increased toughness. The more ductile behavior exhibited by the specimen reinforced with 45°-oriented BFRP could probably be due to the enlargement of the failure zone associated with the stress redistribution.

**3.1.3. Double-Layered BFRP HPFRCC Beam.** Figure 12 shows the load-mid span deflection curves of double-layered BFRP HPFRCC beams. By close comparison, the specimen bonded with a 45°-oriented basalt fiber sheet showed better results in both cases. The flexural strength and toughness of the specimen bonded with different directions of basalt fiber sheets showed a comparatively better result (90-45). Here, the HPFRCC beam when retrofitted with 90°- and 45°-oriented basalt fiber (i.e., specimen 90-45) showed a better toughness in comparison with that of the other specimens. This toughness of 940.3 N·m was one of the better specimens. This combination of layering basalt sheet can be a better option for an improved result. From the result, it was found that the specimen reinforced with 45°-oriented fiber specimen showed a better result than other layered combinations in the same category. Here, the increase in toughness and flexural strength is observed in the hybrid type of specimen (90-45) because the fiber orientation directly impacts the

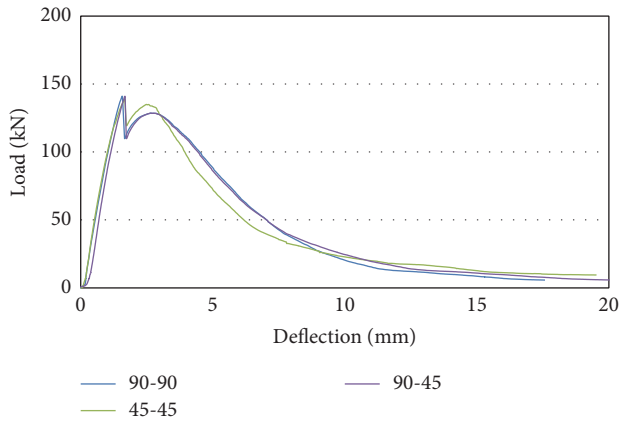


FIGURE 12: Load-mid span deflection curves of double-layered BFRP HPFRCC beam.

mechanical properties; therefore, it was logical to orient as many layers as possible to the main load-carrying direction. While this approach may work for some structures, it is usually necessary to use different directions with the hybrid type laminate. This type of combination of FRP layers carries an equal load in all four directions.

**3.1.4. Three-Layered BFRP HPFRCC Beam.** Figure 13 shows the load-mid span deflection curves of three-layered BFRP HPFRCC beams. Surprisingly, the three-layered beam specimens showed relatively different results. A remarkable difference was observed with the specimen, 90-90-90, which has the highest flexural strength and lowest toughness. Almost all the three-layered BFRP beam specimens showed similar flexural toughness except the variable, 45-90-45. Comparatively, the toughness was lower in value with that of the single- and double-layered specimens. This is an important issue to be considered—even a higher number of layers could result in lower toughness. Here, the specimen with 45°-oriented basalt fiber sheet when laminated in an alternative layer (45-90-45) showed an increased toughness compared with the other three-layered basalt retrofitted variables. The irregular result could be due to the increase in strength, and stiffness is sometimes realized at the expense of a loss in ductility or the capacity of the structure to deflect in elastically while sustaining a load close to its capacity. The test result was similar with that of the double-layered BFRP specimen, when compared with the hybrid type of lamination. The specimen laminated in an alternative layer (45-90-45) had an increased toughness.

**3.2. Discussion.** A beam that failed by concrete crushing when a large quantity of FRP is used also shows a greatly reduced ductility (Buyukozturk and Hearing, 1998 [18]) [19]. The test results showed that the strength and toughness of the HPFRCC beam decreased with increasing number of BFRP layers. The forces in the FRP sheets/strips are directly proportional to the diagonal compressive stresses developed in the concrete struts. When these stresses exceed the concrete compressive strength, crushing of the concrete occurs. This failure is highly dependent on the crack angle and the FRP fiber orientation. The flatter the crack angle, the larger the

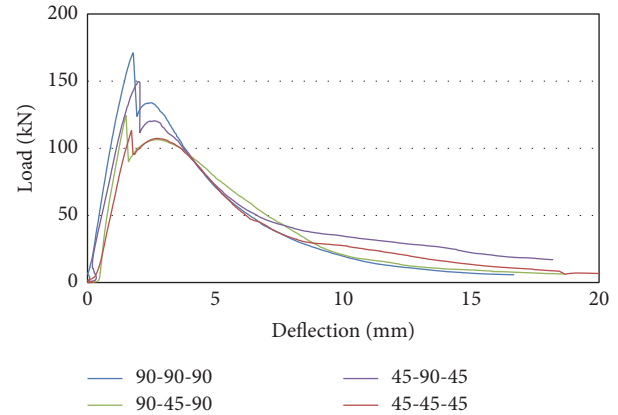


FIGURE 13: Load-mid span deflection curves of three-layered BFRP HPFRCC beam.

stresses developed. The FIB (Federation Internationale du Beton) Bulletin, FRP Reinforcement for Concrete Structure (2002) [20], noted that if the design is governed by the serviceability limit state, the quantity of FRP added into the structure may be considerably higher than what is required for the ultimate limit state.

In this case, it may be difficult to achieve the ductility requirement. Here, the SIFCON, which is already a high-strength concrete and was further reinforced externally by the BFRP, could be the reason behind the decrease in strength and toughness. Another reason could be that the failure mode of the specimen was in the concrete crushing of the beam, where the single-layered specimen showed a better flexural performance compared with the others. Therefore, the capacity is dependent on the strength of the concrete and shape of the specimens, and the failure is in the concrete rather than in the FRP-concrete interface.

Consequently, the strength decreased with the increased number of BFRP sheets. Although these are some of the result outputs worthy of discussion, the flexural performance and failure mode of the FRP concrete interface depend not only on the FRP sheet, fiber orientation, and layering but also on the stiffness, bond length, surface treatment, concrete strength, and adhesive layer stiffness, which are important factors that should be taken into consideration. Ductility index is used as the basis to evaluate the material behavior that represents the ability of a concrete beam to undergo a large deformation while maintaining its load-resisting capacity or a significant portion of it. It indicates the capability of the material to absorb and dissipate energy by postdeformation. Hence, the higher the ductility index, the better the performance.

## 4. Conclusion

This study is based on existing research work on HPFRCC beams strengthened by externally laminated BFRP in the tensile zone. Since the HPFRCC is already a high-strength concrete, the importance of this study was to further strengthen the HPFRCC by using a BFRP laminate.

- (1) Among the three different variable combinations, the single-layered 45°-oriented basalt fiber sheet reinforcement was the best method to strengthen the HPFRCC beam structure.
- (2) From the test result, it was interesting to note that increasing the quantity of external reinforcement by increasing the BFRP thickness or layers does not always increase the maximum load ratio. Even the single-layered basalt retrofitted specimen showed better toughness in comparison with the other multilayered specimen. This means that more research is required on this field of improving the strength of HPFRCC retrofitted with multilayers of external basalt polymer.
- (3) In the two-layer combination, different directions of basalt fiber sheet reinforcement showed higher toughness compared with other types. Moreover, the case was similar to the three-layer combination. The toughness improved when the 45°-oriented basalt fiber sheets were alternatively bonded with 90°-oriented basalt fiber sheets in two- and three-layered basalt reinforced beam (90-45 and 45-90-45).
- (4) The decreasing strength value with the addition of FRP could be due to the reduced ductility. Strength and toughness are directly proportional to the ductility of the confinement, and we could relate this result with the overreinforcement, which reduces the ductility as well. The confinement with basalt fiber in hybrid orientation showed a better result because the load is distributed in all directions.
- (5) Single-layered 45°-oriented basalt fibers limited the reinforcement and controlled the ductility as they provided stiffness in both diagonal directions. In conclusion, single-layered 45°-oriented basalt fiber sheet reinforcement is the most appropriate combination for strengthening an HPFRCC beam; in addition, it has a low installation time and is also economical.

## Competing Interests

The authors declare that they have no competing interests.

## Acknowledgments

This research was supported by a grant from a Construction Technology Research Project (development of impact/blast resistant HPFRCC and evaluation technique thereof, 13SCIPS02) funded by the Ministry of Land, Infrastructure, and Transport.

## References

- [1] L. Ostergaard, R. Walter, and J. F. Olesen, "Method for determination of tensile properties of engineered cementitious composites (ECC)," in *Proceedings of the 3rd International Conference on Construction Materials, Performance, Innovations and Structural Implications*, Vancouver, Canada, 2005.
- [2] Country Reports on Terrorism 2010 [Internet]. State.gov, 2011, <http://www.state.gov/j/ct/rls/crt/2010/>.
- [3] J. Zhang and H. Stang, "Applications of stress crack width relationship in predicting the flexural behavior of fibre-reinforced concrete," *Cement and Concrete Research*, vol. 28, no. 3, pp. 439–452, 1998.
- [4] A. Naaman, "High performance fibre reinforced cement composites," in *High Performance Construction Materials*, C. Shi and Y. Mo, Eds., Science and Applications, pp. 91–154, 1st edition, 2008.
- [5] A. Naaman and H. Reinhardt, "High performance fiber reinforced cement composites HPFRCC-4: international workshop Ann Arbor, Michigan, June 16–18, 2003," *Cement and Concrete Composites*, vol. 26, no. 6, pp. 757–759, 2004.
- [6] P. Balaguru, A. Nanni, and J. Giancaspro, *FRP Composites for Reinforced and Prestressed Concrete Structures*, Taylor & Francis, New York, NY, USA, 2009.
- [7] H. GangaRao, N. Taly, and P. Vijay, *Reinforced Concrete Design with FRP Composites*, CRC Press, Boca Raton, Fla, USA, 2007.
- [8] H. He and W. Dong, "Study on damaged reinforced concrete beams strengthened with basalt fiber polymer sheets," *Advanced Materials Research*, vol. 446-449, pp. 2941–2944, 2012.
- [9] R. Siddique and M. Khan, *Supplementary Cementing Materials*, Springer, Heidelberg, Germany, 2011.
- [10] U. Meier, "Strengthening of structures using carbon fibre/epoxy composites," *Construction and Building Materials*, vol. 9, no. 6, pp. 341–351, 1995.
- [11] V. M. Karbhari and L. Zhao, "Issues related to composite plating and environmental exposure effects on composite-concrete interface in external strengthening," *Composite Structures*, vol. 40, no. 3-4, pp. 293–304, 1997.
- [12] Leeming and Darby, *Design and Specifications for FRP Plate Bonding of Beams: Chapter 9 of Strengthening of Reinforced Concrete Structures Using Externally-Bonded FRP Composites*, Woodhead, Cambridge, UK, 1999.
- [13] J. Sim, C. Park, and D. Y. Moon, "Characteristics of basalt fiber as a strengthening material for concrete structures," *Composites Part B: Engineering*, vol. 36, no. 6-7, pp. 504–512, 2005.
- [14] S. Kim, C. Park, S. Kim, H. Cho, S. Jeon, and M. Ju, "Optimum mix proportions of in-fill slurry for high performance steel fiber reinforced cementitious composite," *Journal of the Korean Recycled Construction Resources Institute*, vol. 2, no. 3, pp. 196–201, 2014.
- [15] S. Kim, H. Cho, H. Lee, and C. Park, "Flexural performance characteristics of high performance slurry infiltrated fiber reinforced cementitious composite according to fiber volume fraction," *Journal of the Korea Institute for Structural Maintenance and Inspection*, vol. 19, no. 4, pp. 109–115, 2015.
- [16] S. Kim, H. Ban, M. Ju, H. Cho, and C. Park, "Performance fiber reinforced cementitious composites under mode I fracture," in *Proceedings of the 5th International Conference on Design and Analysis of Protective Structures (DASP '15)*, pp. 975–981, Singapore, 2015.
- [17] C. P. Pantelides, J. Gergely, L. D. Reaveley, and V. A. Volnyy, "Retrofit of RC bridge pier with CFRP advanced composites," *Journal of Structural Engineering*. ASCE, vol. 9, no. 4, pp. 1094–1099, 1999.
- [18] O. Buyukozturk and B. Hearing, "Failure behavior of precracked concrete beams retrofitted with FRP," *Journal of Composites for Construction*, vol. 2, no. 3, pp. 138–144, 1998.
- [19] S. Kim and C. Park, "Mechanical properties of high performance fiber reinforced composite with high steel fiber volume fraction," in *Fibre Concrete 2015*, Czech Technical University in Prague, Prague, Czech Republic, 2015.

- [20] "Recommendations of RILEM TC 162-TDF: test and design methods for steel fibre reinforced concrete: bending test," *Materials and Structures*, vol. 35, no. 253, pp. 579–582, 2002.

## Research Article

# Bending and Shear Experimental Tests and Numerical Analysis of Composite Slabs Made Up of Lightweight Concrete

F. P. Alvarez Rabanal,<sup>1</sup> J. Guerrero-Muñoz,<sup>2</sup>  
M. Alonso-Martinez,<sup>1</sup> and J. E. Martinez-Martinez<sup>1</sup>

<sup>1</sup>Construction and Manufacturing Department, University of Oviedo, Gijón, Spain

<sup>2</sup>Advanced Simulation Technologies, S.L. Parque Científico Tecnológico de Gijón, Gijón, Spain

Correspondence should be addressed to M. Alonso-Martinez; mar@constru.uniovi.es

Received 23 September 2016; Accepted 23 November 2016

Academic Editor: Peng Zhang

Copyright © 2016 F. P. Alvarez Rabanal et al. This is an open access article distributed under the Creative Commons Attribution License, which permits unrestricted use, distribution, and reproduction in any medium, provided the original work is properly cited.

The aim of this paper is to understand the structural behaviour of composite slabs. These composite slabs are made of steel and different kinds of concrete. The methodology used in this paper combines experimental studies with advanced techniques of numerical simulations. In this paper, four types of concrete were used in order to study their different structural strengths in composite slabs. The materials used were three lightweight concretes, a normal concrete, and a cold conformed steel deck which has embossments to increase the adherence between concrete and steel. Furthermore, two lengths of slabs were studied to compare structural behaviours between short and long slabs.  $m-k$  experimental tests were carried out to obtain the flexural behaviour of the composite slabs. These tests provide dimensionless coefficients to compare different sizes of slabs. Nonlinear numerical simulations were performed by means of the finite element method (FEM). Four different multilinear isotropic hardening laws were used to simulate the four concretes. Coulomb friction contact was used to model the coefficient of friction between steel and concrete. Finally, a chemical bond was included to consider sliding resistance in the contact surface between steel and concrete. Experimental and numerical results are in good agreement; therefore, numerical models can be used to improve and optimize lightweight composite slabs.

## 1. Introduction

Composite slabs are made up of a thin steel sheet and concrete. Reinforced bars are often needed inside the composite layer in order to reduce shrinkage as well as avoid/prevent bending stress [1]. Stress analysis of composite slabs shall consider two phases:

- (i) Implementation phase, in which the steel sheet works as a framework. In this phase, the steel sheet must withstand transmitted loads of fresh concrete.
- (ii) Service phase, in which concrete and steel work together to support stress. Efficiency of the composite slab depends on the interaction between the concrete layer and the steel sheet.

In this paper, new composite slabs made up of steel deck and lightweight concrete are studied. Composite slabs are efficient

and versatile elements [2, 3], but the advantages of composite slabs made of lightweight concrete (LWC) and steel make them especially suitable for industrial applications [4].

Firstly, composite slabs made of LWC and steel are very efficient due to the combination of these two materials, steel and concrete. The tensile strength of steel and the compressive strength of concrete provide increased slab stiffness. Secondly, the weight of these composite slabs is reduced due to the use of lightweight concrete. This advantage makes transport and storage easier, as well as reducing foundation size. Thirdly, these composite slabs are manufactured in an industrialized process and a higher quality is achieved. Furthermore, the construction process with precast concrete is easier and faster. Fourthly, the materials used are recyclable. This enhances the product life and makes the use of composite slabs a sustainable process. Finally, composite slabs made of lightweight concrete are more economical than traditional

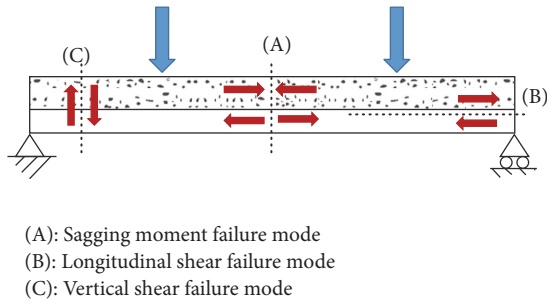


FIGURE 1: Failure modes of composite slabs.

slabs. They use less concrete, do not require an auxiliary framework, and reduce the weight of the structure, among other benefits.

Structural analysis of composite slabs is based on their failure modes. The main failure modes of composite slabs are due to bending stress and longitudinal displacement:

- (i) Failure mode due to “*sagging moment*” which is related to the bending resistance of the composite slab, Figure 1(A).
- (ii) Failure mode of “*longitudinal shear*” because the contact between steel and concrete reaches the ultimate shear load resistance, Figure 1(B).

*Sagging moment* is usually the main failure mode of large and thin slabs where shear stress is low compared to bending stress. *Vertical shear* stress is usually lower than the others, so it is rarely the main failure mode.

In order to study the structural behaviour of composite slabs, the connection between steel and concrete must be studied. Chemical adhesion has been studied by other authors through *m-k* tests [6].

The stress transfer between LWC and steel depends on both mechanical and frictional interaction. The resistance of this contact is obtained by *m-k* tests which are specified in Eurocode 4 [5]. Shear stress of composite slabs can be determined by this European Standard. However, theoretical prediction of composite slabs is very difficult because it depends on many variables, such as the geometry of steel deck and embossments.

*m-k* tests determine relative displacement between the steel sheet and the concrete when shear stress is applied to the composite slab. In this test, a cyclic load is applied in order to take into account the whole life cycle of the composite slabs before collapse. The application of this cyclic load is required to break the chemical bond between the steel and the LWC. In this way, other failure modes in the slabs can be identified.

Other authors have studied the efficiency of *m-k* tests to determine the bending behaviour of composite slabs [1–4, 6, 7]. These studies identify important considerations to achieve successful results in *m-k* tests, such as the introduction of crack initiators in concrete, the influence of the thickness of the steel sheet, or the influence of cyclic preloads applied. The conclusions reveal a reduction in strength due to crack initiators. However, current standards take them into account because they contribute to the control of the slab breakage.

The results show the low influence of the chemical bond between concrete and steel, while embossments, coefficient of friction, and mechanical connectors guarantee suitable interaction between concrete and steel.

*m-k* experimental tests are based on four point bending tests. The main results show the ductile behaviour of concrete as well as a 20% of weight reduction. However, some disadvantages are presented such as a reduction of the strength capacity due to the use of LWC instead of normal concrete [8, 9].

The original contribution of this paper is the study of the structural behaviour of composite slabs made of structural lightweight concrete instead of normal concrete. Furthermore, this LWC is reinforced with polyolefin fibres in order to reduce shrinkage stress.

## 2. Materials and Methods

**2.1. Materials.** Initially, lightweight aggregates were obtained from natural resources, mainly of volcanic origin: pumice, slag, volcanic tuff, and so forth. The lack of natural resources and the increment in the demand for lightweight aggregates made industrial processes to manufacture aggregates necessary. These aggregates include expanded clay, schist, and slate, as well as industrial byproducts such as fly ash and dust from blast furnace. The properties of these aggregates depend on the raw materials and the manufacturing processes.

Lightweight aggregates of different densities can be manufactured ranging from 50 kg/m<sup>3</sup> for expanded perlite to 1000 kg/m<sup>3</sup> for clinker. The compressive strength obtained for LWCs can be increased up to 80 MPa for cubic specimens with the addition of these aggregates and high-effect additives which reduce the amount of water required. The low density of this material provides high thermal insulation in buildings, up to 6 times higher than normal concrete [10].

In this paper, the aggregate used is an expanded clay called “arlite.” The main properties of this material are good insulation, porosity, and resistance. Arlite is usually employed to manufacture high-performance ultralight mortars. In order to compare the differences between LWC and normal concrete, four different types of concrete have been studied. Three of them are LWCs made of arlite with different densities and the fourth is normal concrete. These materials are henceforth referred to in the paper as

- (i) Normal concrete (HN)
- (ii) Structural lightweight concrete type 23 (LWC.LSDur-23)
- (iii) Structural lightweight concrete type-28 (LWC.LSDur-28)
- (iv) Structural lightweight concrete type-37 (LWC.LSDur-37).

The properties of these materials are included in Table 1 and have been determined following the National Standards UNE-EN 12390-3 [11] and UNE-EN 12390-13 [12].

The Spanish Standard for composite slabs made of steel deck and structural concrete is the Eurocode 4 [5]. This

TABLE 1: Mechanical properties of studied concrete.

Concrete type	Density	Compressive strength (MPa)	Young's modulus (MPa)
LWC.LSDur-23	1875	25,60	$2,07 \cdot 10^4$
LWC.LSDur-28	1902	28,59	$2,16 \cdot 10^4$
LWC.LSDur-37	2010	30,22	$2,72 \cdot 10^4$
HN	2435	36,97	$4,57 \cdot 10^4$

TABLE 2: Mechanical properties of the ribbed steel sheet obtained in tensile tests.

	1	2	3	Average
Elastic modulus (MPa)	268	275	271	271.33
Young's modulus (GPa)	206	204	210	208
Poisson coefficient	0.31	0.33	0.31	0.31

standard is based on the repealed British Standard BS5950, as well as other previous standards regarding service analysis, brittleness, and ductility.

To determine the properties of the steel used, tensile tests on 3 specimens of the same material were developed following the National Standard (UNE-EN-ISO-6892-1) [13]. The results obtained are shown in Table 2.

From the average of the experimental results, the curve *engineering stress-strain* is obtained. Then, *true stress-strain* is obtained as shown in Figure 2.

**2.2. Experimental Tests.** The *m-k* test measures the maximum load that a composite slab is able to withstand before breakage occurs because of shear stress between the concrete and the steel sheet. Shear failure causes relative sliding between steel and concrete so that the two elements do not work together any longer.

The load applied in this test is a distributed load in two lines located  $L/4$  from the ends of the composite slabs (see Figure 3). After applying the load incrementally, slab longitudinal shear or sagging moment failure occurs.

The test procedure is as follows:

- (i) Firstly, the composite slab is weighted until breakage to obtain the maximum fracture load.
- (ii) Secondly, a cyclic load ranging from 20% to 60% of the maximum fracture load is applied for 5000 cycles.
- (iii) Finally, a continuous and ever-increasing load is applied until the slab breaks. The total time of the *m-k* test must be longer than 3600 seconds. In this test, the ultimate load ( $W_t$ ) is obtained, as well as the vertical displacement of the center of the slab ( $f$ ) and the sliding between concrete and steel ( $dL$ ).

A total of 16 tests were carried out: four types of concrete were studied, three LWCs and the fourth NC, for two different lengths of slabs,  $2610 \times 1120 \times 160$  mm and  $2030 \times 1120 \times 160$  mm.

Displacement transducers were used to measure the relative displacement between concrete and steel and also

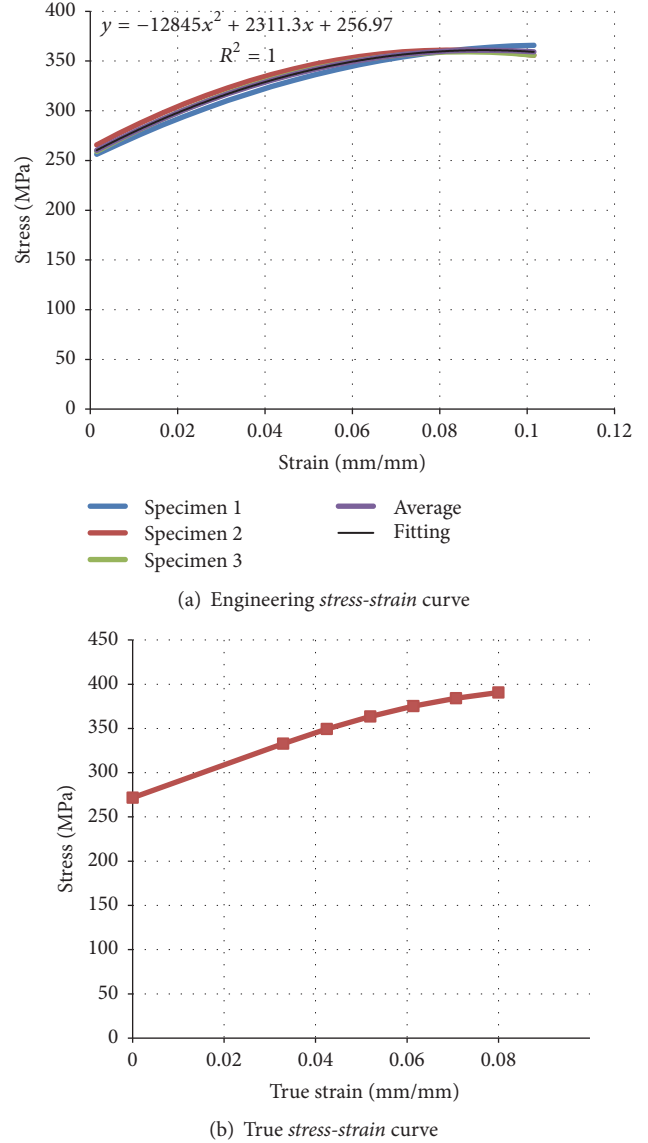


FIGURE 2: Engineering and true stress-strain curves.

the deflection of the slab. Furthermore, the load applied was recorded. Thus, the graphs "load-deflection" and "load-slip" for each slab tested were obtained. *m-k* coefficients provided slab strength [5, Annex B].

Once the *m-k* coefficients are calculated, the shear strength for any geometry of each slab type can be obtained using the following equation:

$$V_c = \frac{b \cdot d_p \cdot [m(A_p / (b \cdot L_s)) + k]}{\gamma_v}, \quad (1)$$

where  $V_c$ : is the shear resistance (N).  $b$  is the width of slab (mm).  $d_p$  is the distance between the centroidal axis of the steel sheeting and the extreme fibre of the composite slab in compression (mm).  $m$ ,  $k$  are design values for the empirical factors obtained from slab tests meeting the basic requirements of the *m-k* method ( $N/mm^2$ ).  $A_p$  is the nominal

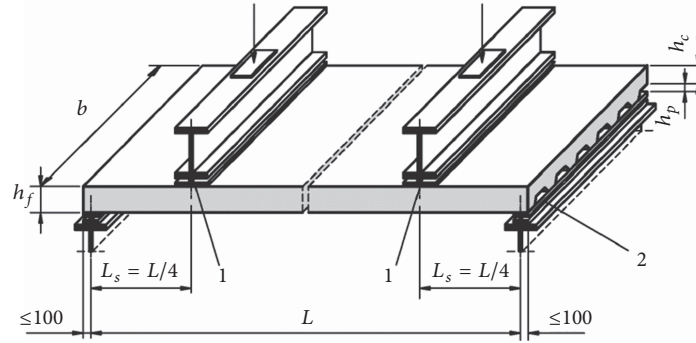


FIGURE 3: *m-k* test configuration [5, Annex B]. “1” refers to a neoprene support. “2” refers to a steel plate support.

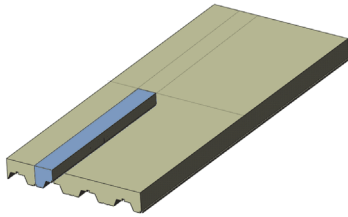


FIGURE 4: Composite slab geometry for *m-k* test. Detail of modelled geometry (in blue).

TABLE 3: Finite element mesh properties.

Composite slab length (mm)	Number of elements	Number of nodes	Mesh quality
2030	286451	261619	0.87
2610	362945	335258	0.83

cross section of the sheeting ( $\text{mm}^2$ ).  $L_s$  is the shear span defined in Figure 3 (mm).  $\gamma_v$  is the partial safety factor for the ultimate limit state [5].

The results obtained regarding shear resistance depend on the length of the slab; see Table 4.

**2.3. Numerical Analysis.** Two different FEA models were built, both for short (2030 mm) and long (2610 mm) composite slabs. In order to reduce computational costs, a simplified model was used, corresponding to 1/16 of the geometry of the slab, applying symmetry boundary conditions on the cutting planes (see Figure 4).

The steel deck was modelled using 4-node shell elements (SHELL181), while 8-node solid elements (SOLID185) were used to model the concrete slab (see Figure 5(a)) [14]. The mesh density was increased in the contact area between both materials (see Figure 5(b)). The main features of the mesh used for each model are included in Table 3.

The following boundary conditions were applied:

- (1) Symmetry boundary conditions at the model cutting planes (see Figure 6(a)).
- (2) Vertical displacement constrained ( $U_Y = 0$ ) at support (see Figure 6(b)).

TABLE 4: Values of equivalent shear stress obtained in pull-out tests.

Concrete type	$\tau_d$ (MPa)
LWC.LSDur-23	0.106
LWC.LSDur-28	0.124
LWC.LSDur-37	0.162
HN	0.243

TABLE 5: Summary of load steps introduced in the FEA model.

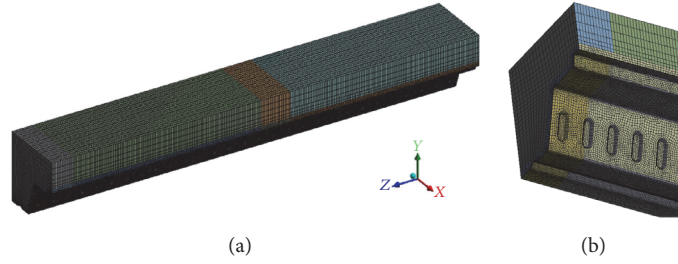
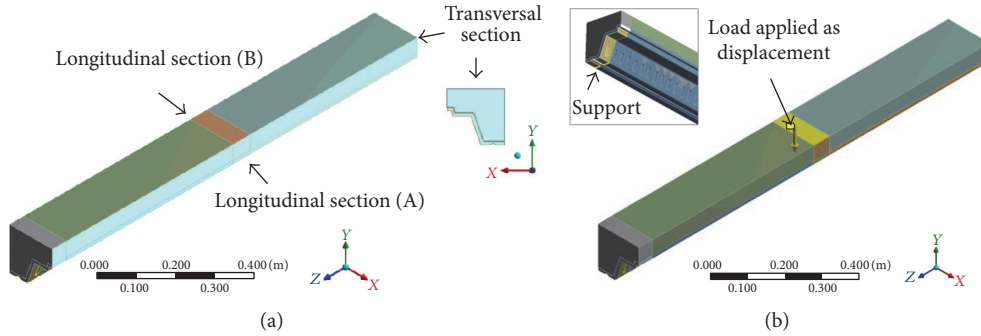
	Load step 1	Load step 2	Load step 3
Time step (s)	$2 \times 10^{-5}$	$1 \times 10^{-3}$	$1 \times 10^{-3}$
Max. time (s)	0.1	0.1	0.1
Force convergence (%)	2	Default	Default

- (3) Load applied incrementally as displacement at the top surface of the slab (see Figure 6(a)).

The simulations carried out were gradually increased in complexity until achieving good agreement with the empirical results. Specifically, the material laws of both steel and concrete were modified to produce more realistic results, from simple to complex: Initially, linear-elastic material models were used to characterize their behaviour. In a second step, strain-hardening material models were used, with better results than the former. Finally, and initial chemical bond (adhesion) between steel and concrete was also introduced, which produced the best correlation with the test results. The configuration of the load steps in the FEA model are shown in Table 5.

The numerical model takes into account the plastic behaviour of both steel and concrete, using multilinear isotropic hardening laws. The stress-strain data is required to implement the materials models. Steel strength was obtained from tensile tests of 3 specimens from the steel deck, as mentioned in Section 2.1 (see Table 1). The stress-strain data for the different types of concrete are determined using the formulae provided in articles 15 (materials) and 39 (characteristics of concrete) from the Spanish code EHE [15], adjusting the curves with the results obtained experimentally.

$$f_{cd} = \alpha_{cc} \cdot \frac{f_{ck}}{\gamma_c}, \quad (2)$$

FIGURE 5: Composite slab model for  $m-k$  test. Mesh detail.FIGURE 6: Boundary conditions applied on  $m-k$  model.

where  $\alpha_{cc}$  is the factor which takes account of the fatigue in the concrete when it is subjected to high levels of compression stress due to long duration loads. The EHE-08 Standard recommends  $0.85 \leq \alpha_{cc} \leq 1$ .  $f_{ck}$  is the characteristic design strength (MPa).  $\gamma_c$  is the safety coefficient for ultimate limit state (ULS). In the case of concrete,  $\gamma_c = 1.5$ .

The relation stress-strain can be determined with the following equations [15]:

$$\sigma_m = f_{cd} \cdot \left[ 1 - \frac{\varepsilon_m}{\varepsilon_{co}} \right]^n + \sigma_{m-1}, \quad \text{If } 0 \leq \varepsilon_c \leq \varepsilon_{co}, \quad (3)$$

$$\sigma_m = f_{cd}, \quad \text{If } \varepsilon_{co} \leq \varepsilon_c \leq \varepsilon_{cu},$$

where  $\sigma_m$  is the stress of the point  $m$  (in MPa).  $\varepsilon_m$  is the strain of the point  $m$  (in mm/mm).  $\varepsilon_{co}$  is the maximum compressive strain in the concrete under simple compression (in mm/mm).  $\varepsilon_{co} = 0.002$  if  $f_{ck} \leq 50$  MPa.  $\varepsilon_{cu}$  is the ultimate bending strain (in mm/mm)  $\varepsilon_{cu} = 0.0035$  if  $f_{ck} \leq 50$  MPa.  $n$  is the exponent of the parabola  $n = 2$  if  $f_{ck} \leq 50$  MPa.

Following previous equations, stress-strain curves of concrete are included in the numerical simulation (see Figure 7). A multilinear isotropic hardening is included in the numerical model to simulate actual concrete behaviour.

Furthermore, the Coulomb friction contact model was used at the contact areas between concrete and the steel deck. As main characteristics, an asymmetric contact was selected, using a friction coefficient of 0.3.

Additionally, the chemical bond between steel and concrete was simulated in the model by introducing some sliding resistance. In this way, the contacting surfaces carry shear stresses up to a certain magnitude across their interface before they start sliding relative to each other. The equivalent shear

stress  $\tau$ , at which sliding on the surface begins as a fraction of the contact pressure  $p$ , is calculated with the following equation:

$$\tau = \mu p + \text{COHE}, \quad (4)$$

where  $\mu$  is the friction coefficient and COHE is the cohesion sliding resistance.

If the pressure applied provides enough shear stress, sliding between concrete and steel starts. The values for the shear stress at which sliding begins ( $\tau_d$ ) were estimated from the results obtained in pull-out tests carried out on reduced specimens of the composite slabs under study. These were the basis for the posterior adjustment of the models [16].

The analysis was divided into 3 load steps, where the load, applied as a remote displacement, was incremented gradually up to 6 mm for long slabs and 3-4 mm for short slabs, using small time steps.

### 3. Results and Comparison

The results of experimental tests and numerical analysis are included in this chapter. Finally, a numerical and experimental comparison is presented in order to validate numerical simulations as well as obtain a good agreement between numerical models and experimental tests.

**3.1. Experimental Results.** The  $m-k$  experimental tests of LWC slabs showed similarities while the HN slabs presented different behaviour.

For composite slabs of LWC, the longitudinal sliding between the steel sheet and the concrete was lower than

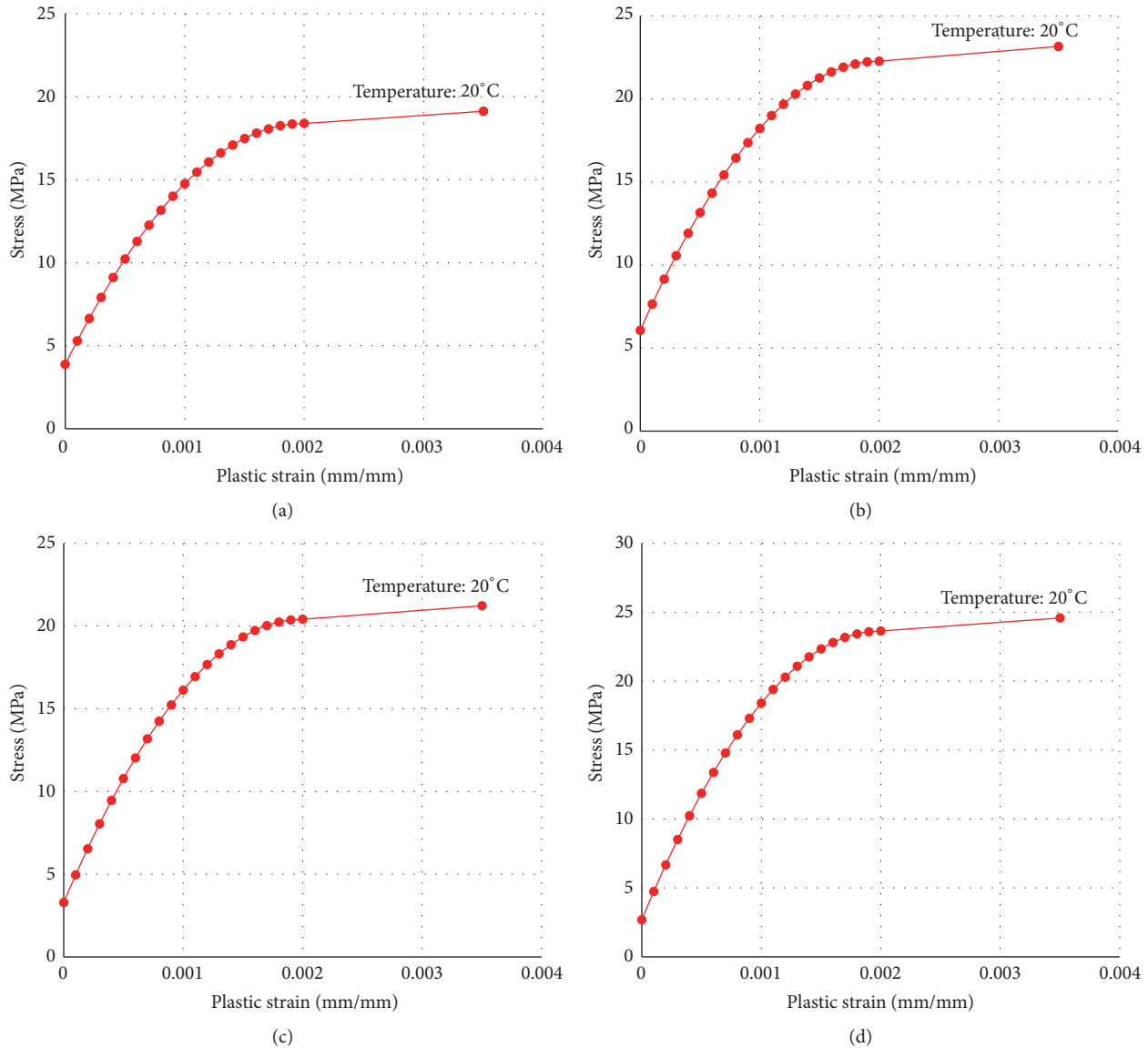


FIGURE 7: Multilinear isotropic hardening material laws introduced in the models: (a) LWC\_LSDur-23, (b) LWC\_LSDur-28, (c) LWC\_LSDur-37, and (d) normal concrete (HN).

0.1 mm when the failure load was reached. In this case, as indicated in the standard, the shear behaviour is considered brittle fracture. This involves that the shear strength is reduced by a coefficient of 0.8.

This brittle behaviour is often observed in  $m-k$  tests of normal concrete composite slabs when the cyclic load applied during the tests does not efficiently remove the chemical bond between steel and concrete. This was considered the cause for the test results of the LWC's composite slabs under study, which was later corroborated by the numerical analysis.

On the other hand, HN composite slabs showed different behaviour. In the case of HN, the measured longitudinal sliding was higher than 0.1 mm at the failure load, which is considered as ductile fracture.

The results obtained in  $m-k$  tests are gathered in Table 6.

The experimental tests results provide different  $m-k$  values for each composite slab. Results are fitted to determine a general equation for each composite slab type. Fitted representations are shown in Figure 8.

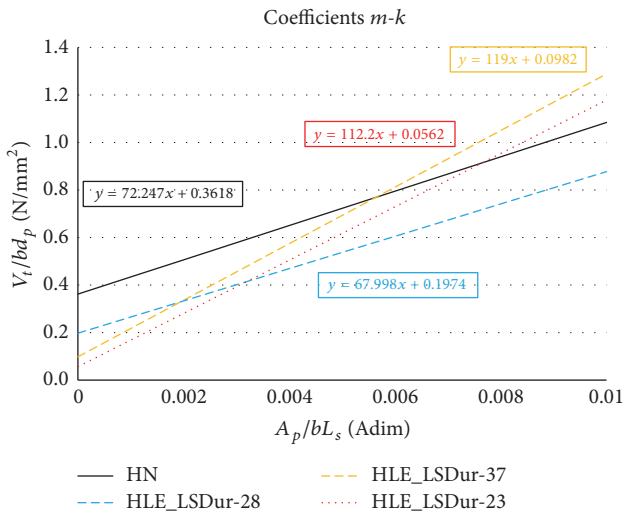
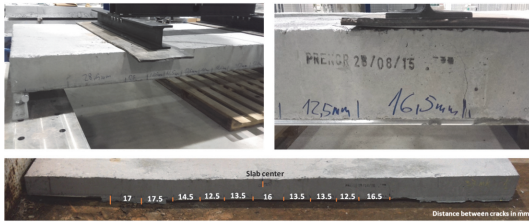
The mode of failure of the composite slabs was not a dominant and evident crack (see Figure 9). The majority of the composite slabs showed many small cracks. In the tests, it was considered that the slab failed when a significant increment in longitudinal sliding was measured.

The displacement between the steel sheet and concrete means that the failure of the composite slab is longitudinal shear stress. The length and the thickness of the slabs tested provided this failure mode.

In any case, the longitudinal sliding recorded at the end of the tests was very small for all composite slabs studied and not discernible to the naked eye.

TABLE 6:  $m$ - $k$  tests results.

Concrete type	Length (mm)	$L_s$ (mm)	$W_t$ (kN)	$V_{tck}$ (kN)	$A_p/b \cdot L_s$	$V_s/b \cdot d_p$ (N/mm <sup>2</sup> )	$m$ (N/mm <sup>2</sup> )	$k$ (N/mm <sup>2</sup> )
LWC_LSDur-23	2610	600	133	50.57	0.0024	0.322	112.2	0.0562
	2030	455	166	63.1	0.0031	0.402		
LWC_LSDur-28	2610	600	148	56.27	0.0024	0.359	68	0.1974
	2030	455	168	63.87	0.0031	0.407		
LWC_LSDur-37	2610	600	157	59.7	0.0024	0.380	119	0.0982
	2030	455	192	72.97	0.0031	0.465		
HN	2610	600	176	83.67	0.0024	0.533	72.25	0.3618
	2030	455	193	91.7	0.0031	0.585		

FIGURE 8:  $m$ - $k$  curve fitted for composite slabs tested.FIGURE 9: Composite slab LWC\_LSDur-37, 2610 mm long after  $m$ - $k$  test.

**3.2. Numerical Results.** In the numerical model, the vertical displacement applied provides a reaction force similar to the vertical load applied in the experimental test. The numerical model gives stress and deflection results under bending. Figure 10(a) shows the maximum reaction force obtained and Figure 10(b) represents the total deformations calculated.

As mentioned before, in the numerical models, the load (applied as a displacement) was increased gradually until it reached the maximum value observed in the  $m$ - $k$  tests.

In order to determine the quality of the numerical results, the values of deflection at the center of the slab obtained by FEA were compared to those measured during testing, for the different simulations carried out.

TABLE 7: Plasticity + chemical bond model. Comparison of errors (%) between numerical and experimental results at the shear-bond failure region.

Concrete type	Length (mm)	$f_{EXP}$ (mm)	$f_{NUM}$ (mm)	Error (%)
LWC_LSDur-23	2610	4.729	4.650	1.67
	2030	2.666	3.262	22.36
LWC_LSDur-28	2610	4.826	4.871	0.95
	2030	1.416	1.459	3.01
LWC_LSDur-37	2610	5.906	5.718	3.18
	2030	1.268	1.296	2.19
HN	2610	8.692	6.968	19.83
	2030	2.066	1.886	8.72

The results of the linear-elastic material models showed that it was necessary to take into account the plastic behaviour of the concrete to produce more accurate results.

Although the strain-hardening material models without chemical bond provided better results than the previous one, the values of longitudinal sliding between steel and concrete registered in the numerical models were superior to those measured during the tests.

These analysis reinforced the conclusions extracted from the tests regarding the inefficacy of the cyclic loading applied to remove the chemical bond.

Therefore, this chemical bond was finally included into the models, which produced the best correlation with the test results.

**3.3. Numerical and Experimental Comparison.** In this chapter, the percentages of error (%) between experimental and numerical analyses are compared.

Firstly, numerical and experimental results are compared with respect to the shear-bond failure region. Table 7 shows the comparison between experimental and numerical results of deflection  $f$  (mm) for the model including plastic behaviour for steel and concrete and the initial adhesion (chemical bond) between both materials.

Except for short span composite slabs made of LSDur-23, the numerical results show good agreement with the experimental results. In case of LSDur-23 slabs, the deviation of the results may be attributed to errors in the water or

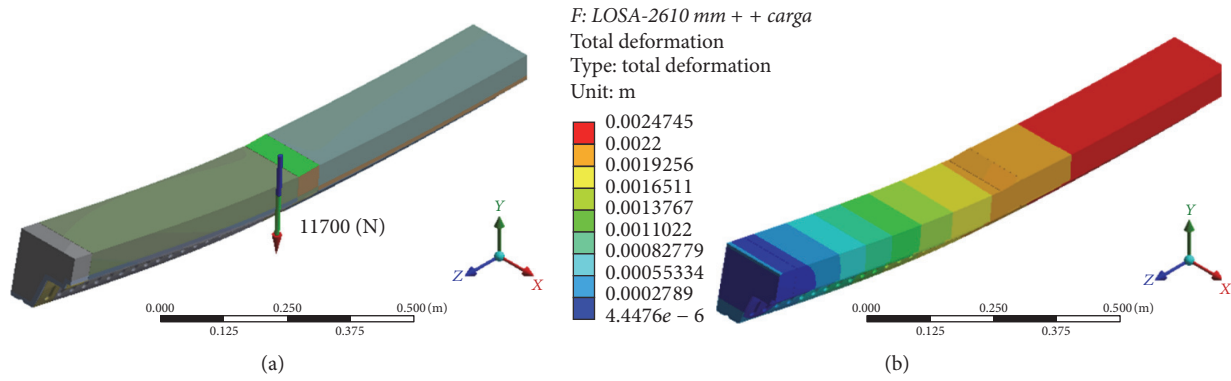


FIGURE 10: Numerical model results: (a) reaction force; (b) total deformation.

TABLE 8: Comparison of errors (%) of the different models at the shear-bond failure region.

Concrete type	Length (mm)	Linear-elastic model	Plasticity model	Plasticity + chemical bond model
LWC.LSDur-23	2610	16.28	1.18	1.67
	2030	0.40	23.27	22.36
LWC.LSDur-28	2610	4.89	10.68	0.95
	2030	8.51	9.69	3.01
LWC.LSDur-37	2610	34.19	4.08	3.18
	2030	8.92	1.00	2.19
HN	2610	62.22	19.25	19.83
	2030	45.84	12.66	8.72

TABLE 9: Comparison of errors (%) of the different models at the linear-elastic region.

Concrete type	Length (mm)	Linear-elastic model	Plasticity model	Plasticity + chemical bond model
LWC.LSDur-23	2610	13.54	1.61	1.97
	2030	9.54	15.87	14.81
LWC.LSDur-28	2610	6.12	11.99	4.21
	2030	12.86	11.90	5.65
LWC.LSDur-37	2610	19.47	0.62	3.46
	2030	3.88	6.87	7.23
HN	2610	42.30	9.48	3.57
	2030	38.31	21.34	9.40

aggregate dosage during the manufacturing of the composite slabs and/or on the displacement measurements taken during the tests.

The results of the linear-elastic model and the plasticity model without adhesion are not shown in detail here but summarized below. The comparison of results at the linear-elastic region for all models is also gathered in this section.

From the analysis of the results, it can be concluded that the introduction of the plastic behaviour of the materials is essential to adjust to reality.

In the comparison near the shear-bond failure area (see Table 8), the model including the chemical bond generally shows the best agreement (less than 3.2% error), except for short slabs dosing LSDur-23 and HN, where the errors obtained are close to 22%. This might suggest that although cyclic loading was applied to the slabs during the test to

remove the chemical bond between materials, this bond was not totally eliminated.

In the comparison of the elastic region (see Table 9), the errors in all plasticity models are acceptable, following a similar pattern to the previous comparison; that is, the results for short slabs of LSDur-23 and HN show the worst correlation, although in this case the model fit with chemical adhesion is much better (less than 10% error).

Finally, the results comparison for the longest span composite slabs (2610 mm) is shown graphically in Figure 11.

## 4. Conclusions

The main conclusions of this paper are explained in this chapter.

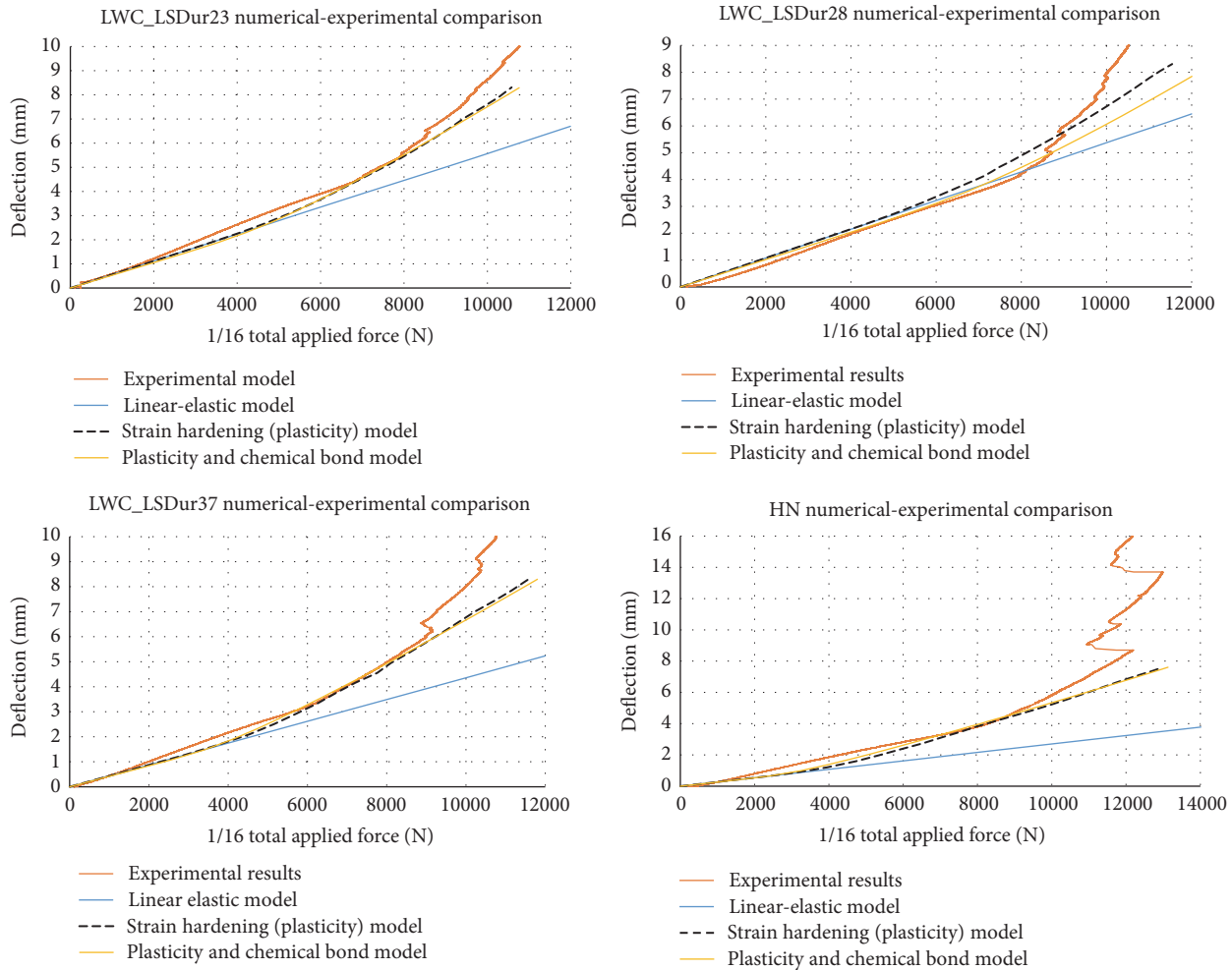


FIGURE 11: Comparison numerical-experimental results for 2610 mm composite slabs.

Based on the experimental tests, the structural resistance (failure load) of the composite slabs made of lightweight concrete reinforced with fibres is reduced between 11% and 25% with respect to conventional concrete, as shown by *m-k* testing. The main failure mode of composite slabs is longitudinal shear, for both LWC and HN slabs.

With respect to the numerical simulation, the numerical model simulates a 4-point bending test of composite slabs of different lengths according to Eurocode 4. These models were increased in complexity to reproduce the phenomena observed experimentally, introducing frictional contact, chemical adhesion, and plasticity material laws of steel and concrete.

The introduction of plasticity models for the materials is essential to achieve realistic results. In most cases, the plasticity models that include the chemical bond show better correlation with the experimental results. This corroborates the hypothesis that the chemical bond between steel and concrete was only partially removed by the cyclic load applied in the *m-k* tests.

Although the numerical models developed reproduce the behaviour of specific mixes of LWCs and normal concrete

(4 varieties of concrete, 3 LWCs and one HN), it could also be used for other dosages, provided that their mechanical properties are properly characterized.

Both experimental tests and numerical models show the same failure mode: longitudinal shear. It occurs when the shear strength of the mechanical interlock between concrete and steel is reached and therefore the two layers of the composite slab do not work as a single element.

Finally, it can be concluded that the experimental and numerical results are in good agreement. Moreover, the numerical models developed within this work can be used to improve and optimize the mechanical behaviour of composite slabs.

## Competing Interests

The authors declare that they have no competing interests.

## Acknowledgments

This work was partially financed by the Spanish Ministry of Science and Innovation cofinanced with FEDER funds under

Research Project BIA2012-31609. Furthermore, the authors are grateful for the regional funding through the Asturias Government and FICYT, also cofinanced with FEDER funds under Research Project FC-15-GRUPIN14- 004.

## References

- [1] B. S. Mohammed, M. A. Al-Ganad, and M. Abdullahi, “Analytical and experimental studies on composite slabs utilising palm oil clinker concrete,” *Construction and Building Materials*, vol. 25, no. 8, pp. 3550–3560, 2011.
- [2] J. J. Del Coz Díaz, P. J. García Nieto, J. L. Suárez Sierra, and I. Peñuelas Sánchez, “Non-linear thermal optimization and design improvement of a new internal light concrete multi-holed brick walls by FEM,” *Applied Thermal Engineering*, vol. 28, no. 8-9, pp. 1090–1100, 2008.
- [3] J. J. Del Coz Díaz, P. J. García Nieto, J. Domínguez Hernández, and A. Suárez Sánchez, “Thermal design optimization of lightweight concrete blocks for internal one-way spanning slabs floors by FEM,” *Energy and Buildings*, vol. 41, no. 12, pp. 1276–1287, 2009.
- [4] J. W. Rackham, G. H. Couchman, and S. J. Hicks, “Hicks composite slabs and beams using steel decking: best practice for design and construction,” MCRMA Technical Paper 13, Steel Construction Institute Publication P300, 2009.
- [5] UNE-EN 1994-1-1, EUROCODE 4: Desing of composite steel and concrete structures. Part 1-1: General rules and rules for buildings, 2013.
- [6] H. Cifuentes and F. Medina, “Experimental study on shear bond behavior of composite slabs according to Eurocode 4,” *Journal of Constructional Steel Research*, vol. 82, pp. 99–110, 2013.
- [7] T. Luu, E. Bortolotti, B. Parmentier, X. Kestemont, M. Briot, and J.-C. Grass, “Experimental investigation of lightweight composite deck slabs,” in *Proceedings of the 9th International Conference on Steel Concrete Composite and Hybrid Structures*, Leeds, UK, July 2009.
- [8] A. Penza, *Composite slabs with lightweight concrete: experimental evaluation of steel decking and lightweight concrete [Ph.D. thesis]*, Politecnico di Milano, 2010.
- [9] J. Guerrero Muñoz, *Analysis and optimization of thermal and structural behavior of composite slabs made of lightweight concrete [Ph.D. thesis]*, University of Oviedo, 2016.
- [10] S. Chandra and L. Berntsson, *Lightweight Aggregate Concrete*, Noyes Publications, 2002.
- [11] UNE, “Testing hardened concrete—part 3: compressive strength of test specimens,” UNE-EN 12390-3:2009, 2009.
- [12] UNE-EN 12390-13, Testing hardened concrete—Part 13: Determination of secant modulus of elasticity in compression, 2014.
- [13] ISO 6892-1, Metallic materials—Tensile testing—Part 1: Method of test at room temperature, 2009.
- [14] S. Moaveni, *Finite Element Analysis: Theory and Applications with ANSYS*, Prentice-Hall, New York, NY, USA, 2007.
- [15] EHE 2008 Structural Concrete Instruction, Annex 16, Recommendations for the use of Lightweight Concrete.
- [16] B. J. Daniels, “Shear bond pull-out tests for cold-formed-steel composite slabs,” Rapport d’Essais ICOM-194, EPFL, Lausanne, Switzerland, 1988.

## Research Article

# **In Situ Determination of the Transport Properties of Near-Surface Concrete Using AC Impedance Spectroscopy Techniques**

**Lipeng Wu, Peng Dai, and Yong Li**

*School of Civil Engineering, Shijiazhuang Tiedao University, Shijiazhuang 050043, China*

Correspondence should be addressed to Lipeng Wu; [lipengwu@outlook.com](mailto:lipengwu@outlook.com)

Received 11 July 2016; Accepted 31 October 2016

Academic Editor: Peng Zhang

Copyright © 2016 Lipeng Wu et al. This is an open access article distributed under the Creative Commons Attribution License, which permits unrestricted use, distribution, and reproduction in any medium, provided the original work is properly cited.

The durability of existing concrete structures has increasingly attracted widespread attention in recent years. The phenomenon of performance degradation is often associated with the intrusion of hazardous ions from outside. As the first barrier to external substances intrusion, the near-surface concrete plays an important role in durability. So the performance of in-service concrete structures often depends on the transport properties of the near-surface concrete. Accordingly, information on service conditions and life prediction can be obtained by testing these transport properties. In this paper, an *in situ* method for chloride ion diffusion coefficient determination is proposed based on the relationship between the alternating current impedance spectroscopy parameters and the chloride ion diffusion coefficient. By a rational design, the new method can synthetically reflect the transport properties of near-surface concrete and is not affected by the presence of the reinforcing bar. In addition, the experimental results show that the method is in good agreement with “PERMIT” migration test which has been widely used. The proposed method is less time consuming and nondestructive and has good reproducibility.

## **1. Introduction**

Durability of civil engineering structures has attracted worldwide attention. Concrete is predominantly used in construction within worldwide. In order to predict the service life of existing concrete structures, some important parameters such as chlorine ion diffusion coefficient must be obtained, especially for concrete structures exposed to deicing salt or marine environment. Laboratory test methods for permeability determination are generally suitable for a concrete block prepared in the laboratory. Drilled cores cannot reflect well the nature of in-service concrete structures because the field pouring, vibrating, and curing conditions of concrete are different from those of the laboratory; core samples drilled from structural members will bring damage resulting in microstructure change; and existing concrete structure always bear a certain load. Moreover, these methods aim to study the entire test block rather than the near-surface concrete. The near-surface concrete is the primary barrier to harmful substances, thereby determining the durability of

reinforced concrete structures to a certain extent. For these reasons, research and development of the chloride ion permeability test method applicable to *in situ* testing are particularly important. Researchers have proposed many field test methods. Some methods are for liquid intrusion [1–8], while some are for gas permeation [7–9] and electromigration [10, 11]. The gas permeation tests have high sealing requirements and are susceptible to concrete humidity. These methods also have poor discrimination ability for high-performance concrete. Liquid intrusion tests are simple to perform, and the required test equipment is also simple. However, their ability for high-performance concrete distinction is poor. These methods are apt to be influenced by temperature and humidity, which greatly reduce their applications. Chloride ion migration tests have reliable theory, but their testing process and data processing are complicated.

A testing method for chloride ion diffusion coefficient determination based on the alternating current (AC) impedance spectroscopy technique is established by Wu et al. by choosing an equivalent circuit model with a clear physical

meaning, using the Einstein–Smoluchowski equation, introducing a high concentration of chloride ion solution, and considering the correction of decreased impedance because of mineral admixture [12]. The AC impedance technique is applied to the field test in this paper through many considerations.

The *in situ* near-surface transport property measurement is quite different from that of the laboratory block test. First, the electrode arrangement is different. In the laboratory test, two stainless steel electrodes are attached to two opposite surfaces of the fully saturated specimen. However, one option for the *in situ* situation is the preembedding of an electrode in the concrete and attaching another electrode on the concrete surface. On the one hand, the diffusion coefficient equation of the laboratory test can be directly adopted. On the other hand, the measured point is fixed and the embedded electrode is susceptible to vibrating during concrete pouring, which results in errors that cannot easily be eliminated. The second method is arranging two electrodes on the concrete member surface, which will cause change of the conductivity cell constant. The influence of reinforcing bar on the impedance test is not clear. The advantage of this method is that the test location can be freely selected. The latter is used in this paper.

Using surface-contacted electrode arrangement will introduce several issues: how to determine the electrode shape and size, how to ensure close contact between the electrodes and the concrete surface, how to determine cell constant, and the influence of reinforcing bar on impedance testing. These problems will be solved individually.

## 2. Tester Design

The tester design, especially the electrode selection and arrangement, is the primary problem that must be considered for the field permeability test. Four points should be considered. First is the choice of electrode material. This test does not use the electrode/interface reversible electrochemical reaction. Hence, the electrode can be inert, and an economical stainless steel electrode can be used. Second is the electrode shape and size. Using symmetric electrodes can produce a symmetric charge transfer pathway, which is easy to calculate. Therefore, a circular electrode is used as the inner electrode and an annular electrode is utilized as the outer. The diameter of the inner and outer electrodes should be able to cover one to two times the area of the coarse aggregate. The specific size can also be further determined. Third is that the valid test depth should be roughly equal to the concrete cover. The effective test depth is small if the distance between the inner and outside electrodes is small. The effective test depth will also increase if the distance is increased. The electrode size and arrangement can be mathematically determined if a particular test depth is specified. Fourth is the contact between the electrode and the measured surface. A thin layer of the electrolyte solution with good conductivity can be introduced to ensure a close contact between the two.

The preliminary tester design is presented in Figure 1 by the preceding considerations.

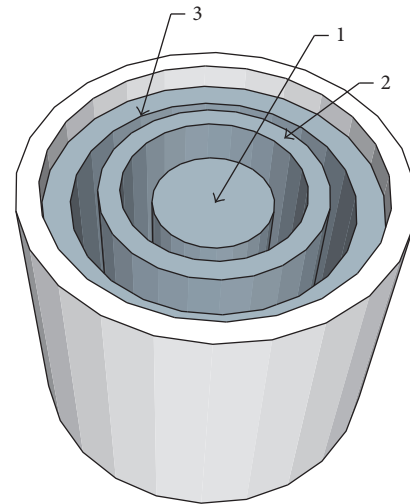


FIGURE 1: Schematic diagram of the tester.

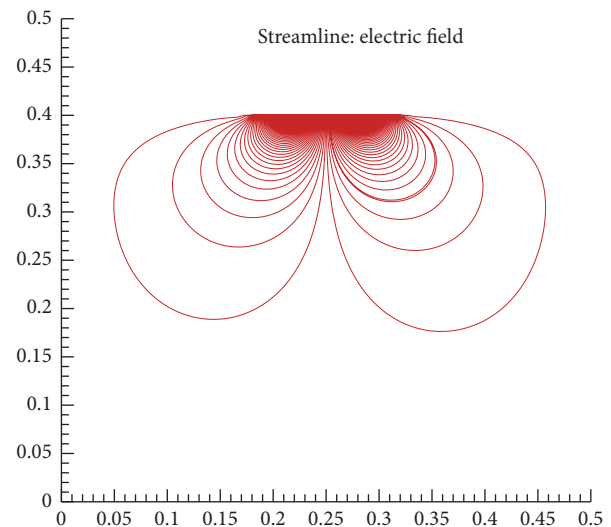


FIGURE 2: Electric field intensity distribution of the near-surface concrete.

The tester chamber is made of polymethyl methacrylate. In the center of the tester is a column (marked as 1) on which the inner circular electrode is fixed. A hollow cylinder marked as 2 serves as an isolator forming an inner chamber and an outer chamber. A hollow cylinder marked as 3 is used to fix the outer annular electrode. An annular notch is located on hollow cylinder 2 to mount a rubber ring for the complete separation of the inner and outer chambers. The outermost annular ring 4 is used to fix the tester onto the concrete surface. The two electrodes are connected to the impedance analyzer by wires. The highly conductive electrolyte solution (1 mol/L NaCl) is injected into the inner and outer chambers after the tester is mounted.

The electrode size and arrangement are calculated using the electric field finite element analysis (Figure 2). The finite element model is axisymmetric. The size of the internal and the external electrodes and their spacing are the same as

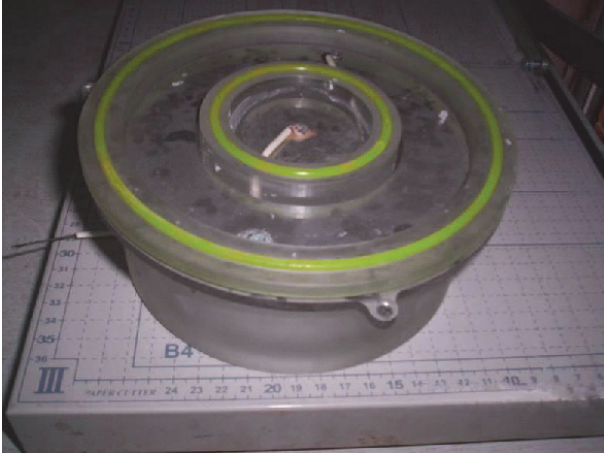


FIGURE 3: Prototype of the AC impedance field testing.

those of the prototype (see Figure 3). The potential difference between the two electrodes is 10 mV, and the relative permittivity is 4.2. The length of the solution domain is 0.5 m and the width is 0.4 m. The element is square, with side length of 0.005 m.

The effective test depth should be approximately equal to 30 mm, which is the typical thickness of the concrete cover. Accordingly, the finite element simulation shows that the diameter of the inner circular electrode can be 50 mm; the internal diameter of the outer electrode is 88 mm; and the external diameter is 142 mm. These values allow the near-surface electric flux to account for more than 90% of the total electric flux. The manufactured tester based on the results of the finite element simulation is presented in Figure 3.

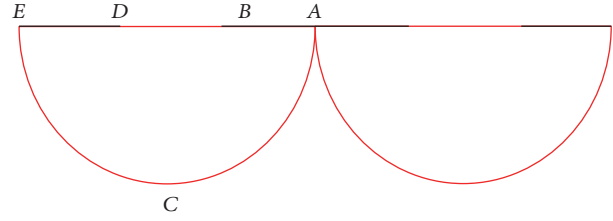
Many holes are drilled in the concrete before the test to fix the tester using bolts and nuts. Subsequently, 1 mol/L NaCl solution similar to that used in the theoretical part of this paper is utilized to conduct vacuum salt saturating. The tester is fixed together, and the highly conductive electrolyte solution is injected into the chambers. The AC impedance test is then performed.

### 3. Cell Constant Determination

The theoretically deduced chloride ion diffusion coefficient is calculated as follows [12]:

$$D_{Cl^-} = \frac{aRT}{1.64F^2 R_{cp} C_{Cl^-}}, \quad (1)$$

where  $R$  is the universal gas constant ( $=8.314 \text{ J K}^{-1} \text{ mol}^{-1}$ );  $T$  is the absolute temperature (K);  $F$  is the Faraday constant ( $=96485 \text{ C mol}^{-1}$ );  $R_{cp}$  is the resistance of the connected capillary pores or connected microcracks in concrete (Ohm); and  $C_{Cl^-}$  is the concentration of chloride ( $\text{mol L}^{-1}$ ). The cell constant ( $a$ ) is the ratio of the length of the current conduction pathway to its cross-sectional area. The cell constant is the ratio of the thickness of the test block to the specimen/electrode contact area when two identical electrodes attached to two opposite surfaces of the specimen are used.



$$A(0, 0) \quad B(-25, 0) \quad C(-35.5, -30) \\ D(-44, 0) \quad E(-71, 0)$$

FIGURE 4: Assumption for the electric field lines.

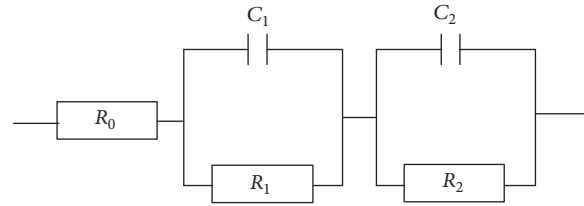


FIGURE 5: Equivalent circuit of the field test.

The current conduction pathway in the field test conditions is curved. The two contact areas of the specimen/electrodes are not equal (Figure 3). Therefore, the cell constant of the field testing needs to be further determined.

The following assumptions are made for simplicity: (1) the current conduction pathway of the concrete surface is a straight line with a length equal to the net distance of the electrodes; (2) the current conduction pathway of the outermost effective measurement range is a circular arc, and the lowest point is the effective test depth; and (3) the length of the current conduction pathway is the average length of the inner and outer conduction pathways, and the cross-sectional area of the current conduction pathway is the average area of the two electrodes (Figure 4).

The length of the outermost arc can be calculated according to the  $A$ ,  $C$ , and  $E$  coordinates. The cell constant,  $a$ , is finally determined as  $9.2 \text{ m}^{-1}$ .

### 4. Determination of Equivalent Circuit for Field Test

A highly conductive electrolyte solution is introduced to reduce the impedance between the concrete surface and the electrodes. Therefore, the equivalent circuit for the field test (Figure 5) is different from that of [12].

The two left units of the equivalent circuit in Figure 5 are similar to those used in [12]. The right unit of the circuit in the same figure comprises a resistor-capacitor in parallel representing the resistance and the interfacial capacitance caused by the introduction of the electrolyte solution. The resistance of the 1 mol/L NaCl solution layer ( $R_2 = \rho L' / A'$ , where  $L'$  is the distance between the concrete surface and the electrode and  $A'$  is the electrode area) is actually much smaller than the resistance of the capillary pore solution in

TABLE I: Concrete mix.

Specimen number	Materials used (unit: kg/m <sup>3</sup> )						
	Cement	Fly ash	Slag	Silicon fume	Water	Fine aggr.	Coarse aggr.
C0	466.0	0	0	0	186.0	750.0	1125.0
FA1	372.8	92.3	0	0	186.0	735.7	1103.6
FA2	276.6	186.4	0	0	186.0	720.5	1080.9
FA3	186.4	276.6	0	0	186.0	705.3	1058.0
GS1	349.5	0	116.5	0	186.0	747.6	1121.4
GS2	233.0	0	233.0	0	186.0	744.2	1116.3
GS3	116.5	0	349.5	0	186.0	740.8	1111.2
SF1	442.7	0	0	23.3	186.0	747.6	1121.4
SF2	419.4	0	0	46.6	186.0	744.2	1116.3
SF3	396.1	0	0	69.9	186.0	740.8	1111.2

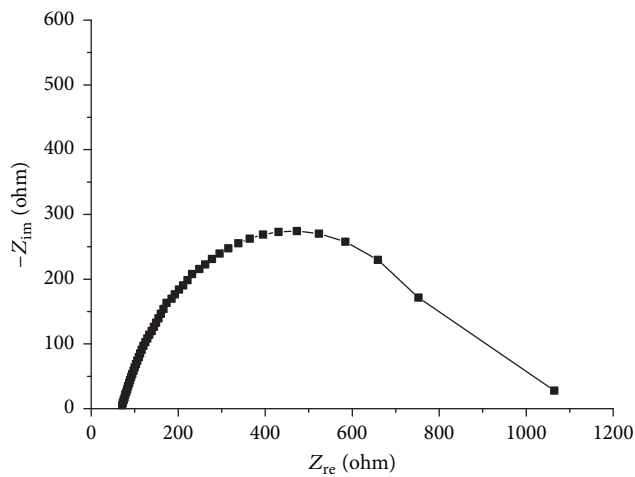


FIGURE 6: Nyquist plot of a typical field AC impedance measurement.

concrete. Accordingly, the right semicircular generated by  $R_2$  and  $C_2$  in parallel is much smaller than that of  $R_1$  and  $C_1$  in parallel. Therefore, the right arc is not visible. The Nyquist plot of the measured impedance data (Figure 6) does not exhibit two semicircular arcs, which can also prove this point.

## 5. Factors Affecting Field Test

The two main factors affecting the *in situ* determination of the transport properties using the AC impedance technique are water/salt saturating level and the presence of the reinforcing bar. The current carriers in the impedance testing are dissolved ions. A significant increase in the measured impedance, which does not reflect the true permeability-related parameters, is obvious if the saturating level is low. Exploratory tests show that the measured impedance difference could be several hundreds or even thousands of times for the same concrete specimens with different saturating levels. Therefore, the in-field test water/salt saturating level must be guaranteed before the testing.

Commercially available water saturating equipment can be used for laboratory testing. However, related equipment

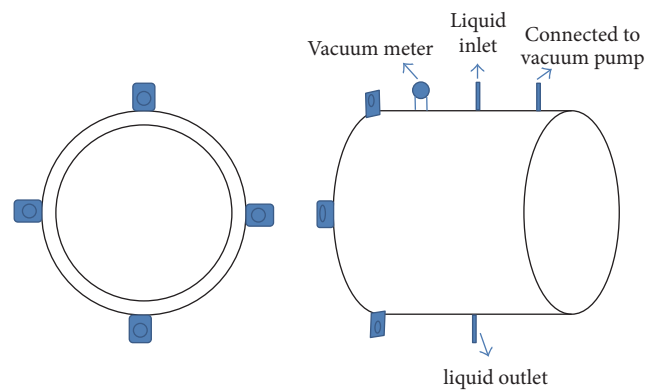


FIGURE 7: Design of the field test saturating equipment.

for the field testing is not yet available. Hence, a prototype is designed (Figure 7).

First, lower the pressure inside the container from normal atmospheric pressure to 0.1 atm or less, then inject saturated calcium hydroxide solution into the container, and continue to maintain the vacuum degree. The saturation process may take up to 6 hours, depending on the density of the cover concrete. Also an alternative approach is recommended. Attach a piece of sponge to the concrete surface and spray calcium hydroxide solution to the sponge and ensure that the sponge is saturated. In general, it may take three days for the concrete surface to be saturated using this method.

The presence of the reinforcing bar as a conductor may comprise part of the current conduction pathway, which will affect the impedance measurement for the near-surface concrete. An experimental study and a theoretical analysis of the influence of the reinforcing bar on the AC impedance test will be presented in this section.

The specimens ( $\Phi 300 \text{ mm} \cdot 120 \text{ mm}$ ) are prepared using the concrete mix mentioned in Table I.

The concrete cover thickness for the reinforced concrete specimen is 30 mm. All the specimens are subsequently immersed in a saturated solution of calcium hydroxide after mold removal. The typical plain and reinforced concrete specimens are illustrated in Figure 8.



(a) Plain concrete blocks



(b) Reinforced concrete blocks

FIGURE 8: Concrete blocks.



FIGURE 9: AC impedance test.

Salt saturating is first performed using the 1 mol/L NaCl solution. The 1 mol/L NaCl solution is injected to reduce the interfacial effect after the tester is fixed onto the concrete surface. An Agilent 4294A precision impedance tester is used to perform the test. The frequency range of the impedance test is 40 Hz–40 MHz, while the amplitude of the applied AC is 0.5 V. Five points (logarithmic spacing) are collected for each order of magnitude. An image of the testing is presented in Figure 9.

The typical Nyquist plots of the impedance test of the plain and reinforced concrete blocks with the similar mix design are illustrated in Figure 10.

The presence of the reinforcement bars has little effect on the AC impedance testing compared with the impedance test result of the plain concrete specimen (Figure 10). The reason lies in the designed tester. The effective test depth is 30 mm. In other words, the location of the reinforcing bar is beyond the designed test depth. The finite element simulation shows that the electric field intensity decreases with the increasing depth. The near-surface part of the concrete decides the impedance

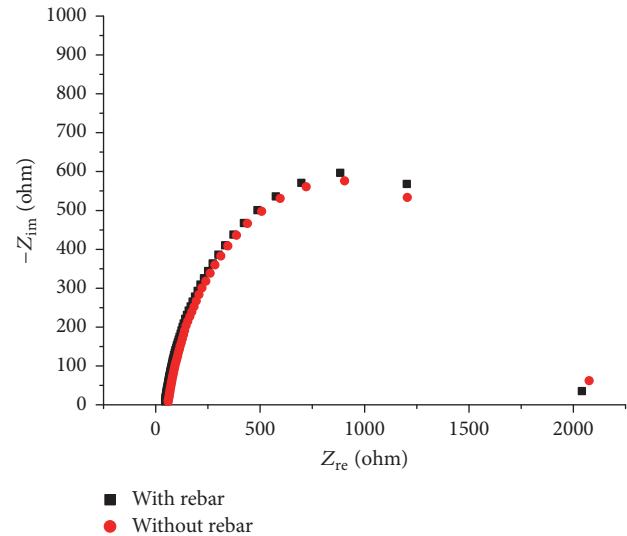


FIGURE 10: Influence of the reinforcing bar on AC impedance testing.

to a great extent. Therefore, the field impedance test is not subject to the influence of the reinforcement presence after a careful design.

## 6. Experimental Study of the Concrete with Different Cementitious Materials

Table 1 shows the concrete mix used in this research. The shape, size, and curing condition of the prepared specimens and the test parameters used are all similar to those in Section 5. The testing age is 28 d and 90 d.

The typical impedance data obtained are presented in Figures 11 and 12.

The chloride ion diffusion coefficient can be obtained using (1) by numerical fitting between the measured impedance data and the selected equivalent circuit and using the approximate *in situ* cell constant (i.e.,  $a = 9.2 \text{ m}^{-1}$ ) after

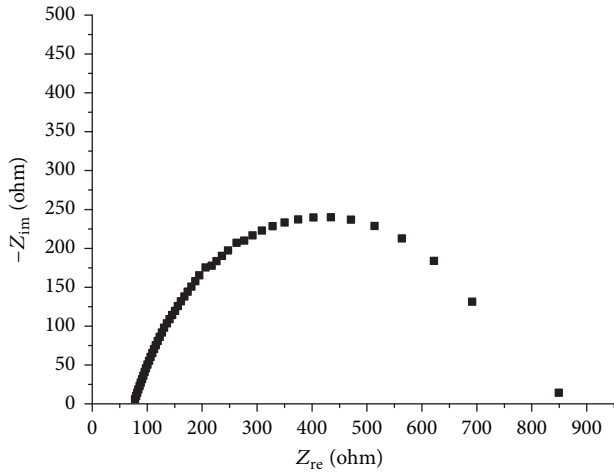


FIGURE 11: Nyquist plot of specimen number SF3 (28 d).

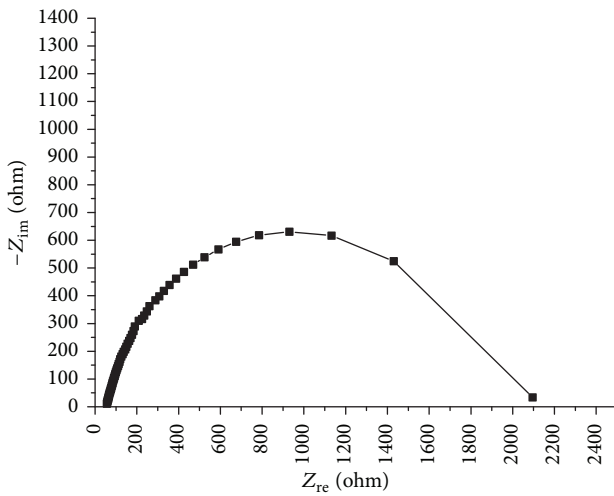


FIGURE 12: Nyquist plot of specimen number SF3 (90 d).

data validation checking. The diffusion coefficient can then be further corrected according to the type of cementitious materials (see [12]). The chloride ion diffusion coefficients for the concrete with different cementitious materials are presented in Table 2.

## 7. Analysis and Discussion

The proposed *in situ* method for the chloride ion diffusion coefficient determination can discriminate concretes with different cementitious materials (Table 2). The concretes with mineral admixtures will effectively reduce the diffusion coefficient at a long age. As regards the concrete with fly ash, especially on the high replacement level, the anti-intrusion ability will decrease at an early age (i.e., less than 90 d) probably because of the lower fly ash activity. Experimental studies have shown that the reaction degree is very low before 28 d [13]. Moreover, the fly ash reactivity is only able to increase significantly after 90 d. By contrast, the silica fume has a much higher reactivity. The particles of the silica fume

TABLE 2: Test results of the chloride ion diffusion coefficients.

Specimen	Chloride ion diffusion coefficients	
	$D$ (28 d) <sup>a</sup> ( $\times 10^{-12} \text{ m}^2 \text{ s}^{-1}$ )	$D$ (90 d) ( $\times 10^{-12} \text{ m}^2 \text{ s}^{-1}$ )
C0	3.60 (3.71)	1.40
FA1	5.82 (5.90)	1.10
FA2	2.70 (2.82)	1.21
FA3	4.73 (4.88)	1.63
GS1	2.85 (2.96)	1.35
GS2	2.15 (2.32)	1.20
GS3	1.42 (1.60)	1.03
SF1	1.20 (1.31)	0.41
SF2	0.83 (0.87)	0.34
SF3	1.03 (1.12)	0.36

<sup>a</sup>Data in () are obtained from the PERMIT ion migration test; see Section 7 for details.



FIGURE 13: "PERMIT" ion migration test.

are also much smaller than those of the cement particles. Therefore, the pores in the concrete can be effectively filled, which results in a decrease of the interconnected porosity that consequently reduces permeability. However, the chloride ion diffusion coefficient for the high replacement level (i.e., 15%) increases maybe because of the mixture becoming too viscous to compact, which causes the porosity to increase. Compared with the fly ash and the silica fume, slag has an in-between activity. Microscopic observation and mercury injection tests show that the reaction degree of the slag obviously increases with the increasing age, which decreases the permeability [14]. Therefore, the test result of this study reflects the well-recognized understanding.

Besides, the proposed test method was validated in the lab by carrying out a comparative investigation and correlating the results with the migration coefficient from the "PERMIT" test [10, 11]; the procedure to carry out the PERMIT ion migration test can be found in [10]. The concrete mixes are the same as that of Table 1. The test specimen is 600 mm \* 300 mm \* 150 mm; see Figure 13 for details.

The results in Table 2 also indicate that the proposed method correlates well with the "PERMIT" ion migration test, which has gradually gained recognition worldwide.

Compared with the water and gas permeability tests, the proposed field test method requires full water/salt saturating, which makes it less affected by the moisture in the concrete. The impedance method greatly reduces the testing time compared with the “PERMIT” ion migration method. The measuring time is less than 5 min after the preparatory work is done. However, the concrete must be fully saturated with sodium chloride solution; otherwise, the obtained results are unreliable.

## 8. Conclusions

The AC impedance spectroscopy technology is less time consuming. The concrete mesostructure can be well revealed through numerical fitting between the preset equivalent circuit and the measured impedance data. The AC impedance technique-based method is applied to the field test using the carefully designed tester.

The proposed method is not subject to the influence of the presence of the reinforcement because the electrode shape, size, and arrangement are considered. The cell constant is approximately calculated based on the finite element analysis of the electric field and through many assumptions.

A highly conductive electrolyte solution fills the space between the electrodes and the concrete surface to guarantee the validity of the test data, ensure good repeatability, and minimize the interface effect. The additional resistance and capacitance caused by introducing the electrolyte solution can be ignored in the Nyquist plot.

The most important factor affecting the measuring accuracy is the saturating degree after the influence of the reinforcing bar is eliminated. The near-surface concrete must be fully saturated before the tests to restrain the unpredictable error effectively.

The proposed method has good theoretical basis and can effectively distinguish the antipenetration ability of different concretes.

## Competing Interests

The authors declare that there is no conflict of interests regarding the publication of this paper.

## Acknowledgments

The authors acknowledge the support from National Natural Science Foundation of China (Grant no. 51408379) and Natural Science Foundation of Hebei, China (Grant no. E2013210125).

## References

- [1] R. Siddique, “Compressive strength, water absorption, sorptivity, abrasion resistance and permeability of self-compacting concrete containing coal bottom ash,” *Construction and Building Materials*, vol. 47, pp. 1444–1450, 2013.
- [2] M. V. Diamanti, A. Brenna, F. Bolzoni, M. Berra, T. Pastore, and M. Ormellese, “Effect of polymer modified cementitious coatings on water and chloride permeability in concrete,” *Construction and Building Materials*, vol. 49, pp. 720–728, 2013.
- [3] N. Chahal, R. Siddique, and A. Rajor, “Influence of bacteria on the compressive strength, water absorption and rapid chloride permeability of fly ash concrete,” *Construction and Building Materials*, vol. 28, no. 1, pp. 351–356, 2012.
- [4] J. Bolouri Bazaz and M. Khayati, “Properties and performance of concrete made with recycled low-quality crushed brick,” *Journal of Materials in Civil Engineering*, vol. 24, no. 4, pp. 330–338, 2012.
- [5] F. Pacheco-Torgal and S. Jalali, “Compressive strength and durability properties of ceramic wastes based concrete,” *Materials and Structures/Materiaux et Constructions*, vol. 44, no. 1, pp. 155–167, 2011.
- [6] L. Basheer, J. Kropp, and D. J. Cleland, “Assessment of the durability of concrete from its permeation properties: a review,” *Construction and Building Materials*, vol. 15, no. 2-3, pp. 93–103, 2001.
- [7] J. W. Figg, “Methods of measuring the air and water permeability of concrete,” *Magazine of Concrete Research*, vol. 25, no. 85, pp. 213–219, 1973.
- [8] N. Hearn and R. H. Mills, “A simple permeameter for water or gas flow,” *Cement and Concrete Research*, vol. 21, no. 2-3, pp. 257–261, 1991.
- [9] M. Carcassès, A. Abbas, J.-P. Ollivier, and J. Verdier, “An optimised preconditioning procedure for gas permeability measurement,” *Materials and Structures*, vol. 34, no. 245, pp. 22–27, 2002.
- [10] P. A. M. Basheer, R. J. Andrews, D. J. Robinson, and A. E. Long, ““PERMIT” ion migration test for measuring the chloride ion transport of concrete on site,” *NDT and E International*, vol. 38, no. 3, pp. 219–229, 2005.
- [11] S. Nanukuttan, *Development of a New Test Protocol for the Permit Ion Migration Test*, Queen’s University of Belfast, Belfast, UK, 2007.
- [12] L. Wu, P. Dai, and Y. Li, “Determination of the transport properties of structural concrete using AC impedance spectroscopy techniques,” *Journal of Engineering*, vol. 2016, Article ID 2630186, 8 pages, 2016.
- [13] T. G. Ushaa, R. Anuradha, and G. S. Venkatasubramani, “Performance of self-compacting geopolymer concrete containing different mineral admixtures,” *Indian Journal of Engineering and Materials Sciences*, vol. 22, no. 4, pp. 473–481, 2015.
- [14] H. Jin, J. Guohua, W. Qiang, Z. Haibing, and T. Aimin, “Influence of early-age moist curing time on the Late-Age properties of concretes with different binders,” *Indian Journal of Engineering and Materials Sciences*, vol. 21, no. 6, pp. 677–682, 2014.

## Research Article

# The Hysteresis Performance and Restoring Force Model for Corroded Reinforced Concrete Frame Columns

Guifeng Zhao,<sup>1</sup> Meng Zhang,<sup>1</sup> Yaoliang Li,<sup>1</sup> and Dawang Li<sup>2</sup>

<sup>1</sup>School of Civil Engineering, Zhengzhou University, Zhengzhou 450001, China

<sup>2</sup>Guangdong Provincial Key Laboratory of Durability for Marine Civil Engineering, Shenzhen University, Shenzhen 518060, China

Correspondence should be addressed to Dawang Li; lidw@szu.edu.cn

Received 14 August 2016; Accepted 5 October 2016

Academic Editor: Song Han

Copyright © 2016 Guifeng Zhao et al. This is an open access article distributed under the Creative Commons Attribution License, which permits unrestricted use, distribution, and reproduction in any medium, provided the original work is properly cited.

A numerical simulation of the hysteresis performance of corroded reinforced concrete (RC) frame columns was conducted. Moreover, the results obtained were compared with experimental data. On this basis, a degenerated three-linearity (D-TRI) restoring force model was established which could reflect the hysteresis performance of corroded RC frame columns through theoretical analysis and data fitting. Results indicated that the hysteretic bearing capacity of frame columns decreased significantly due to corrosion of the rebar. In view of the characteristics of the hysteresis curve, the plumpness of the hysteresis loop for frame columns decreased and shrinkage increased with increasing rebar corrosion. All these illustrated that the seismic energy dissipation performance of frame columns reduced but their brittleness increased. As for the features of the skeleton curve, the trends for corroded and noncorroded members were basically consistent and roughly corresponded to the features of a trilinear equivalent model. Thereby, the existing Clough hysteresis rule can be used to establish the restoring force model applicable to corroded RC frame columns based on that of the noncorroded RC members. The calculated skeleton curve and hysteresis curve of corroded RC frame columns using the D-TRI model are closer to the experimental results.

## 1. Introduction

The RC frame column is currently one of the most widely used structural forms. With the increase in its service life and the direct or indirect effects of external corrosion media, structural materials will degrade and undergo surface cracking, carbonisation, desquamation, corrosion-induced expansion of the rebar, and so forth, as shown in Figure 1. Of these, rebar corrosion is regarded as the prime factor affecting the changes in the durability of concrete structures [1, 2]. Corrosion leads to the degradation of geometric parameters and mechanical properties of rebar and, to some extent, will weaken the static bearing capacity of a structure and increase its brittleness. Meanwhile, the seismic performance will be inevitably impaired [3–5].

A frame column, which supports structures such as beams and slabs, is considered the foremost load-bearing member in an RC framed structure. Once a frame column is broken, it exerts a more severe influence on the damage suffered by beams, slabs, and filler walls. As for the frame

structures constructed in areas where earthquake frequently occurs, the frame column bears not only the vertical load, but also the brunt of any seismic action. The frame column, as a kind of eccentric compression member, has a lower stiffness than that of the beam and bears mainly vertical load. Therefore, even if only a small number of columns are damaged in a frame structure, the whole structure is likely to collapse (Figure 2). Considering the aforementioned reasons, engineers in different countries try to improve the bearing capacity, ductility, and resistance to lateral displacement, of frame columns as much as possible, so as to endow the frame structure with reliable seismic behaviour.

The hysteresis curve and restoring force model are two important indicators used when analysing the seismic behaviour of RC frame columns [8, 9]. When giving the expectation of ground motion in a mathematical model or inputting certain seismic waves for the region where a structure is located, a restoring force model and its parameters are the most important factors influencing the results of the seismic response analysis of the structure. The hysteresis

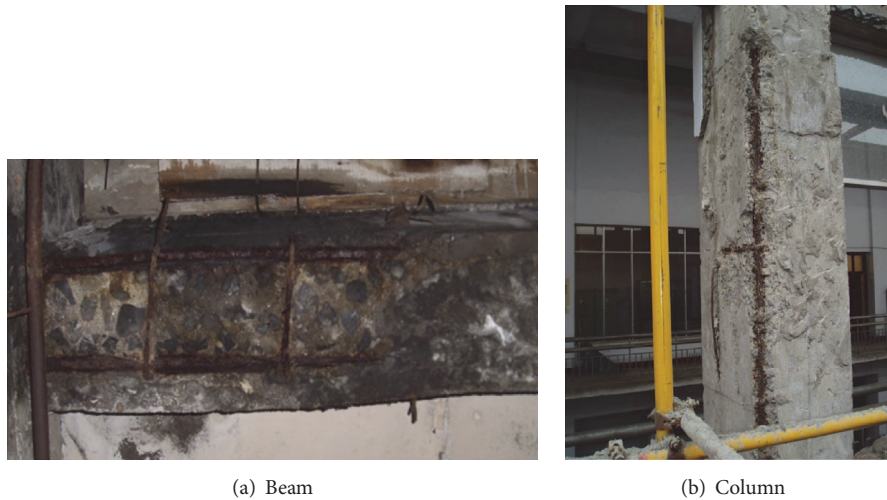


FIGURE 1: Cracks, desquamation of concrete cover, and corrosion of rebar in the frame beam and column.



FIGURE 2: Earthquake damage to the bottom columns in a frame structure.

performance and restoring force model are mainly influenced by factors such as the size of the members, reinforcement ratio, loading system, and material properties [10–12].

The hysteresis curve reflects the characteristics of structures or members during repetitive stress, including deformation, stiffness degradation, and energy consumption [14–16]. The restoring force model of members refers to the capacity of members to restore themselves to their original column form after unloading and shows the mathematical relationship between restoring force and deformation under cyclic loading [14]. Broadly speaking, the restoring force model consists of a skeleton curve and a hysteresis rule. The former draws boundaries for all the hysteresis feature points while the latter reflects the highly nonlinear characteristic of the structure. The restoring force model also represents the seismic behaviour of structures or members in the analysis of the elastoplastic seismic response and can be obtained based on the relationship between the restoring force and deformation through repetitive experiments. In actual application, the relationship curve needs to be abstracted and simplified to form a practical mathematical model.

So far, existing research on the seismic behaviour of engineering structures is mainly conducted on those to be built, while ignoring the relationship between the seismic

behaviour and service time of the structure. As a matter of fact, with the extension of the service of RC frame structures, the corrosion and degradation accumulate continuously. Under such circumstances, the original seismic design of structures fails to reflect the seismic safety situation of corroded structures which have been used for a certain time. Therefore, the seismic safety and durability of corroded and degraded RC frame structures need to be reevaluated and tested, so as to clarify the current performance of such structures. Based on the evaluated results, different measures can be applied to reinforce the structures according to the importance of, and extent of the damage to, the structures. After reinforcement, structures are expected to resist possible seismic actions and avoid, or reduce, casualties and economic loss throughout their service lives.

At present, the hysteresis performance and restoring force models for noncorroded RC frame structures or members have been explored widely in engineering. However, there are relatively few research reports on degraded RC structures or members (particularly frame columns) affected by corrosion. Existing studies mainly focus on the evaluation of the macroscopic seismic behaviour and reinforcement effect of reinforced corroded columns [17–19]. In addition, the hysteresis performance of corroded frame columns is generally studied on samples of a few experiments [13, 19, 20]. Considering that the corrosion and degradation of RC members take a long time in most natural environments, conducting simulations in natural conditions takes a long time and costs too much. Therefore, accelerated corrosion tests are commonly used in practice. By changing parameters including the concentration, chemical components, temperature, and flow rate of the corrosive media, the corrosion effect is enhanced and therefore accelerates testing. Obviously, this approach provides favourable support to research into the stress-related properties of corroded RC structures. To obtain an accurate hysteresis curve and a restoring force model for a corroded RC frame column with specific design parameters, a large number of samples need to be prepared

while using an accelerated corrosion test, to acquire sufficient experimental data. While performing this kind of experiment, the preparation of samples takes a long time and is expensive, and few parameters can be considered at any time. Due to these limitations, the hysteresis performance and restoring force model of corroded RC members have not been sufficiently investigated. Owing to the absence of simple, feasible, calculation methods for the restoring force model of a corroded RC member, the analysis and evaluation of the seismic safety of large amounts of corroded RC structures in seismic zones cannot be rapidly performed to obtain accurate results. This influences the formulation and implementation of maintenance and reinforcement decisions. Therefore, the investigation of the hysteresis performance and a restoring force model for corroded RC structures or members is deemed important for the analysis and assessment of seismic reliability and the maintenance and reinforcement of structures [3–5, 21].

With the rapid development of nonlinear finite element techniques and computer technology, numerical simulation has been widely applied in civil engineering. Moreover, numerical simulation presents numerous advantages such as short computation time and low cost, and it considers the influences of various parameters. Thereby, numerical simulation is used based on the experimental research to study the hysteresis performance of corroded RC members under different working conditions and obtain sufficient relationship data between the restoring force and deformation. In this way, a simple, practical, mathematical model can be established: this is an easy way to construct the restoring force model of corroded members.

According to the above analysis, an RC frame column was studied in terms of the influences of different corrosion rates on the hysteresis performance of the column using nonlinear FE software ABAQUS. Thereafter, the simulation results were compared with the experimental results to verify the reliability of the FE numerical simulation [13]. On this basis, various corroded members were studied by changing the parameters used in their analysis. Furthermore, by analysing the obtained hysteresis, skeleton, and curves, a restoring force model of corroded RC frame column was constructed. The model was expected to provide a simple, reliable computational basis for seismic safety analysis, reliability assessment, reinforcement, and reconstruction of corroded RC frame structures.

## 2. Definition of a Constitutive Model for RC Materials in ABAQUS

**2.1. Constitutive Model for Concrete.** A concrete damaged plasticity (CDP) model is a native constitutive model for concrete materials implicit to the algorithm used in the ABAQUS software. The model was first proposed by Lubliner et al. [22] and improved by Lee and Fenves [23] to apply to nonlinear analysis of concrete structures and members under monotonic and cyclic loading [24, 25]. Owing to the concrete materials being affected by various environmental media in different ways, including weakening effects, such as corrosion and carbonisation by chloride ions and sulphates, and strengthening effects, for example, the action of nitrates,

TABLE 1: Empirical values of parameters in the CDP model.

Parameter	$\Psi$	$m$	$\alpha_f$	$\gamma$	$\mu$
Value	30	0.1	1.16	0.6667	0.0005

it is difficult to define the effects by any uniform standard [26]. The most common causes of weakening chloride- and sulphate-induced corrosion of concrete were taken as examples in this research [27]. Corrosion only affects the concrete in its protective layer, while it has little influence on the internal core concrete under less serious corrosion. Thereby, the authors suggested determining expressions for the stress-strain relationship of intact concrete cores based on the constitutive relationship recommended by Chinese Standard GB50010-2010, Code for the Design of Concrete Structures [28], and the corroded concrete in the protective layer was only regarded as the bearing capacity reserves of the material, while ignoring its contribution to the strength. The bearing capacity reserve was achieved by setting birth and death elements in ABAQUS.

Concrete structures, or members, will produce plastic deformation and cracking under low intensity cyclic loading, and both the accumulation of plastic deformation and the expansion of cracks can induce stiffness degradation or softening. So, a damage factor  $d$  [29] was used in ABAQUS to describe this stiffness degradation or softening:

$$d = 1 - \frac{\sigma_{\text{true}}/E_0}{\varepsilon^{\text{pl}}(1/b_c - 1) + \sigma_{\text{true}}/E_0}, \quad \varepsilon^{\text{pl}} = \varepsilon^{\text{in}} \times b_c, \quad (1)$$

where  $d$  is the damage factor;  $\sigma_{\text{true}}$  is the true stress;  $E_0$  is the initial elastic modulus of the concrete;  $\varepsilon^{\text{in}}$  is the inelastic strain in the concrete;  $\varepsilon^{\text{pl}}$  is the plastic strain in the concrete;  $b_c$  is the scale factor between plastic strain and inelastic strain ( $0 < b_c < 1$ ). It was found by trial calculation that the hysteresis behaviour of concrete members could be readily simulated when the pressure  $b_c$  was 0.7 and the tension  $b_c$  was 0.3 during calculation. In addition, the calculated parameters of the CDP model also cover expansive angle,  $\Psi$ ; flow potential eccentricity,  $m$ ; the ratio between the biaxial ultimate compressive strength and the uniaxial ultimate compressive strength  $\alpha_f$ ; the ratio of secondary stress invariants on the tensile, and compressive meridian planes  $\gamma$ , and bonding parameter  $\mu$ . After calculation, the suggested values of the above parameters are listed in Table 1.

### 2.2. Constitutive Model for Rebar

**2.2.1. Constitutive Relationship for Noncorroded Rebar.** Under cyclic loading, the influence of the Bauschinger effect produced by loading and unloading on the stiffness degradation of rebar must be taken into account. Owing to the actual factors affecting the Bauschinger effect being complicated, some researchers have simplified the constitutive model of rebar based on experimental data to facilitate analysis. Typically, the USTEEL02 subprogram for rebar modelling in the uniaxial hysteresis constitutive model set of PQ-Fibre [7] material developed at Tsinghua University may be used to improve

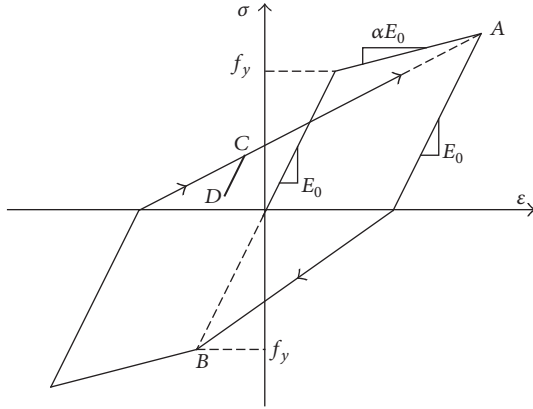


FIGURE 3: Loading and unloading: the Clough model [6].

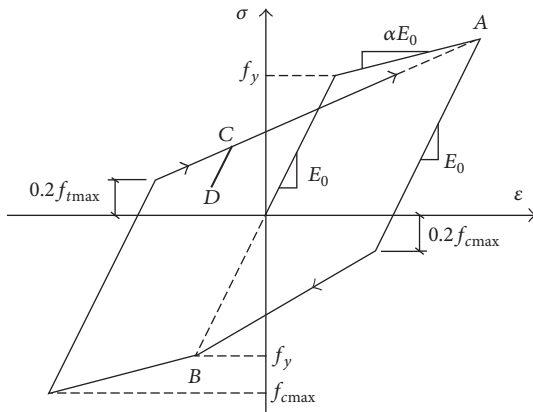


FIGURE 4: USTEEL02 rebar model [7].

the basis of the maximum point-oriented bilinear model proposed by Clough [6] (see Figure 3), which could comprehensively consider the Bauschinger effect generated during the loading-unloading-reserve loading of rebar. Besides, its feasibility has been verified [30, 31]. The Bauschinger effect on the rebar can be taken into consideration by importing the subprogram into ABAQUS.

As shown in Figure 4, the USTEEL02 model comprises four material parameters: the elastic modulus, initial yield strength, stiffness coefficient after yielding, and the ultimate plastic deformation rate; it also includes 11 state variables. Meanwhile, it considers the postyield stiffness degradation of the rebar and flexural strength degeneration of members caused by cumulative damage, including the influence of hysteresis on factors such as concrete strength and stirrup ratio. Moreover, the downtrend of the skeleton curve after member failure is considered. The parameters in the model can be determined by using [7]

$$\begin{aligned}\alpha &= \frac{E_y}{E_0}; \\ \delta &= \frac{\varepsilon_f E_0}{f_y}; \\ \varepsilon_f &= \frac{0.15\lambda_V}{\mu},\end{aligned}\quad (2)$$

where  $\alpha$  is the postyield stiffness coefficient of the rebar (suggested value: 0.001);  $E_0$  is the elastic modulus of the rebar;  $E_y$  is the postyield stiffness of the rebar;  $f_y$  is the yield strength of the rebar;  $\delta$  is the plastic deformation rate;  $\varepsilon_f$  is the plastic deformation;  $\lambda_V$  is a hoop reinforcement property; and  $\mu$  is the axial compression ratio.

**2.2.2. The Reduction of Geometric Parameters and Degradation of Mechanical Properties of Rebar under Attack from Corrosion.** In the atmosphere, the corrosion of rebar in RC structures is mainly caused by carbonisation, cracking, and spalling of the concrete cover. It can be assumed that the corrosion is uniform. As there are many corrosion products, such as rust, on the surface of the rebar during corrosion, the geometric parameters of the rebar, including its linear mass and effective cross-sectional area and its mechanical properties, such as yield strength, can be reduced to some extent. Although the corrosion of rebar is discrete, to a certain extent, the related model for the decline in yield strength and elastic modulus of rebar can be obtained through statistical analysis of multiple experiments [32]. Yuan et al. [10] provided a yield degradation model based on multiple tests on corroded rebar and found that

$$\begin{aligned}f_{yc} &= f_{y0}(1 - 2.9\eta), \quad 0 < \eta \leq 5\%, \\ f_{yc} &= f_{y0}(1.175 - 6.4\eta), \quad \eta > 5\%,\end{aligned}\quad (3)$$

where  $f_{yc}$  and  $f_{y0}$  are, respectively, the yield strength of rebar before and after corrosion and  $\eta$  stands for the corrosion rate of the cross-section [10].

As for actual RC structures and members, if the concentration of external harmful media, such as chlorides and sulphates, is high, besides, the mass of concrete being inhomogeneous and variable, the invasion time of the harmful media to the rebar will vary. Inevitably, the corrosion time for rebar is different; that is to say, nonuniform corrosion occurs. In addition, the nonuniformity is more significant with increasing corrosion which induces local pitting corrosion on the rebar which can lead to stress concentration and a further reduction in the bearing capacity of structures and members. The yield strength reduction of rebar under the effects of pitting corrosion can be computed by the following formula [33]:

$$f_y(t) = (1 - \alpha_y \eta_{\text{pit}}) f_{y0}, \quad (4)$$

where  $f_y(t)$  is the yield strength after corrosion of the rebar;  $\alpha_y$  is an empirical coefficient (suggested value: 0.005);  $\eta_{\text{pit}}$  is the corrosion rate of the pitting-corroded cross-section; and  $f_{y0}$  is the yield strength of the rebar before corrosion.

With respect to the influence of corrosion on the elastic modulus of the rebar, some researchers find that the elastic modulus of rebar changed little with increasing corrosion rate [34]. When the corrosion is uneven, Lee et al. [35] found that the corrosion of rebar can weaken its elastic modulus as given below:

$$E_{sx} = (1 - 0.0113\eta_m) E_s, \quad (5)$$

where  $E_{sx}$  is the elastic modulus of the rebar after corrosion;  $\eta_m$  is mass loss rate due to rebar corrosion; and  $E_s$  is the elastic modulus of the rebar before corrosion. The transform relationship between the cross-sectional loss rate in a pitting-corroded rebar and the mass loss rate [36] is given by

$$\eta_s = \begin{cases} \eta_m, & 0 \leq \eta_m < 2\%, \\ 0.015 + 0.97\eta_m, & 2\% \leq \eta_m < 10\%, \\ 0.062 + 0.95\eta_m, & 10\% < \eta_m \leq 20\%, \end{cases} \quad (6)$$

where  $\eta_s$  is the cross-sectional loss rate and  $\eta_m$  the mass loss rate.

For analysis, the rebar model can be reasonably simplified. (1) Assuming that the corrosion rates of stirrups and the main longitudinal reinforcement are the same and that the constraining effects of the stirrups on the core concrete are ignored, the beneficial effect of any stirrups can be neglected owing to the stirrup ratio of general RC members being low and the constraint of stirrups on the core concrete being slight. (2) As for the local nonuniform pitting corrosion of longitudinal reinforcement, the shape and distribution of pitted zones are random. If the finite element model is established according to the actual shape and distribution of these pitted zones, the modelling computational effort becomes large, while the computational efficiency decreases. Some researchers have studied the influence characteristics of pitting corrosion on RC members under uniform corrosion. Besides, they provided a conversion formula between local pitting corrosion and uniform corrosion [34] (see (7)). Thereby, the transform relation was used during this research. In addition, a uniform corrosion was used to simulate pitting corrosion of the longitudinal reinforcement

$$R = \frac{p(t)}{p_{av}(t)}. \quad (7)$$

In (7),  $p(t)$  is the maximum pit depth;  $p_{av}(t)$  is the average pit depth; and  $R$  is a pitting coefficient (suggested value  $5 \leq R \leq 13$ ) [34].

**2.3. Bond-Slip Constitutive Relationship.** There is relative slippage between concrete and rebar, when RC members are subjected to low frequency cyclic loading. To some extent, slippage can absorb the energy in members produced by external loads. One of the macro-behaviours is a pinch effect caused by hysteresis. The bond-slip stress between concrete and rebar mainly originates from friction, cohesive forces from the cement material on the rebar, and the mechanical interaction between the surface of the deformed rebar and the concrete before corrosion. The surface roughness of the rebar decreased and some threads on the surface were lost: this affected the stick-slip behaviour after corrosion of the rebar.

The relative slippage between concrete and rebar could be simulated by defining a nonlinear spring element in ABAQUS. Owing to load being added to the top side of the frame column during simulation, slippage of the rebar mainly appeared along the longitudinal column axis (the  $Z$ -direction), while horizontal,  $X$ -, and  $Y$ - directions slippage

was negligible. That is to say, two linear spring elements with larger stiffness ( $2 \times 10^{11}$  to  $2 \times 10^{13}$  N/mm) were set on the overlapped nodes of the concrete and rebar in the  $X$ - and  $Y$ -directions, and a nonlinear spring element was used in the  $Z$ -direction. The force-displacement relationship of the nonlinear spring element is given by [33]

$$F = \tau(D) A_i, \quad (8)$$

where  $\tau(D)$  is the shear stress in bond-slip and  $A_i$  is the distribution area across the corresponding contact surface of the spring.

According to the experience of the authors, the calculation mode of slippage-induced shear stress-displacement, as defined by CEB-FIB MODEL CODE 1990 [37], was applied to determine the shear stress governing bond-slip. In this way, the bond-slip force between the rebar and concrete was modelled. In addition, the mode was characterised by few parameters and a simple calculation [38]:

$$\beta = \begin{cases} 1 + 0.9943\eta_s - 0.9584\eta_s^2 + 0.3461\eta_s^3 - 0.0447\eta_s^4, & \eta_s \leq 3\%, \\ 1.4822\eta_s^{-0.4235}, & \eta_s > 3\%, \end{cases} \quad (9)$$

where  $\beta$  is the reduction coefficient for the ultimate bond strength and  $\eta_s$  is the rebar corrosion rate.

### 3. Establishment of the Finite Element Model

**3.1. Model Parameters.** To compare with existing results [13], a frame column was simulated. The cross-section measured  $200 \times 200$  mm, and the section of the foundation beam was a rectangle measuring  $250 \times 300$  mm. In addition, the concrete cover thickness was 25 mm. The longitudinal reinforcement was Grade II rebar (symmetrical), while Grade I rebar was used for the stirrups. Moreover, the design strength grade was chosen as a C25 grade concrete. Figure 5 shows the geometric parameters and the reinforcement layout. The bottom of the column was fixed. During testing, a vertical jack was used to increase the load to 325.08 kN. It was calculated that the axial compression ratio of the column was 0.27. In addition, the lateral repeated force was applied by a horizontal two-dimensional hydraulic jack sited some 100 mm below the top of the column. The measured concrete compressive strength of the mix used to form the frame column was 31.1 MPa and its tensile strength was approximately 4 MPa, and the initial elastic modulus and Poisson's ratio were approximately 30 GPa and 0.2, respectively (estimated values only). The measured yield strength of the longitudinal reinforcement in the column was 415.6 MPa and the elastic modulus was about 200 GPa before corrosion.

**3.2. Finite Element Model and Loading Scheme.** To consider the influence of corrosion on the bond-slip between the rebar and the concrete, discrete modelling was used, including C3D8R for concrete elements with a unit size of  $100 \times 25 \times 25$  mm and T3D2 for rebar with a unit size for longitudinal reinforcement and stirrups of 100 mm and 35 mm, respectively. Then a nonlinear spring constraint was imposed in the

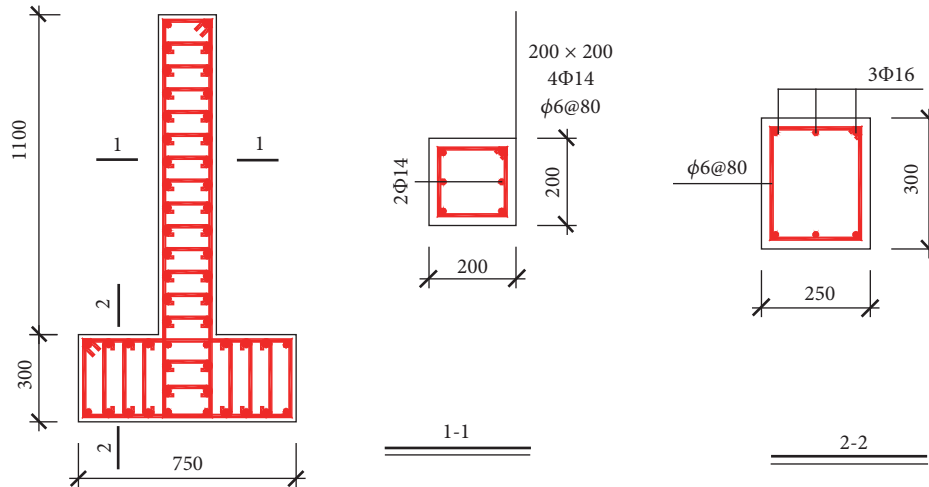


FIGURE 5: Dimensions and reinforcement layout.

longitudinal direction (the Z-axis). Besides, a linear spring constraint with a stiffness of  $2 \times 10^{12}$  N/mm was applied to the section orientation, that is to say, X- and Y-directions of the column to simulate bond-slip between the rebar and concrete. The established concrete model and framework model for the reinforcement are shown in Figure 6.

Owing to the bottom of frame column being fixed, a fixed constraint was applied at the nodes of grid at its base. A concentrated force of 325.08 kN was applied to simulate the axial compression. Reference point RPI was established at 100 mm below the top surface of column and it was coupled with the top surface. The displacement loading method was adopted to simulate the effect of lateral repeated force. Cyclic loading was performed according to displacement amplitudes  $\Delta_y, 2\Delta_y, 3\Delta_y, \dots$  with three loops *per* amplitude. Then the loading was stopped when the bearing capacity of frame column dropped to 85% of its ultimate loading capacity, among which  $1.0\Delta_y, 1.5\Delta_y, 2.0\Delta_y, \dots, \Delta_y$  were regarded as the yield displacement of the frame column.

#### 4. Numerical Simulation and Analysis of the Hysteresis Performance of Corroded RC Frame Columns

##### 4.1. Analysis of Load Cases and Calculation Parameters.

To understand the influence of different amounts of rebar corrosion on the hysteresis performance of a frame column, four sets of operating conditions, including noncorroded, slight corrosion, moderate corrosion, and severe corrosion, along with the influence of local pitting corrosion, were selected. According to the literature [33], the corresponding corrosion rates for a pitting-corroded cross-section under the four conditions above were 0%, 6.3%, 25%, and 56.3%, respectively. Assuming that pitting corrosion coefficient  $R = 5$ , the corresponding uniform corrosion rates of the rebar cross-section were 0%, 5%, 10%, and 15%, respectively (obtained by (7)). The corresponding reinforcement parameters under the

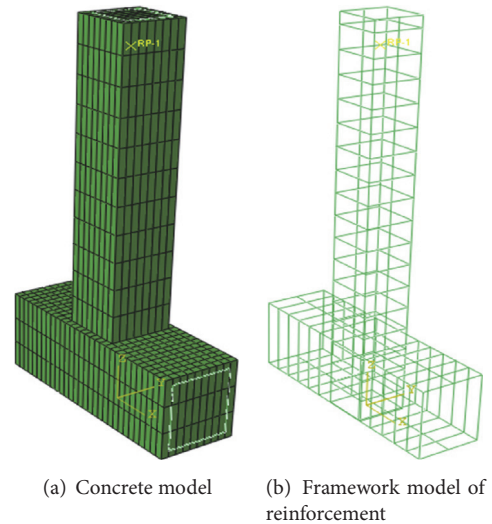


FIGURE 6: Finite element models for concrete and rebar.

four load cases, including the yield strength of the rebar and the bond-slip degradation coefficient, are listed in Table 2.

##### 4.2. Simulation Results and Analysis

**4.2.1. Uniaxial Pushover Analysis.** To obtain the yield displacements of each frame column under various corrosion conditions during loading, firstly a uniaxial pushover analysis was conducted on each frame column under different cases. The target displacement was set to 45 mm according to Chinese Standard GB50011-2010 (Code for the Seismic Design of Buildings) [39]. The results are shown in Figure 7.

As shown in Figure 7, under static displacement the corresponding peak bearing capacities under each case with different corrosion rates were as follows: 63 kN with a corrosion rate of 0%, 60 kN with a corrosion rate of 5%, 55 kN with a corrosion rate of 10%, and 49 kN with a corrosion rate

TABLE 2: Calculation parameters for different degrees of corrosion.

Corrosion rate (pitting corrosion rate)	0% (0%)	5% (6.3%)	10% (25.0%)	15% (56.3%)
Mass loss rate	0%	5.1%	10.5%	15.7%
Yield strength (MPa)	415.6	400.1	363.3	296.4
Elastic modulus (GPa)	200	197.7	176.3	164.5
Degradation coefficient of bond-slip	1.0	0.75	0.56	0.47

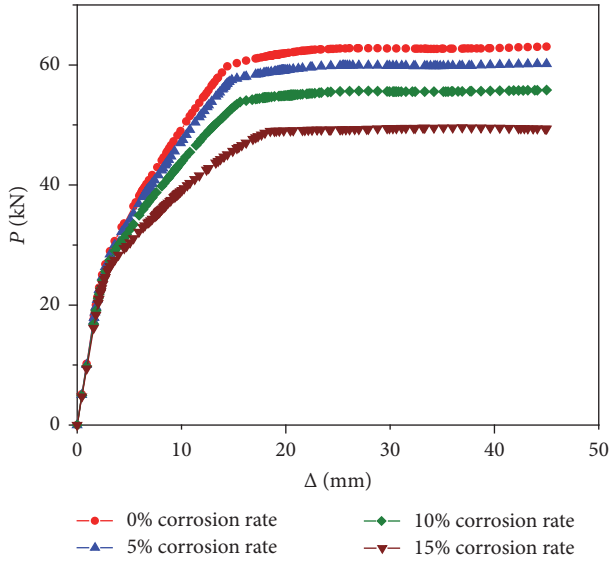


FIGURE 7: Uniaxial pushover analysis of frame columns with different corrosion rates.

of 15%. According to the PARK yield displacement principle [40], the yield displacements under cases with different corrosion rates were calculated as 10 mm with a 0% corrosion rate, 9.7 mm with a 5% corrosion rate, 8.8 mm with a 10% corrosion rate, and 7.6 mm with a 15% corrosion rate. It also can be seen that, with an increased corrosion rate, the static ultimate bearing capacity and the yield displacement of the frame column decreased after corrosion of the rebar. Compared with noncorroded columns, the static ultimate bearing capacities of columns after corrosion, respectively, fell by 4.8%, 12.7%, and 22.2%, which was linearly related to the increase of corrosion rate. This implied that the decrease of yield strength of the rebar, its elastic modulus, and section loss caused by corrosion were important factors affecting the weakening of the static bearing capacity of frame columns. Compared with the static bearing capacity, the yield displacement decreased more significantly with increasing corrosion rate. With increasing corrosion rate, the yield displacements were decreased by 5.9%, 14.1%, and 25.9%, respectively, and the rates of decrease were greater than the average cross-sectional rate of decrease and mass loss. Overall, the yield displacement and corrosion rate had a nonlinear relationship. This illustrated that the degradation of bond-slip behaviour between the rebar and the concrete plays a more important role in the weakening of the static bearing capacity of frame columns.

4.2.2. *Hysteresis Curves.* Based on the aforementioned parameters, low frequency cyclic loading and unloading were performed on frame columns under various load regimes. The comparison of simulated hysteresis curves with the experimental results [13] is shown in Figure 8.

The comparison of the FE simulated results and the experimental results shows that the simulated hysteresis curves are similar in shape to those obtained experimentally [13]. During cyclic loading, the hysteresis curve for the noncorroded column was plump and arcuate which implied that the seismic energy absorption was favourable. With an increasing rebar corrosion rate, the plumpness of the hysteresis loop decreased, while the shrinkage increased. In addition, the hysteresis curve changed to a reverse S-shape from an arcuate form so that the area within the hysteresis loop decreased, causing a severe “pinching” phenomenon. Moreover, with an increasing corrosion rate, the frequency of cyclic loading and the ultimate displacement decreased, as did the seismic energy absorption ability of the column. This suggested that rebar corrosion was an important factor affecting the seismic energy absorption ability of frame columns. With increasing corrosion, the energy dissipation capacity of the frame columns decreased, while their brittleness increased.

4.2.3. *Skeleton Curves.* Skeleton curves are obtained by connecting the ultimate loading points for each tension or compression load cycle, in the same direction, on the hysteresis curve successively. Skeleton curves describe the trajectory of the maximum peak horizontal force at each cyclic loading stage and reflect the changes in the stress and deformation of members at different stages. Therefore, skeleton curves are an important index for assessing the seismic performance of members or structures, as well as a significant basis for determining the feature points in the restoring force model for such members.

The skeleton curves of frame columns with different corrosion rates were extracted (see Figure 9). As shown in Figures 9(a) and 9(b), the numerical and experimental ultimate loads under each case with different corrosion rates were as follows: 52.3 and 50.15 kN with a corrosion rate of 0%, 47.9 and 49.65 kN with a corrosion rate of 5%, 44.8 and 49.5 kN with a corrosion rate of 10%, and 39.3 and 43.54 kN with a corrosion rate of 15%. It can be seen that the bearing capacity of the frame columns decreased with increasing rebar corrosion rate, and the numerical and experimental peak bearing capacities decreased by approximately 8.4%, 14.3%, and 24.9% and 1.0%, 1.3%, and 13.2%, respectively, during cyclic loading. Moreover, the larger the corrosion

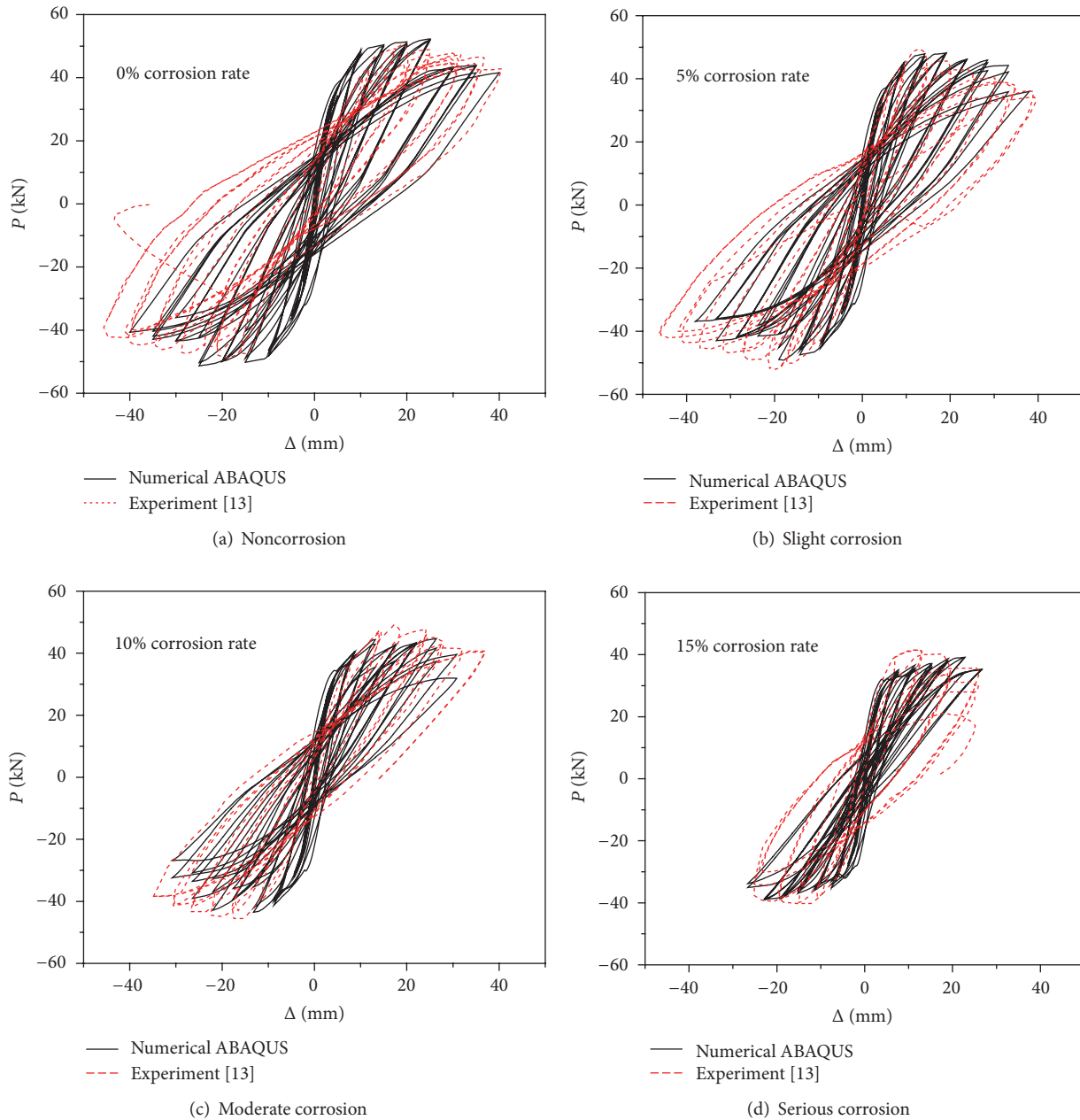


FIGURE 8: Hysteresis curves for RC columns under different corrosion rates.

rate, the greater the decrease in bearing capacity. Meanwhile, as the rebar corrosion rate increased, the rising segment of the skeleton curve was flattened and seen to have had a shortened strengthening segment, implying a weakened capacity to resist deformation, and a lower ductility of the frame columns.

It needs to be pointed out that the FE simulation results and experimental results in Figures 8 and 9 are not identical. This is mainly because there are various factors affecting the hysteretic performance of corroded RC frame columns. FE simulation cannot take all of these factors into account. In addition, the property, size, and reinforcement ratio of the concrete materials used in the tested samples are of

larger-scale with regard to their discretisation. Moreover, the loading rate and constraint conditions in the experiment exert influences on the experimental results as well. In spite of this, the authors believe that it is feasible to study the hysteretic performance of corroded RC frame columns using a FE numerical simulation.

Based on the above analysis, the following suggestions can be applied to the seismic reinforcement of corroded RC frame columns: for mildly corroded members (i.e., those with a rebar corrosion rate within 5%) whose hysteretic bearing capacity reduces slightly to within 10%, then such structures, or members, can be slightly, or non-, reinforced according to their importance in engineering practice. Regarding the

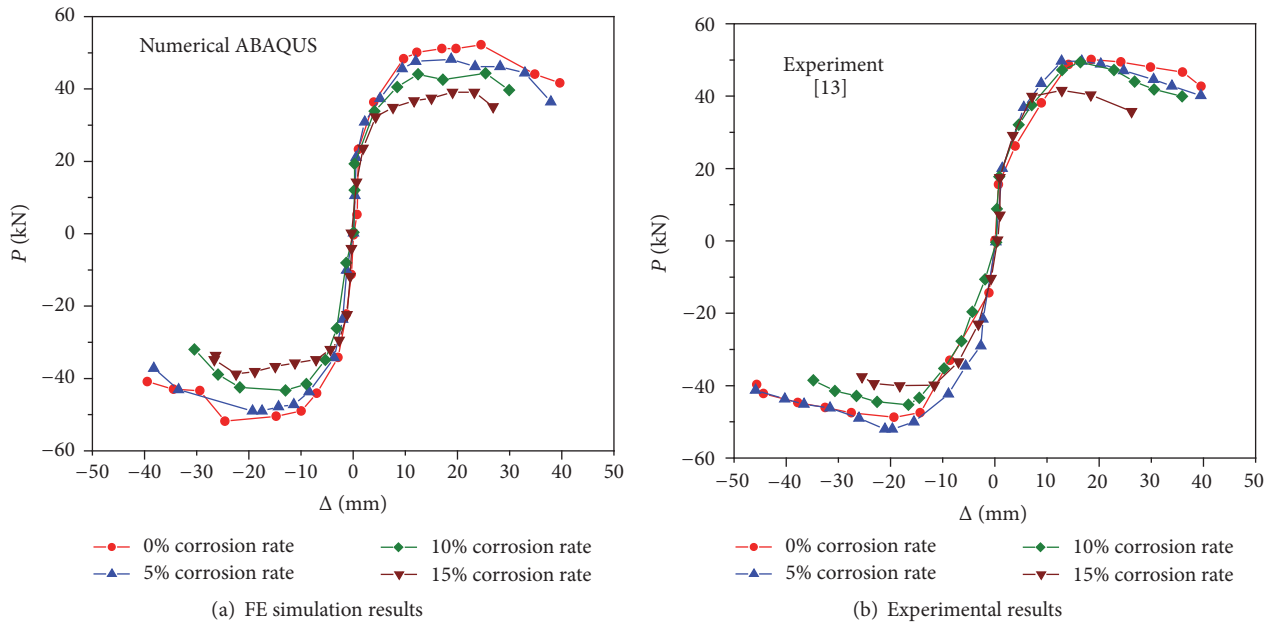


FIGURE 9: Skeleton curves for RC columns under different corrosion rates.

slightly corroded members with corrosion rates of 5% to 10%, their hysteretic bearing capacity was reduced by 10% to 20%, indicating that members were in a poor state. Therefore, such members are expected to be reasonably reinforced. Owing to the hysteretic bearing capacity of moderately corroded members (with corrosion rates of between 10% and 15%) decreased by 20% to 30%, the members need to be given more attention when designing/assessing their reinforcement as they are in poorer condition. In view of the more seriously corroded members, the corrosion rate of which is above 15%, their hysteretic bearing capacity decreases significantly (by more than 30% generally), indicating there is an increased risk from such members. Thereby, these kinds of members should be replaced.

**4.2.4. Deformation and Failure Characteristics.** To understand the final deformation and failure characteristics of corroded frame columns under cyclic loading, the stress distributions and deformed shapes of each column were extracted. Figure 10 shows the stress distributions and deformations of frame columns with different corrosion rates. It can be seen that these frame columns presented similar deformation characteristics under various operating conditions. The key difference was that the deformation became more severe as the corrosion rate increased.

Figure 11 shows seismic damage to RC columns: the deformation of such frame columns in a numerical simulation under cyclic loading was consistent with that of the column after an actual earthquake (see Figures 10 and 11). The concrete at the bottom of both columns was crushed and the rebar was bent into a cage. This indicated that the numerical simulation results for the hysteresis performance of a corroded frame column can well reflect their damage characteristics in a real earthquake.

## 5. Restoring Force Model of a Corroded RC Frame Column

**5.1. Selection of the Restoring Force Model.** In the seismic response analysis of structures, the actual hysteresis performance curves are commonly modelled (using the restoring force model). For RC structures, the restoring force model is generally divided into two levels. The first level is the restoring force model of the materials used: this is mainly designed to reveal the stress-strain relationship between rebar and concrete and is the basis for modelling the restoring forces in RC members. The second level is the restoring force model of the members, which is used to describe the hysteretic relationship between bending moment and curvature ( $M-\Phi$ ) in the beam sections and that between the load and displacement ( $P-\Delta$ ) of columns. Since the first has been extensively studied with well-acknowledged conclusions, the authors merely considered the restoring force model on a member level.

A suitable restoring force model for RC members needs to meet the following two requirements simultaneously: firstly, the model is expected to exhibit a certain precision, reflect the hysteretic performance of actual structures or members, and replicate experimental results within an acceptable tolerance through numerical simulation. Secondly, the model should be simple and practical, so that it does not present unnecessary complexity which hinders the effective performance of static elastoplastic, or dynamic nonlinear time-history, analysis.

In earthquakes, when RC structures are subjected to elastoplastic stress stages, the plastic deformation of structures can absorb large amounts of the input energy, which endows the relationship between the restoring force and displacement of members with apparent hysteretic nonlinearity. Considering this characteristic, the restoring force model for

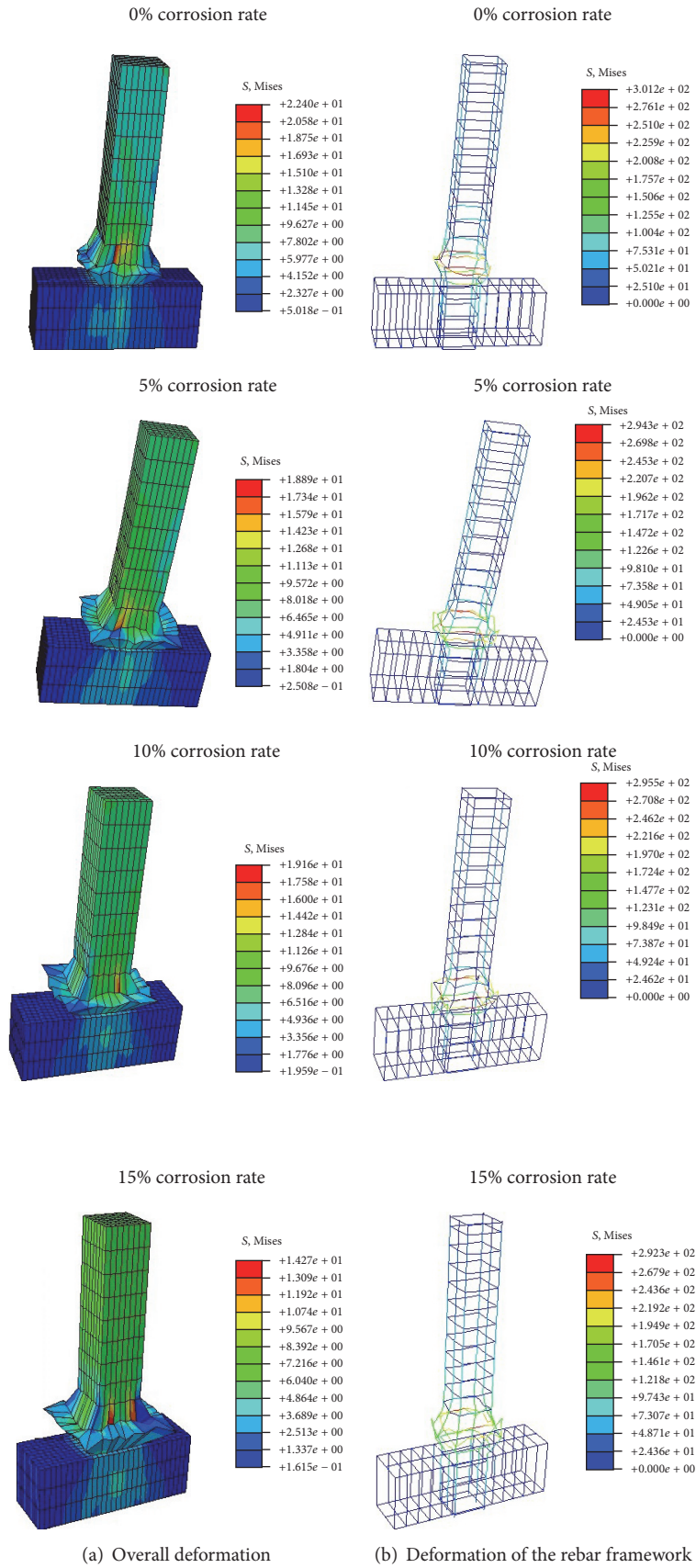


FIGURE 10: The stress, and final deformation, of corroded frame columns under cyclic loading.



FIGURE 11: Seismic damage to RC columns.

describing actual RC structures and members is divided into two types with curves and polygonal lines. The curvilinear restoring force model describes the actual stress characteristics of structures more accurately. However, its computations are complex, and the model is thereby rarely applied. As for that using polygonal lines, although it is comprised of several line segments and demonstrates a discontinuous stiffness distribution and has inflection points, it can be used without undue difficulty. Therefore, the restoring force model with polygonal lines has become widely used in practice.

The simplest nonlinear hysteretic model is bilinear elastoplastic model. Its positive loaded skeleton curve is composed of two lines and its shape is determined by yield strength, elastic stiffness, and postyield stiffness of members. As to the negative loaded skeleton curve, its loading and unloading stiffness are constant and equal to the elastic stiffness, which is similar to the positive loaded one. However, one of the shortcomings of this model is the difficulty of accounting for the stiffness deterioration of RC elements during cyclic load reversals. To overcome the problem of stiffness deterioration, Clough [6] proposed a model, which can consider the stiffness degradation of RC members under cyclic loading at nonlinear stage. Both bilinear and Clough models are simple to be applied, while they are merely suitable for members under simple bending with spindle hysteresis curves. Hence, several enhancements were done to these models in order to better simulate different characteristics of RC members. In 1970, a more refined and sophisticated hysteresis model was developed by Takeda et al. [41] on the basis of experimental results. In this model the monotonic behaviour is described by a trilinear skeleton curve which accounts for flexural cracking of concrete and yielding of reinforcing steel and also strain-hardening characteristics. The unloading stiffness was reduced by an exponential function of the previous maximum deformation. However, the Takeda model, similar to the Clough model, simulates dominantly flexural behaviour. Subsequently, a variety of improved hysteretic models emerged one after another.

To verify the effect of different hysteretic models on the dynamic response of RC frames, Anderson and Townsend [42] used four different models to describe the hysteretic behaviour of critical regions of RC members. The study shows that the most representative and practical model is the

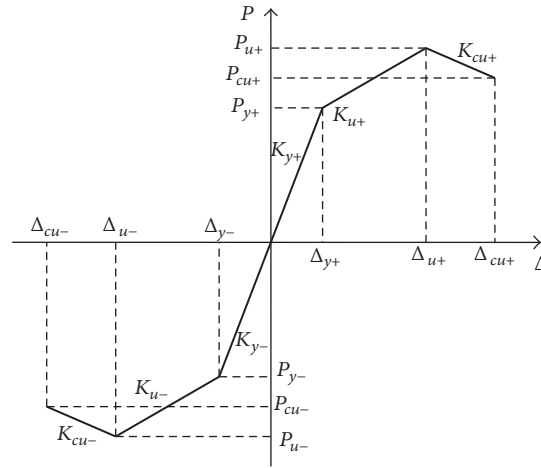
degrading trilinear (D-TRI) model. The D-TRI model uses three lines to describe the loading and restoring force skeleton curve and considers the stiffness degradation properties of an RC structure or structural component. The model can describe in more detail the cracking and yield of concrete and complex hysteresis rules. Therefore, it can preferably illustrate the relationship between the restoring force and deformation of concrete structures and members in the whole process. Due to this advantage, the D-TRI model is the most commonly used in the analysis of the elastoplastic seismic response of RC structures.

Based on the above analysis, we use the D-TRI model to investigate the hysteresis performance of RC frame columns in this paper. The skeleton curve and basic hysteresis rule of D-TRI model are shown in Figure 12. The skeleton curve was determined by parameters including yield load  $P_y$ , yield displacement  $\Delta_y$ , ultimate load  $P_u$ , peak displacement  $\Delta_u$ , failure load  $P_{cu}$ , and failure displacement  $\Delta_{cu}$ . The modified Clough model, that is, the maximum historical displacement-oriented model, was adopted as the basic hysteretic rule here. The loading was conducted in numerical order [43, 44], as shown in Figure 12(b).

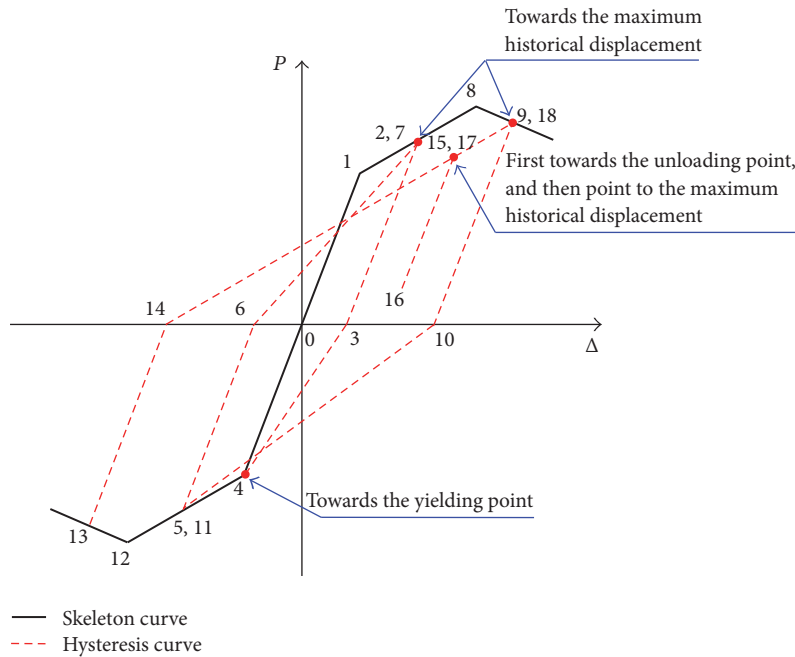
In Figure 12,  $K_y$  is the initial elastic stiffness,  $K_u$  is the postyield stiffness, and  $K_{cu}$  is softening stiffness. When the horizontal seismic force exceeded the yield loading  $P_y$  or the seismic displacement was greater than the yield displacement  $\Delta_y$ , it was a strengthening process, while once the force reached the ultimate load, it became a softening process.

Once the key points of the bearing capacity and displacement were determined on the skeleton curve in the D-TRI model, the values of  $K_y$ ,  $K_u$ , and  $K_{cu}$  can be calculated as follows:

$$\begin{aligned}
 K_y &= \frac{P_y}{\Delta_y}, \\
 K_u &= \frac{(P_u - P_y)}{(\Delta_u - \Delta_y)}, \\
 K_{cu} &= \frac{(P_{cu} - P_u)}{(\Delta_{cu} - \Delta_u)}.
 \end{aligned} \tag{10}$$



(a) Skeleton curve: D-TRI model



(b) Basic hysteresis rule: D-TRI model

FIGURE 12: D-TRI model.

After determining the above parameters, the formula for the restoring force model of members can be established. Furthermore, owing to symmetrical reinforcement being generally applied to RC frame columns in practice, the hysteresis curve is basically central-symmetric under cyclic loading. Therefore, to simplify the computation, it was assumed that the restoring force model was central-symmetric, that is,  $P_{y+} = P_{y-}$  and  $\Delta_{y+} = \Delta_{y-}$ .

For corroded RC frame columns, it can be seen from Section 4.2 that the hysteresis curves and skeleton curves of corroded members exhibited basically identical shapes to those of noncorroded members under low frequency cyclic loading. The difference was that when influenced by rebar

corrosion, the parameters depicting the characteristics of the restoring force decreased. Meanwhile, as seen in Figure 9, the trends for the skeleton curves of corroded, and noncorroded, members were basically consistent and roughly corresponded to the features of a trilinear equivalent model. The difference lays in the different coordinates of the feature points of bearing capacity and displacement of members.

Based on the above analysis, it was assumed that corroded and noncorroded members had similar restoring force models: therefore D-TRI model was applicable to both kinds of members, as displayed in Figure 13. In this way, (10) were used to compute key parameters in the restoring force model for noncorroded columns. Then, the parameter values of

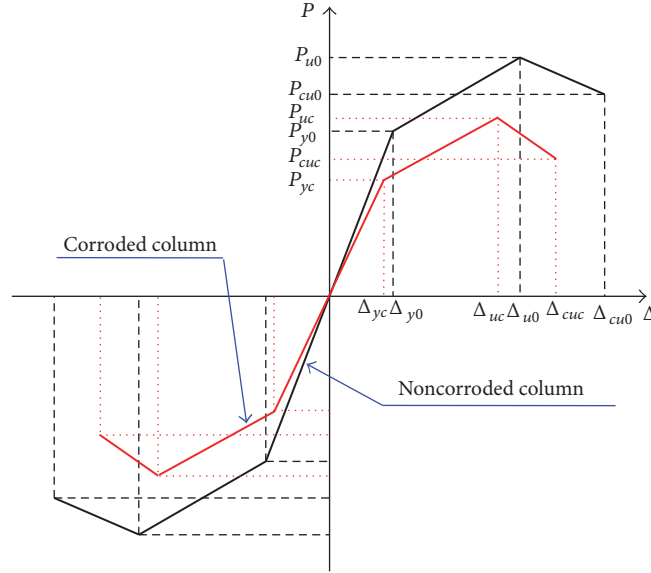


FIGURE 13: Skeleton curves for D-TRI model of corroded, and noncorroded, columns.

the key points on the skeleton curve for the restoring force model of corroded columns were obtained by introducing the corrosion-induced reduction coefficient of the mechanical performance index of frame columns.

## 5.2. Determining Key Parameters of the Skeleton Curve for the Restoring Force Model

### 5.2.1. Determining Key Parameters for Noncorroded Members.

The determination of the feature point parameters of the skeleton curve for the restoring force model of a noncorroded RC column played a fundamental role in establishing the restoring force model for corroded ones.

(1) *Yield Load  $P_{y0}$  and Yield Displacement  $\Delta_{y0}$ .* Yield load  $P_{y0}$  is defined as the corresponding horizontal thrust when tensile rebar yields at the maximum bending moment section; the corresponding bending moment is the yield moment  $M_{y0}$ . According to plane cross-section assumptions, it can be found that the relationship between yield load  $P_{y0}$  and bending moment  $M_{y0}$  is

$$P_{y0} = \frac{2M_{y0}}{H_0}, \quad (11)$$

where  $H_0$  is the height from the horizontal loading point of the frame column to the column base and  $M_{y0}$  is the yield moment of the cross-section, which can be calculated on the basis of [45]

$$\begin{aligned} M_{y0} = & A_{s0}f_{y0}(h_0 - a) + n_0bh_0f_{c0}\left(\frac{h}{2} - a\right) \\ & - 0.5\kappa bh_0f'_{c0}\left(\frac{\kappa h_0}{3} - a\right), \\ f'_{c0} = & \frac{\kappa f_{y0}}{(1 - \kappa)\alpha_E}, \\ \alpha_E = & \frac{E_s}{E_c}, \end{aligned} \quad (12)$$

where  $A_{s0}$  is the tensile longitudinal reinforcement area;  $f_{y0}$  is the design yield strength of the longitudinal reinforcement;  $h_0$  is the effective height of the cross-section of the member;  $h$  is the height of the cross-section of the member;  $b$  is the width of the cross-section of the member;  $a$  is the distance from the centre of the main tension reinforcement to the edge of the cross-section;  $n_0$  is the axial compression ratio;  $f_{c0}$  is the measured strength of the concrete [46];  $\kappa$  is the relative height of the compression zone;  $f'_{c0}$  is the stress in the concrete on a cross-section when the tensile rebar yields, where  $f'_{c0} > f_{c0}$ , setting  $f'_{c0} = f_{c0}$ ;  $E_s$  is the elastic modulus of the rebar; and  $E_c$  is the measured elastic modulus of concrete [46].

The relative height of the compression zone  $\kappa$  is given by [45]

$$\begin{aligned} \kappa = & \left\{ \left( \rho_t + \frac{n_0}{\alpha_f} \right)^2 \alpha_E^2 + \left[ \rho_t \left( 1 + \frac{a}{h_0} \right) + \frac{2n_0}{\alpha_f} \right] \alpha_E \right\}^{0.5} \\ & - \left( \rho_t + \frac{n_0}{\alpha_f} \right) \alpha_E, \end{aligned} \quad (13)$$

where  $\alpha_f = f_{y0}/f_{c0}$ ;  $\rho_t$  is the reinforcement ratio of the main tension reinforcement.

As the stiffness degradation is not obvious from concrete cracking to rebar yielding in actual frame columns, the member is assumed to be perfectly elastic before rebar yielding. Therefore, the yield displacement  $\Delta_{y0}$  [45] is

$$\Delta_{y0} = \frac{H_0^2 f_y}{3h_0(1 - \kappa)E_s}. \quad (14)$$

(2) *Ultimate Load  $P_{u0}$  and Peak Displacement  $\Delta_{u0}$ .* By regression analysis on the obtained data [47], the ultimate load was given by

$$P_{u0} = (1.24 - 0.075\rho_t n_0 - 0.5n_0)P_{y0}. \quad (15)$$

TABLE 3: Calculated results of yield load ( $P_y$ ) and yield displacement ( $\Delta_y$ ) and those obtained through FE simulation and experiments.

Corrosion rate (%)	Formula (a)	Numerical ABAQUS (b)	Experiment [13] (c)	Relative error (%) $((a) - (c))/(c) \times 100\%$
Yield load $P_y$ (kN)				
0	47.6	49.0	41.78	13.9
5	43.8	45.0	41.15	6.4
10	39.3	40.5	42.05	-6.5
15	34.0	35.0	37.11	-8.4
Yield displacement $\Delta_y$ (mm)				
0	9.8	10.0	9.32	5.2
5	9.7	9.7	9.36	3.6
10	9.2	8.8	10.84	-15.1
15	8.2	7.6	7.85	4.5

Considering the influence on the mechanical properties of the members of factors such as the properties of the concrete, axial compression ratio, and shear span ratio, during the determination of peak displacement, an empirical method was used to fit the calculated data to obtain an expression for the peak displacement [47]:

$$\Delta_{u0} = \frac{1}{0.045 + 1.75n_0}. \quad (16)$$

(3) Failure Load  $P_{cu0}$  and Failure Displacement  $\Delta_{cu0}$ . In general, if the bearing capacity of RC members was reduced to 85% of the ultimate load, the structural, or member, failure was determined as a failure during testing; namely,

$$P_{cu0} = 0.85P_{u0}. \quad (17)$$

The corresponding displacement to failure load  $P_{cu0}$  was a failure displacement  $\Delta_{cu0}$ . On the basis of the statistical analysis of simulated data [47], the effect of factors, including the properties of the concrete, axial compression ratio, reinforcement ratio of tensile reinforcement, and section size, was taken into account to determine the calculation method of failure displacement as

$$\Delta_{cu0} = (5.20 - 4.1n_0) \Delta_{y0}. \quad (18)$$

5.2.2. Determining Key Parameters for Corroded Members. Rebar corrosion can induce a decrease in the cross-sectional area thereof, as well as its yield strength, bond behaviour, ultimate elongation, and so forth. Besides, there are many coupled factors which could interact: generally, corrosion degradation parameters are usually related to the axial compression ratio  $n_0$  and corrosion rate  $\eta_s$ . Hence, the key parameters for a corroded member were established by analysing and fitting the data [47]:

(1) Yield load  $P_{yc}$  and yield displacement  $\Delta_{yc}$ :

$$\begin{aligned} P_{yc} &= [0.9993 - 0.0531\eta_s n_0 - 0.0043(\eta_s n_0)^2] P_{y0}, \\ \Delta_{yc} &= [1.0015 + 0.01\eta_s n_0 - 0.0123(\eta_s n_0)^2] \Delta_{y0}. \end{aligned} \quad (19)$$

(2) Ultimate load  $P_{uc}$  and peak displacement  $\Delta_{uc}$ :

$$\begin{aligned} P_{uc} &= [0.9964 - 0.0475\eta_s n_0 + 0.003(\eta_s n_0)^2] P_{y0}, \\ \Delta_{uc} &= \mu_{u0} \Delta_{yc}. \end{aligned} \quad (20)$$

(3) Failure load  $P_{cuc}$  and failure displacement  $\Delta_{cuc}$ :

$$\begin{aligned} P_{cuc} &= 0.85P_{uc}, \\ \Delta_{cuc} &= [0.9871 - 0.0818\eta_s n_0] \Delta_{cu0}. \end{aligned} \quad (21)$$

For noncorroded and corroded members, the corresponding stiffness parameters can be acquired by substituting the bearing capacity and key displacement parameters on the skeleton curve, respectively.

### 5.3. Verifying the Reliability of the Restoring Force Model

5.3.1. Verifying the Accuracy of Key-Point Parameters of the Skeleton Curve. The parameters for each member in Section 3.1, such as material property parameters, axial compression ratio, and corrosion ratio, were substituted into (11) to (21). By doing so, the authors compared the calculated, FE simulated, and experimental results for key-point parameters of the skeleton curve for the restoring force model, as shown in Tables 3–5. It can be seen that the computed key-point parameters of the skeleton curve for the restoring force model of the corroded frame columns were generally consistent with those acquired in FE simulation and experiments [13]. Except for a few data points with large discrepancies with the experimental results (of up to 25%), most of the discrepancies were within 15%. This indicated that the proposed formulas for fitting the key-point parameters of the skeleton curve were reasonable.

5.3.2. Validation of the Accuracy of the Skeleton, and Hysteresis, Curves. The calculated key-point parameters of skeleton curve for the restoring force model in Section 5.3.1 were substituted into (10). Then according to the basic hysteresis rule shown in Figure 12(b), the skeleton, and hysteresis,

TABLE 4: Computed results of ultimate load  $P_u$  and peak displacement  $\Delta_u$  and those acquired by FE simulation and experiments.

Corrosion rate (%)	Formula (a)	Numerical ABAQUS (b)	Experiment [13] (c)	Relative error (%) $((a) - (c))/(c) \times 100\%$
Ultimate load $P_u$ (kN)				
0	52.2	52.3	50.15	4.1%
5	49.0	47.9	49.65	-1.3%
10	46.5	44.8	49.5	-6.1%
15	44.5	39.3	43.54	2.2%
Peak displacement $\Delta_u$ (mm)				
0	23.6	24.5	22.54	4.7
5	22.9	18.3	22.37	2.4
10	20.8	25.9	19.75	5.3
15	17.9	22.4	14.32	25.0

TABLE 5: Calculated results of failure load  $P_{cu}$  and failure displacement  $\Delta_{cu}$  and those obtained in FE simulation and experiments.

Corrosion rate (%)	Formula (a)	Numerical ABAQUS (b)	Experiment [13] (c)	Relative error (%) $((a) - (c))/(c) \times 100\%$
Failure load $P_{cu}$ (kN)				
0	44.4	42.5	42.63	4.2
5	41.7	43.6	42.2	-1.2
10	39.5	40.2	42.07	-6.1
15	37.8	35.3	37.01	2.1
Failure displacement $\Delta_{cu}$ (mm)				
0	40.9	39.5	41.54	3.4
5	35.9	34.0	39.51	-9.1
10	31.3	30.0	32.52	-3.8
15	26.8	26.3	24.1	11.2

curves of the corroded frame columns with their different corrosion rates were obtained, as shown in Figure 14.

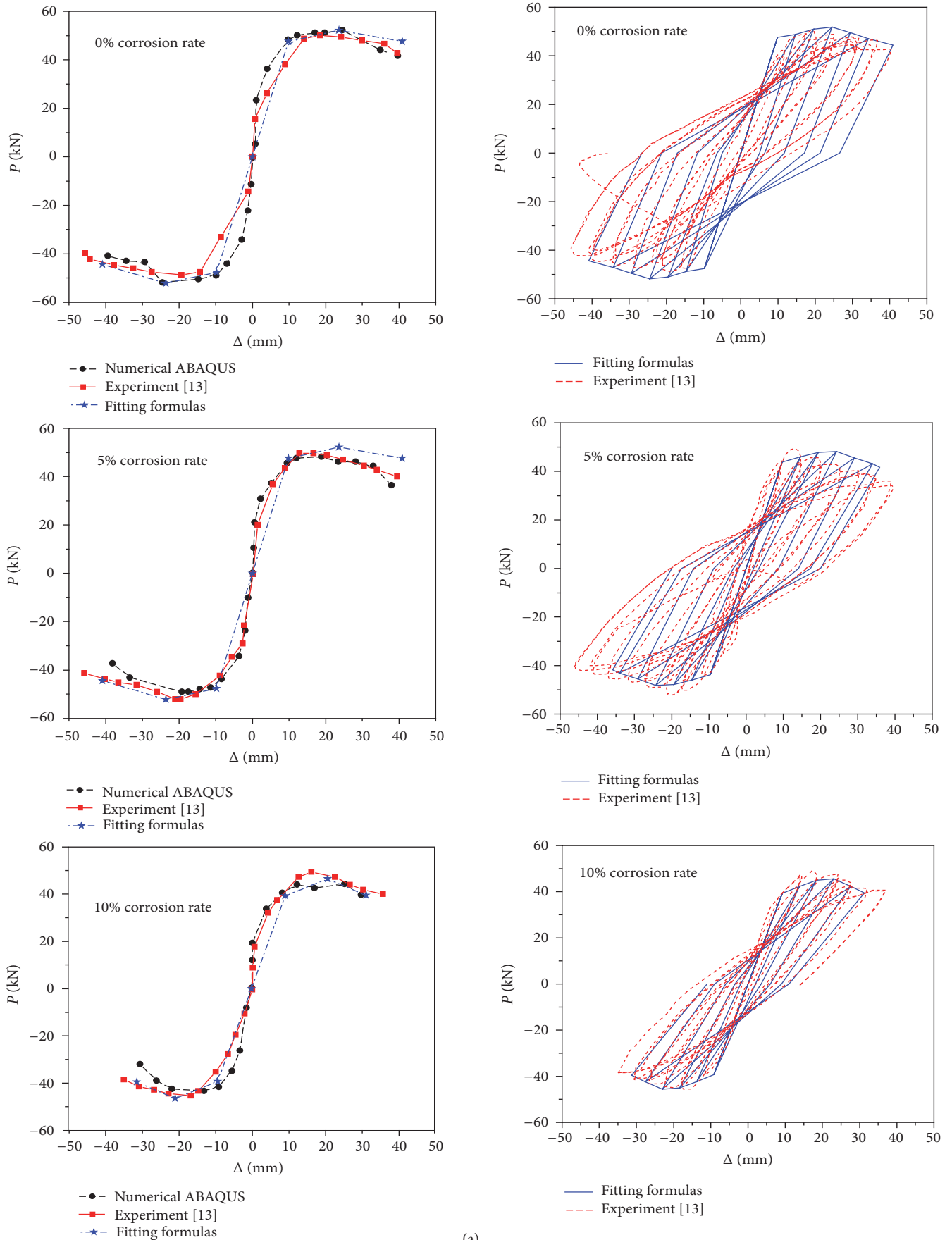
From Figure 14, it could be seen that the hysteresis curves and skeleton curves of the restoring force model obtained by fitting formulas were generally consistent with those obtained in the experiment: with the increased rate of corrosion, the bearing capacity and the area within the hysteresis loop of the frame column decreased. This implied that the seismic energy dissipation capacity of the corroded frame columns decreased, while their brittleness increased. These results validated the idea that numerical simulation would be a simple, feasible method of constructing the restoring force model of corroded RC members: the established model was found to have been accurate and was deemed reasonable.

## 6. Conclusions

ABAQUS finite element software was used for the numerical simulation analysis of the hysteresis performance of RC frame columns with four different amounts of corrosion: non-corroded, slight corrosion, moderate corrosion, and severe corrosion. In addition, the analytical results were compared with published experimental results and actual earthquake damage characteristics of framed columns. On this basis, a D-TRI model was established to reflect the hysteresis performance of corroded RC frame columns. Moreover, the

influence of factors including the rebar corrosion rate and axial compression ratio was taken into consideration. The main conclusions were as follows:

- (1) The seismic bearing capacity of a frame column would be significantly decreased after corrosion of its rebar. In addition, with increasing rebar corrosion rate, the diminution of the bearing capacity gradually increased, including the corrosion-induced degradation of the bond-slip behaviour between rebar and concrete, which played an important role in weakening the hysteretic bearing capacity.
- (2) Along with the increased amount of rebar corrosion, the plumpness of the hysteresis loop of a frame column decreased, while the shrinkage increased. Meanwhile, the hysteresis curve became a reverse S-shape, having originally been arcuate. Furthermore, the area within the hysteresis loop became smaller and generated severe "pinching": this explained why the seismic energy dissipation capacity of such frame columns decreased, while their brittleness increased.
- (3) The FE simulated frame column showed failure and deformations similar to those experiencing actual earthquakes under cyclic loading. This suggested that it was feasible to simulate the hysteresis performance of corroded RC frame columns using



(a)  
FIGURE 14: Continued.

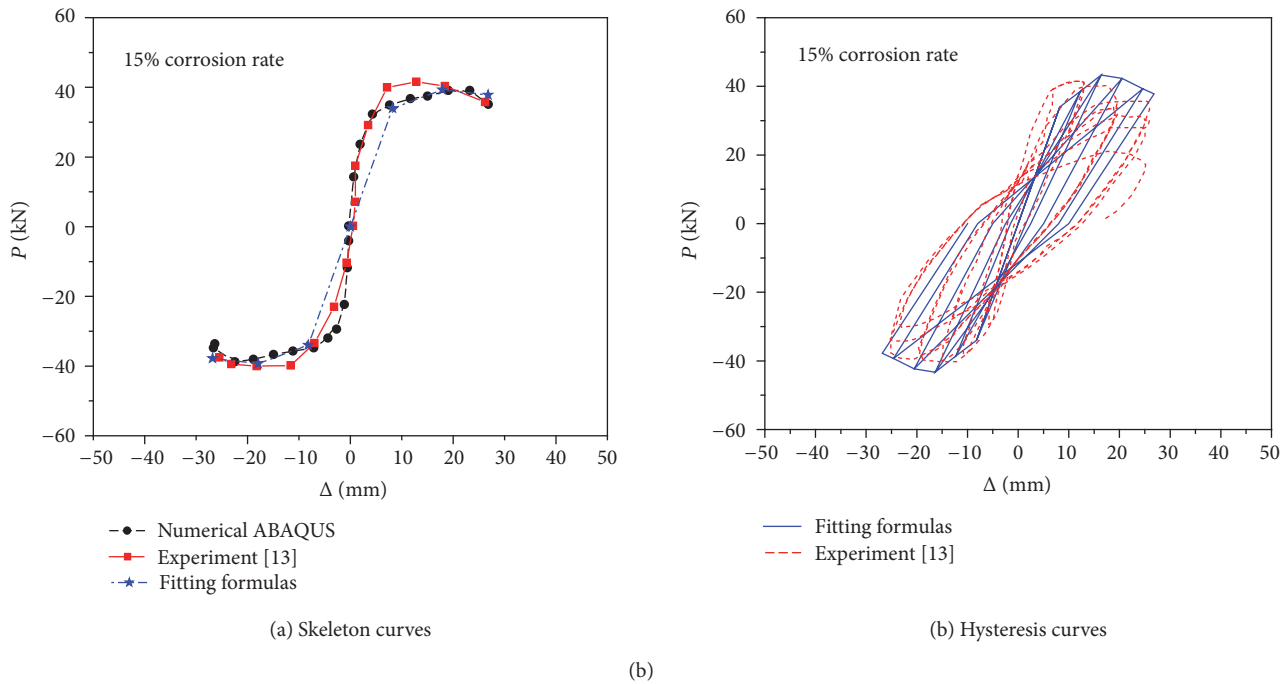


FIGURE 14: Comparison of skeleton curves and hysteresis curves obtained by the restoring force model and experiment.

the FE method. Furthermore, the simulated results favourably described the failure characteristics of the frame column in earthquake conditions.

- (4) The hysteresis, and skeleton, curves of the corroded RC frame column presented basically consistent shapes with those of a noncorroded member under low-cyclic loading, which broadly conformed to the characteristics of a trilinear distribution. Therefore, a restoring force model applicable to corroded RC frame columns, the D-TRI restoring force model, for instance, could be established based on that of noncorroded RC members using the existing Clough hysteresis rule.
- (5) The skeleton, and hysteresis, curves of corroded RC frame columns, predicted using the D-TRI model, were similar to those from experimental results. Except for a few data points which showed large discrepancies (25%) with the experimental results, most of the calculated key-point parameters of the skeleton curve presented discrepancies of less than 15%. Moreover, the hysteresis curve showed similar characteristics to the experimental results. This proved that the restoring force model established for the corroded RC members in this research using numerical simulation was simple and applicable, as well as accurate and rational.

### Competing Interests

The authors declare that there is no conflict of interests regarding the publication of this paper.

### Acknowledgments

This research has been funded by the National Natural Science Foundation of China (Grant nos. 51520105012 and 51278303) and Outstanding Young Talent Research Fund of Zhengzhou University (Grant no. 1521322004) and Guangdong Provincial Key Laboratory of Durability for Civil Engineering, Shenzhen University (Grant no. GDDCE 12-06). In addition, the authors would like to thank Dr. Y. W. Zhou and all study participants for their helpful discussions.

### References

- [1] H. Yalciner, S. Sensoy, and O. Eren, "Time-dependent seismic performance assessment of a single-degree-of-freedom frame subject to corrosion," *Engineering Failure Analysis*, vol. 19, no. 1, pp. 109–122, 2012.
- [2] P. A. Sadegh, C. Dehghanian, and A. Kosari, "Corrosion protection of the reinforcing steels in chloride-laden concrete environment through exoxy/polyanilin-camphorsulfonate," *Corrosion Science*, vol. 90, pp. 239–247, 2015.
- [3] D.-E. Choe, P. Gardoni, D. Rosowsky, and T. Haukaas, "Probabilistic capacity models and seismic fragility estimates for RC columns subject to corrosion," *Reliability Engineering and System Safety*, vol. 93, no. 3, pp. 383–393, 2008.
- [4] L. Berto, R. Vitaliani, A. Saetta, and P. Simioni, "Seismic assessment of existing RC structures affected by degradation phenomena," *Structural Safety*, vol. 31, no. 4, pp. 284–297, 2009.
- [5] L. Berto, A. Saetta, and P. Simioni, "Structural risk assessment of corroding RC structures under seismic excitation," *Construction and Building Materials*, vol. 30, pp. 803–813, 2012.
- [6] R. W. Clough, "Effect of stiffness degradation on earthquake ductility requirements," Tech. Rep. SESM66-16, Department of

- Civil Engineering, University of California, Berkeley, Berkeley, Calif, USA, 1966.
- [7] Z. Qu, "A collection of user-defined uniaxial hysteretic models for ABAQUS/Standard," 2007, <http://www.quzhe.net/PQFiber-en.htm>.
  - [8] S. Malekpour and F. Dashti, "Application of the direct displacement based design methodology for different types of RC structural systems," *International Journal of Concrete Structures and Materials*, vol. 7, no. 2, pp. 135–153, 2013.
  - [9] K. Ramin and M. Fereidoonfar, "Finite element modeling and nonlinear analysis for seismic assessment of off-diagonal steel braced RC frame," *International Journal of Concrete Structures and Materials*, vol. 9, no. 1, pp. 89–118, 2015.
  - [10] Y. S. Yuan, F. P. Jia, and Y. Cai, "The structural behavior deterioration model for corroded reinforced concrete beams," *China Civil Engineering Journal*, vol. 34, pp. 47–52, 2001.
  - [11] J.-K. Song, J. Kim, H.-B. Song, and J.-W. Song, "Effective punching shear and moment capacity of flat plate-column connection with shear reinforcements for lateral loading," *International Journal of Concrete Structures and Materials*, vol. 6, no. 1, pp. 19–29, 2012.
  - [12] Q.-J. Chen, J. Cai, M. A. Bradford, X. Liu, and Z.-L. Zuo, "Seismic behaviour of a through-beam connection between concrete-filled steel tubular columns and reinforced concrete beams," *Engineering Structures*, vol. 80, pp. 24–39, 2014.
  - [13] X. X. Chen, *Study and Evaluation on Seismic Performance of Existing Reinforced Concrete Frame*, Xi'an University of Architecture and Technology, Xi'an, China, 2011.
  - [14] T.-H. Kim, D.-J. Seong, and H. M. Shin, "Seismic performance assessment of hollow reinforced concrete and prestressed concrete bridge columns," *International Journal of Concrete Structures and Materials*, vol. 6, no. 3, pp. 165–176, 2012.
  - [15] R. He, L. H. Sneed, and A. Belarbi, "Rapid repair of severely damaged RC columns with different damage conditions: an experimental study," *International Journal of Concrete Structures and Materials*, vol. 7, no. 1, pp. 35–50, 2013.
  - [16] T.-H. Kim, "Comparison of totally prefabricated bridge substructure designed according to Korea Highway Bridge Design (KHBD) and AASHTO-LRFD," *International Journal of Concrete Structures and Materials*, vol. 7, no. 4, pp. 319–332, 2013.
  - [17] H.-S. Lee, T. Kage, T. Noguchi, and F. Tomosawa, "An experimental study on the retrofitting effects of reinforced concrete columns damaged by rebar corrosion strengthened with carbon fiber sheets," *Cement and Concrete Research*, vol. 33, no. 4, pp. 563–570, 2003.
  - [18] O. Ozcan, B. Binici, and G. Ozcebe, "Improving seismic performance of deficient reinforced concrete columns using carbon fiber-reinforced polymers," *Engineering Structures*, vol. 30, no. 6, pp. 1632–1646, 2008.
  - [19] J. Li, J. Gong, and L. Wang, "Seismic behavior of corrosion-damaged reinforced concrete columns strengthened using combined carbon fiber-reinforced polymer and steel jacket," *Construction and Building Materials*, vol. 23, no. 7, pp. 2653–2663, 2009.
  - [20] Y. Ma, Y. Che, and J. Gong, "Behavior of corrosion damaged circular reinforced concrete columns under cyclic loading," *Construction & Building Materials*, vol. 29, pp. 548–556, 2012.
  - [21] F. Biondini, E. Camnasio, and A. Titi, "Seismic resilience of concrete structures under corrosion," *Earthquake Engineering & Structural Dynamics*, vol. 44, no. 14, pp. 2445–2466, 2015.
  - [22] J. Lubliner, J. Oliver, S. Oller, and E. Oñate, "A plastic damage model for concrete," *International Journal of Solids and Structures*, vol. 25, no. 3, pp. 299–326, 1989.
  - [23] J. Lee and G. L. Fenves, "Plastic-damage model for cyclic loading of concrete structures," *Journal of Engineering Mechanics*, vol. 124, no. 8, pp. 892–900, 1998.
  - [24] U. Cicekli, G. Z. Voyiadjis, and R. K. Abu Al-Rub, "A plasticity and anisotropic damage model for plain concrete," *International Journal of Plasticity*, vol. 23, no. 10–11, pp. 1874–1900, 2007.
  - [25] S. J. George and Y. Tian, "Structural performance of reinforced concrete flat plate buildings subjected to fire," *International Journal of Concrete Structures and Materials*, vol. 6, no. 2, pp. 111–121, 2012.
  - [26] Y. F. Fan, Z. G. Huang, J. M. Li, and L. G. Guo, "Research on cohesive property between reinforcement and concrete of corroded RC member," *Industrial Construction*, vol. 29, pp. 49–51, 1999.
  - [27] H.-K. Liu and J. Li, "Constitutive law of attacked concrete," *Journal of Building Materials*, vol. 14, no. 6, pp. 736–741, 2011.
  - [28] GB50010, *Code for Design of Concrete Structures*, National Standard of P.R. China, Architecture & Building Press, Beijing, China, 2011.
  - [29] V. Birtel and P. Mark, "Parameterised finite element modelling of RC beam shear failure," in *Proceedings of the ABAQUS Users' Conference*, pp. 95–108, Boston, Mass, USA, 2006.
  - [30] X. L. Wang, X. Z. Lu, and L. P. Ye, "Numerical simulation for the hysteresis behavior of RC columns under cyclic loads," *Engineering Mechanics*, vol. 24, no. 12, pp. 76–81, 2007.
  - [31] Z. Qu, "Predicting nonlinear response of an RC bridge pier subject to shake table motions," in *Proceedings of the 9th International Conference on Urban Earthquake Engineering (9CUEE '12)*, pp. 1717–1724, Tokyo, Japan, 2012.
  - [32] W.-L. Qu and Y. Wang, "Investigation on force-bearing capacity of corroded reinforced concrete beam by using nonlinear finite element analysis," *Journal of Wuhan University of Technology*, vol. 29, no. 6, pp. 73–75, 2007.
  - [33] W. L. Jin and J. Xia, "Influence of pitting corrosion on the bending capacity of reinforced concrete beams," *Building Structure*, vol. 39, pp. 100–102, 2009.
  - [34] W. P. Zhang, D. F. Shang, and X. L. Gu, "Stress-strain relationship of corroded steel bars," *Journal of Tongji University (Natural Science)*, vol. 34, no. 5, pp. 586–592, 2006.
  - [35] H. S. Lee, T. Noguchi, and F. Tomosawa, "FEM analysis for structure performance of deteriorated RC structures due to the corrosion of rebar," in *Proceedings of the 2nd International Conference on Concrete under Severe Conditions*, pp. 327–336, E&FN Spon, Tromso, Norway, June 1998.
  - [36] X. H. Wang and T. Y. Zhong, "Relation between the loss coefficient of the corroded rebar's cross-section in concrete and that of its weight," *Research and Application of Building Materials*, no. 1, pp. 4–6, 2005.
  - [37] MC90 CEB-FIP Model Code (1990), *Design of Concrete Structures*, British Standard Institution, London, UK, 1993.
  - [38] Y. Liang, X. Y. Luo, X. Q. Xiao, and Y. F. Zhang, "Experimental study on bond-slip performance of corroded reinforced concrete," *Industrial Construction*, vol. 42, no. 10, pp. 95–100, 2012.
  - [39] "Code for seismic design of buildings," National Standard of the People's Republic of China GB50011, China Architecture & Building Press, Beijing, China, 2010.
  - [40] R. Park, "Evaluation of ductility of structures and structural assemblages from laboratory testing," *Bulletin of the New*

- Zealand National Society for Earthquake Engineering*, vol. 22, no. 3, pp. 155–165, 1989.
- [41] T. Takeda, M. A. Sozen, and N. N. Nielsen, “Reinforced concrete response to simulate earthquakes,” *Journal of the Structural Division*, ASCE, vol. 96, no. 12, pp. 2557–2573, 1970.
- [42] J. C. Anderson and W. H. Townsend, “Models for RC frames with degrading stiffness,” *Journal of the Structural Division*, vol. 103, no. 12, pp. 2361–2376, 1977.
- [43] L. F. Ibarra, R. A. Medina, and H. Krawinkler, “Hysteretic models that incorporate strength and stiffness deterioration,” *Earthquake Engineering & Structural Dynamics*, vol. 34, no. 12, pp. 1489–1511, 2005.
- [44] W. Shi, X. Lu, H. Guan, and L. Ye, “Development of seismic collapse capacity spectra and parametric study,” *Advances in Structural Engineering*, vol. 17, no. 9, pp. 1241–1255, 2014.
- [45] J. P. Ou, Z. He, B. Wu, and F. W. Qiu, “Seismic damage performance-based design of reinforced concrete structures,” *Earthquake Engineering and Engineering Vibration*, vol. 19, pp. 21–30, 1999.
- [46] ACI Committee 318, *Building Code Requirements for Structural Concrete and Commentary (ACI318-08)*, American Concrete Institute, Farmington Hills, Miss, USA, 2008.
- [47] J. Y. Shen, *Analysis of Hysteresis Performance of the Corroded Reinforced Concrete Columns and Beams*, Zhengzhou University, Zhengzhou, China, 2014.

## Research Article

# Determination of the Transport Properties of Structural Concrete Using AC Impedance Spectroscopy Techniques

Lipeng Wu, Peng Dai, and Yong Li

*School of Civil Engineering, Shijiazhuang Tiedao University, Shijiazhuang 050043, China*

Correspondence should be addressed to Lipeng Wu; [lipengwu@outlook.com](mailto:lipengwu@outlook.com)

Received 11 July 2016; Accepted 5 October 2016

Academic Editor: Song Han

Copyright © 2016 Lipeng Wu et al. This is an open access article distributed under the Creative Commons Attribution License, which permits unrestricted use, distribution, and reproduction in any medium, provided the original work is properly cited.

All over the world, particularly in severe environmental conditions, there are reinforced concrete structures that develop nonnegligible phenomena of durability problems. Most of the durability problems are related to hazardous substances invasion. Both engineering practice and scientific studies have revealed that the transport property of near-surface concrete is a main factor in the durability of concrete structures. Among many transport parameters, the chloride ion diffusion coefficient is the most important one, which provides important information on material design and service life prediction. In this paper, AC impedance spectroscopy technology was employed in the measurement of chloride ion diffusion coefficient. The relationship between mesostructure parameters and chloride ion diffusion coefficient was deduced by introducing a reasonable equivalent circuit model. Taking into account the conductivity difference caused by various cementitious material systems, the diffusion coefficient can be corrected, and a diffusion coefficient determination method based on AC impedance spectroscopy technique was established. For the convenience of application, a relationship between the newly proposed method and a widely recognized standard method was obtained. The proposed method can be applied to laboratory testing and establishes the theoretical basis for field tests.

## 1. Introduction

Durability of concrete structures is one of the unsolved problems in the field of civil engineering and is an international research concern [1]. Durability problems are largely caused by the intrusion of external hazardous substances, which means that the transport property of near-surface concrete is an important aspect that affects durability [2]. A generally accepted fact is that transport property is essentially determined by the mesostructure.

Concrete is a typical porous material. Its pore system includes C-S-H gel pores, capillary pores, microcracks, and micropores. Many ions, such as  $\text{Ca}^{2+}$ ,  $\text{Na}^+$ ,  $\text{K}^+$ ,  $\text{OH}^-$ ,  $\text{Cl}^-$ , and  $\text{SO}_4^{2-}$ , exist, which constitute a complex dynamic electrochemical system. Under AC excitation, the system exhibits a characteristic of a resistor-capacitor combination, and the mesostructure can be studied by using AC impedance spectroscopy.

To separate the desired mesostructure parameters from measured impedance data, researchers have proposed a number of equivalent circuit models [3–8]. Some model

parameters can be obtained through numerical fitting by using measured data and a preset equivalent circuit model. These parameters can be used as quantitative characterization of the mesostructure and hydration degree of cement-based material.

## 2. Concrete Mesostructure and Equivalent Circuit Model

The selected scale should not be small when considering the role of pores in ion diffusion. The C-S-H gel pore does not contribute to permeability. Therefore, only the capillary pores and the pores between C-S-H gels were considered. Basically, three conduction pathways exist for alternating current in concrete, that is, continuous conduction, discontinuous conduction, and the so-called “insulating” conduction paths. The continuous conduction path is a series of connected capillary pores or connected microcracks. If the pore connectivity is cut off by cementitious material or its hydration products, the discontinuous conduction path

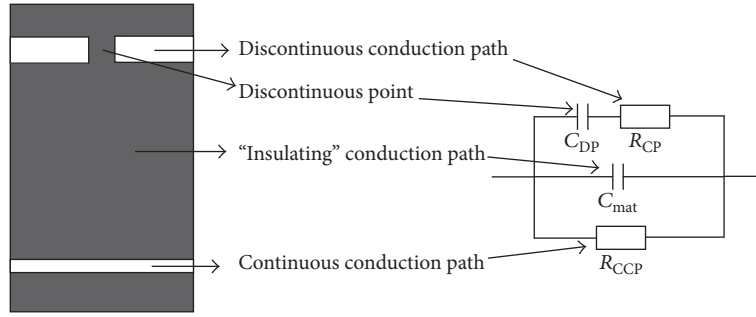


FIGURE 1: Concrete mesostructure for AC conducting.

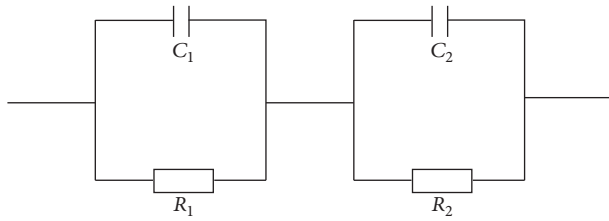


FIGURE 2: Converted equivalent circuit.

is formed. In addition to continuous and discontinuous conduction paths, isolated cementitious material particles and their hydration products or even the entire solid concrete block can also be conductive for alternating current. Based on the above considerations, the concrete mesostructure for AC conducting can be described in Figure 1.

The equivalent circuit model that corresponds to Figure 1 can be expressed as

$$\frac{1}{Z} = \frac{1}{Z_1} + \frac{1}{Z_2} + \frac{1}{Z_3}, \quad (1)$$

where  $Z_1$  is the impedance of the “insulating” conduction path,  $Z_1 = 1/(j\omega C_{mat})$ , and  $C_{mat}$  is the capacitance of the test block;  $Z_2$  is the impedance of the discontinuous conduction path, that is, the sum of the capacitance of the discontinuous point and the resistance of the cut-off continuous conduction path,  $Z_2 = R_{CP} + 1/(j\omega C_{DP})$ ,  $R_{CP}$  is the resistance of the cut-off continuous conduction path, and  $C_{DP}$  is the capacitance of discontinuous point; and  $Z_3$  is the resistance of continuous conduction path,  $Z_3 = R_{CCP}$ .

According to basic circuit theory, the equivalent circuit described in (1) can be converted to a circuit shown in Figure 2.

The conversion relationship of the two equivalent circuits is shown in

$$\begin{aligned} R_{CP} &= (R_0 + R_1) \frac{R_0}{R_1}, \\ R_{CCP} &= R_0 + R_1, \\ C_{DP} &= (C_0 + C_1) \left( \frac{R_1}{R_0 + R_1} \right)^2, \\ C_{mat} &= \frac{C_0 C_1}{C_0 + C_1}. \end{aligned} \quad (2)$$

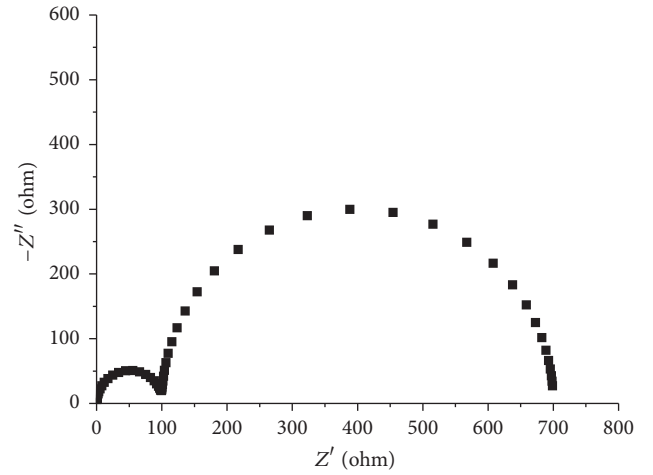


FIGURE 3: Nyquist plot of the equivalent circuit model shown in Figure 2.

A parallel combination of a capacitor and a resistor produces a semicircle in the Nyquist plot. Therefore, two semicircles should appear on the plot of the equivalent circuit shown in Figure 2. Figure 3 shows the relationship between the resistance parameters and the location and size of the semicircles.

Taking into account the second equation in (2), the resistance of the continuous conduction path is the intersection point of the right semicircle with the real axis. However, the Nyquist plot of the measured impedance of cement-based materials does not have two semicircles, but often, only a semicircle appears. Figure 4 is a typical Nyquist plot of concrete; the concrete composition was 23.3 Kg silica fume, 442.7 Kg normal Portland cement, 750 Kg sand, 1125 Kg gravel, 186.4 Kg water, so  $w/b = 0.4$ ; the test age is 28 d.

The left arc does not occur, which indicates that  $C_0$  is much less than  $C_1$ . Thus, the diameter of the left arc is very small with respect to the right arc, and therefore, the left arc is not visible; Cabeza et al. [3, 7] proved this point. Thus, the equivalent circuit can be further simplified as shown in Figure 5, which also shows the corresponding Nyquist plot.

The above discussion indicates that  $R_{CCP}$ , which is the parameter that characterizes the interconnecting porosity that is most relevant to permeability, can be linked with measured impedance spectroscopy.

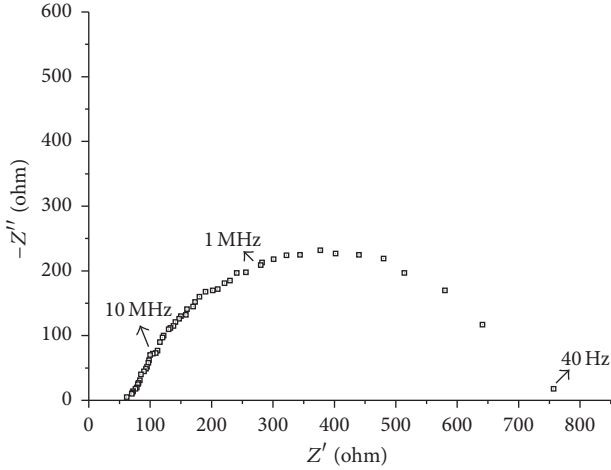
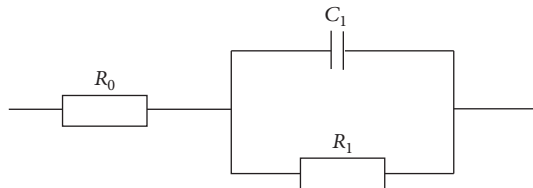
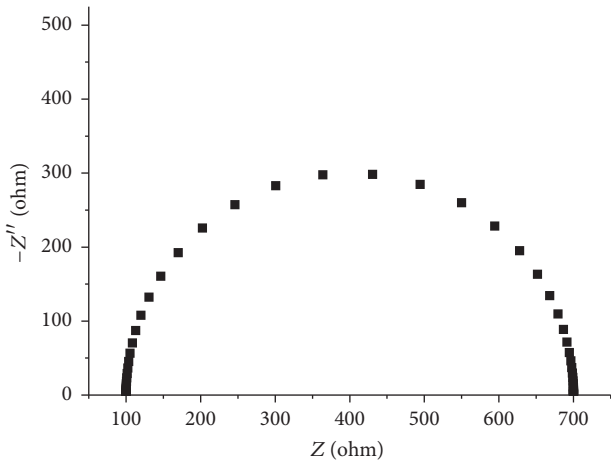


FIGURE 4: High-frequency range Nyquist plot of typical concrete.



(a) Further simplified equivalent circuit



(b) Corresponding Nyquist plot of the simplified equivalent circuit

FIGURE 5: Further simplified equivalent circuit and its Nyquist plot.

### 3. Relationship between AC Impedance Parameters and Permeability

The relationship between AC impedance parameters and permeability can be established in two ways. An empirical relationship between the two can be mathematically regressed by conducting a large number of experiments. However, the disadvantage of this approach is the lack of reliable theoretical basis. Another way to derive some kind of quantitative relationship between the two is through theoretical derivation. This paper adopted the latter approach.

Einstein and Smoluchowski presented an equation on the diffusion of charged particles in solution in 1905 and 1906, respectively; this equation is known as the Einstein-Smoluchowski equation [9], which is shown as follows:

$$D_q = \frac{\mu_q k_B T}{q}, \quad (3)$$

where  $\mu_q$  is the ion mobility ( $\text{m}^2/(\text{V}\cdot\text{s})$ );  $k_B$  is the Boltzmann constant ( $1.38 \cdot 10^{-23} \text{ J/K}$ );  $q$  is the charge carried by ions (C); and  $T$  is the absolute temperature (K). Through the relationship among the Boltzmann constant, the Avogadro constant ( $N_A$ ), the Faraday constant ( $F$ ), the elementary electric charge ( $e$ ), and the universal gas constant ( $R$ ), that is,  $k_B = R/N_A$ ,  $F = eN_A$ , and  $q = z_i e$ , where  $z_i$  is the absolute value of valence, (4) was obtained:

$$\mu_q = \frac{z_q F}{RT} D_q. \quad (4)$$

As for the most significant chloride ion diffusion coefficient  $D_{\text{Cl}^-}$ , which is directly relevant to the durability of reinforced concrete structures, (4) can be specifically written as [9]

$$D_{\text{Cl}^-} = \frac{RT}{z_{\text{Cl}^-} F} \mu_{\text{Cl}^-}. \quad (5)$$

To use (5), a certain concentration of chloride solution must be introduced, and chloride ion mobility must be considered. In AC impedance spectroscopy testing, the measured resistance (or resistivity, conductivity) is a result of the joint action of various ions in a pore solution. To obtain the chloride ion diffusion coefficient, the contribution of chloride ions to the conductance needs to be separated from the total conductance. To achieve this, a 1 mol/L NaCl solution was used to saturate a concrete test block to weaken the influence of other existing ions. Thus, the conductivity expression,  $\sigma = F \sum z_i \mu_i C_i$ , where  $C_i$  is the concentration and  $z_i$  is the activity coefficient ( $z_i = 1$ ), can be written as

$$\sigma = F * (\mu_{\text{Cl}^-} C_{\text{Cl}^-} + \mu_{\text{Na}^+} C_{\text{Na}^+}). \quad (6)$$

To further differentiate the contribution of chloride ions and sodium ions to the conductance, the contribution percentage of chloride ions is 61%, which is close to that of an infinitely diluted sodium chloride solution (60.4%), under the conditions of 25°C and 1 mol/L concentration; this information was verified by consulting a chemistry handbook. Combining (5) and (6) obtains

$$D_{\text{Cl}^-} = \frac{\sigma RT}{1.64 F^2 C_{\text{Cl}^-}}. \quad (7)$$

Taking into account the relationship between resistance ( $\rho$ ), conductivity ( $\sigma$ ), and cell constant ( $a = l/A$ , where  $l$  is the thickness of the test block and  $A$  is the contact area of the electrode and the test block), (8) is obtained:

$$\sigma = \frac{1}{\rho} = \frac{a}{R_{\text{CCP}}}. \quad (8)$$

TABLE 1: Chemical compositions of cement and mineral admixtures (% by weight).

Composition	SiO <sub>2</sub>	Al <sub>2</sub> O <sub>3</sub>	Fe <sub>2</sub> O <sub>3</sub>	CaO	MgO	SO <sub>3</sub>	Na <sub>2</sub> O	K <sub>2</sub> O
Cement	21.09	4.34	2.81	62.5	1.81	2.87	0.15	0.62
Slag	34.55	14.36	0.45	33.94	11.16	1.95	0.28	0.35
Fly ash	57.57	21.91	7.72	3.87	1.68	0.41	1.54	2.51
Silica fume	92.63	1.05	1.17	0.34	0.73	0.30	0.22	0.93

w: mass fraction.

Therefore, the relationship between chloride ion diffusion coefficient and the interconnecting pore resistivity can be expressed as

$$D_{Cl^-} = \frac{aRT}{1.64F^2 R_{CCP} C_{Cl^-}} \quad (9)$$

In (9), the influences of other ions on chloride ion diffusion coefficient determination have been largely removed. To further eliminate these effects, some pastes (water-binder ratio = 10) were prepared, and the cementitious material that was used is as follows: fly ash + Portland cement (cement replacement level is 20%, 40%, and 60%, resp.), slag + Portland cement (cement replacement level is 25%, 50%, and 75%, resp.), and silicon fume + Portland cement (cement replacement level is 5%, 10%, and 15%, resp.). The chemical compositions of cement and mineral admixtures are listed in Table 1.

A conductivity cell with a length of 6.92 cm and an electrode area of 9.62 cm<sup>2</sup> was also made. This experiment aims to investigate the influence of different pore solutions caused by different cementitious materials used on conductance. Strictly speaking, to carry out pore solution conductivity tests, the pore solution should be squeezed out of the concrete block. However, given the complexity of the required equipment and the limited amount of the extracted pore solution, this research adopted the simulation approach by measuring high water-binder ratio paste that was prepared by using various cementitious materials. Before the age of 7 d, the paste will not solidify by shaking the container several times every day. The paste solution was shaken for 5 minutes the day before the test and then left undisturbed for 24 h. Then, the upper solution was taken and injected into the conductivity testing cell. The frequency of the alternating current is 2000 Hz, and the test ages are 28 and 90 d. Figure 6 shows the test results.

Figure 6 shows that the addition of mineral admixtures reduces the concrete pore solution conductivity. As generally accepted, the most important factor that influences permeability is connected porosity rather than pore solution conductivity. To further eliminate the influence of other ions on AC impedance testing for chloride ion diffusion coefficient determination, a correction factor can be introduced. To perform this step, the correction factor of ordinary Portland cement concrete can be set as a benchmark. For concrete that uses other cementitious materials, the correction factor may be determined by interpolation in accordance with Table 2.

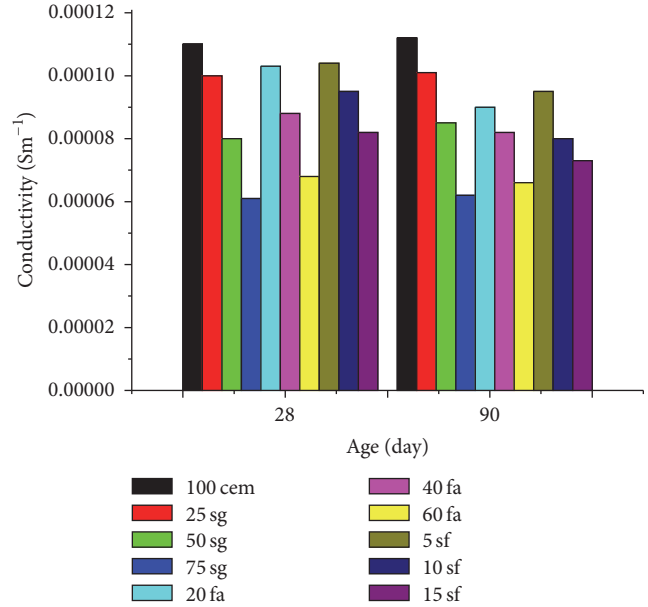


FIGURE 6: Conductivity value of different paste solutions.

TABLE 2: Diffusion coefficient correction factor.

Types of mineral admixtures	(Replacement ratio)/diffusion coefficient correction factor		
Fly ash	(20%) 1.2	(40%) 1.3	(60%) 1.7
Slag	(25%) 1.1	(50%) 1.3	(75%) 1.8
Silicon fume	(5%) 1.1	(10%) 1.3	(15%) 1.4

## 4. Experimental Studies

Table 3 shows the concrete mix that was used in the experiment.

First,  $\Phi 100$  mm  $\times$  300 mm cylinder test blocks were prepared for the experiment. Steel mold was removed one day after pouring, and then concrete cylinders were cured for 28 or 90 d before being cut into  $\Phi 100$  mm  $\times$  50 mm blocks for vacuum saturation (using 1 mol/L NaCl solution, the saturating regime is the same as that of ASTM C1202).

Then, a 100 mm  $\times$  100 mm stainless steel plate was adopted as the electrode. To ensure close contact between the electrodes and the concrete surface, soaked filter papers (using 1 mol/L NaOH solution) were introduced. Prepressure was applied to the electrodes by using screw caps. Agilent 4294A precision impedance analyzer was employed (see Figure 10), and the test frequency is 40 Hz to 40 MHz. Five

TABLE 3: Concrete mix.

Specimen number	Materials used (unit: kg/m <sup>3</sup> )						
	Cement	Fly ash	Slag	Silicon fume	Water	Fine aggr.	Coarse aggr.
C0	466.0	0	0	0	186.0	750.0	1125.0
FA1	372.8	92.3	0	0	186.0	735.7	1103.6
FA2	276.6	186.4	0	0	186.0	720.5	1080.9
FA3	186.4	276.6	0	0	186.0	705.3	1058.0
GS1	349.5	0	116.5	0	186.0	747.6	1121.4
GS2	233.0	0	233.0	0	186.0	744.2	1116.3
GS3	116.5	0	349.5	0	186.0	740.8	1111.2
SF1	442.7	0	0	23.3	186.0	747.6	1121.4
SF2	419.4	0	0	46.6	186.0	744.2	1116.3
SF3	396.1	0	0	69.9	186.0	740.8	1111.2
JH1	266.0	114.0	0	0	144.0	760.8	1141.2
JH2	190.0	95.0	95.0	0	144.0	761.2	1141.8
JH3	195.0	130.0	65.0	0	144.0	752.8	1129.2



FIGURE 7: Concrete blocks for the impedance test.

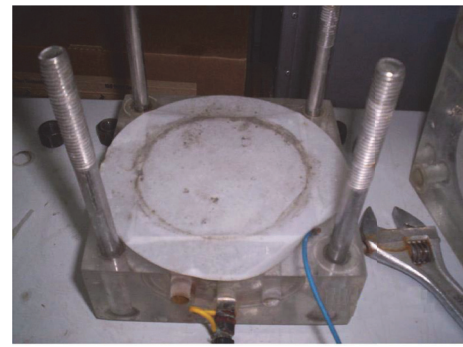


FIGURE 9: Electrode mounting.

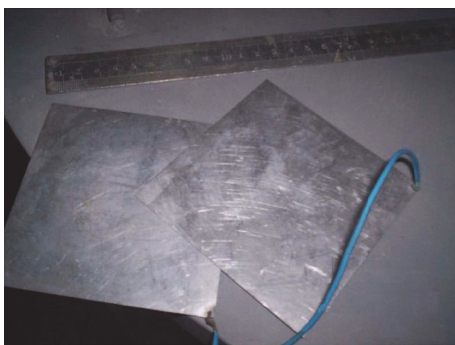


FIGURE 8: Stainless steel electrodes.



FIGURE 10: Impedance tester.

test points were measured for each order of magnitude. The test block, electrode, electrode installation, and impedance analyzer are shown in Figures 7–9, respectively.

Figure 11 shows the AC impedance spectroscopy test result of the C0 test block (90 d).

To verify the validity of the measured impedance data, a validation check by using linear Kramers–Kronig test [10]

was conducted. Figure 12 shows the validation results of typical ordinary Portland cement concrete, cement + fly ash composite binder concrete, cement + slag composite binder concrete, and cement + silica fume composite binder concrete.

In Figure 12, the abscissa axis represents the frequency, and the ordinate axis on both sides represents the residuals

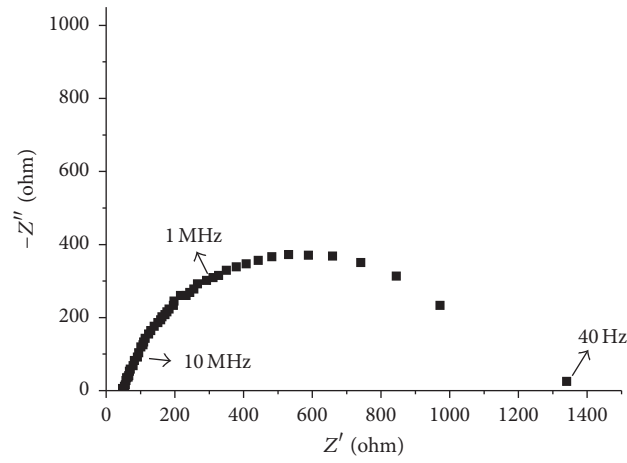


FIGURE 11: Nyquist plot of spectroscopy test results of specimen number C0.

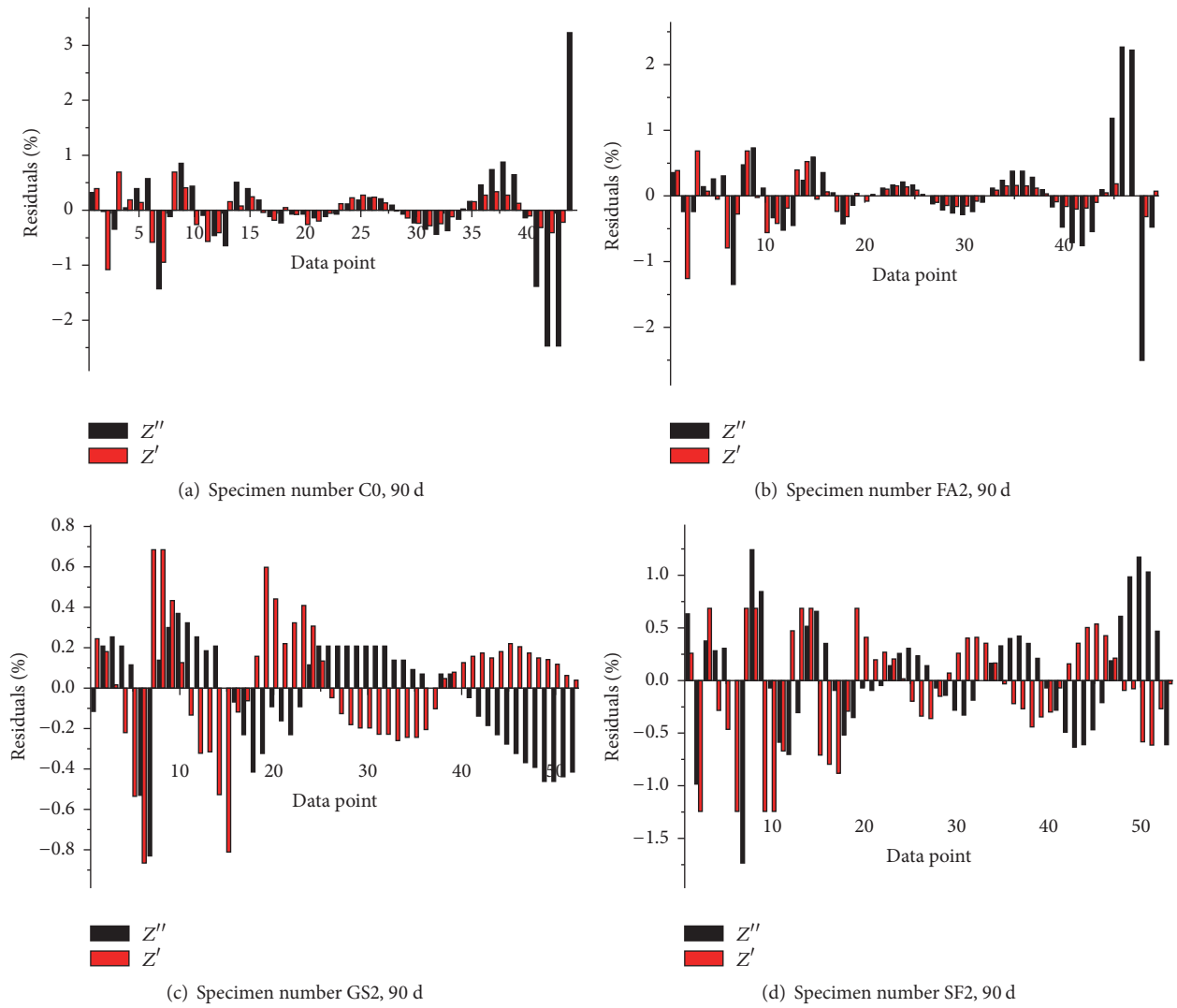


FIGURE 12: Validation results.

of Voigt model fitting. Equation (10) is used to calculate the residuals:

$$\begin{aligned} \text{Residuals (Re}Z) &= \frac{(Z_{\text{Re}} - Z_{\text{Re-cal}})^2}{Z_{\text{Re}}^2}, \\ \text{Residuals (Im}Z) &= \frac{(Z_{\text{Im}} - Z_{\text{Im-cal}})^2}{Z_{\text{Im}}^2}, \end{aligned} \quad (10)$$

where  $Z_{\text{Re}}$  and  $Z_{\text{Im}}$  are real part and the imaginary part of the measured impedance, respectively, and  $Z_{\text{Re-cal}}$  and  $Z_{\text{Im-cal}}$  are the fitted values obtained by using the Voigt model. Small residuals correspond to better validity.

Only measured data that passed the Kramers–Kronig test can be used for further numerical fitting. Figure 12 shows that the obtained impedance data shows good validity, which can be attributed to the measures employed in this section. Moreover, the repeatability of the test data is good because of reliable close contact between the test block and the electrodes.

Parameters  $R_0$ ,  $R_1$ , and  $C_1$  can be obtained through numerical fitting of the measured impedance data and the preset equivalent circuit shown in Figure 5. The chloride ion diffusion coefficient can be calculated by using  $R_{\text{CCP}} = R_0 + R_1$  and (9).

The method of determining chloride ion diffusion coefficient based on the AC impedance technique is performed as follows:

- (1) Prepare  $\Phi 100 \text{ mm} \times 50 \text{ mm}$  specimens and conduct vacuum  $\text{Cl}^-$  saturating using 1 mol/L NaCl solution (the saturating regime is the same as that of ASTM C1202).
- (2) Carry out AC impedance testing to obtain impedance spectroscopy data.
- (3) Perform data validation.
- (4) Obtain  $R_{\text{CCP}}$  from equivalent circuit fitting.
- (5) Calculate chloride ion diffusion coefficient using (9).
- (6) Modify the diffusion coefficient according to the cementitious material that was used.

The rapid chloride permeability test ASTM C1202 has been adopted as national standard by many countries, including China, the United States, and Canada. The ASTM C1202 method specifies the rating of chloride permeability of concrete based on the charge passed through the specimen during 6 h of testing period. ASTM C1202 tests that use the same concrete blocks were conducted to perform a comparison. Figure 13 shows the relationship between chloride ion diffusion coefficients obtained from impedance-based technology and 6 h electric flux. A linear correlation ( $Q_{\text{C1202}} = 930 \times D_{\text{Cl}^-}$ ) between the rapid chloride permeability test and the proposed method was obtained, with a correlation coefficient of 0.9; see Figure 13 for details.

As can be seen from Figure 13, some data points deviate from the straight line. As reported by Shi [11], the ASTM C1202 method is virtually a measurement of electrical conductivity of concrete, which depends on both the pore

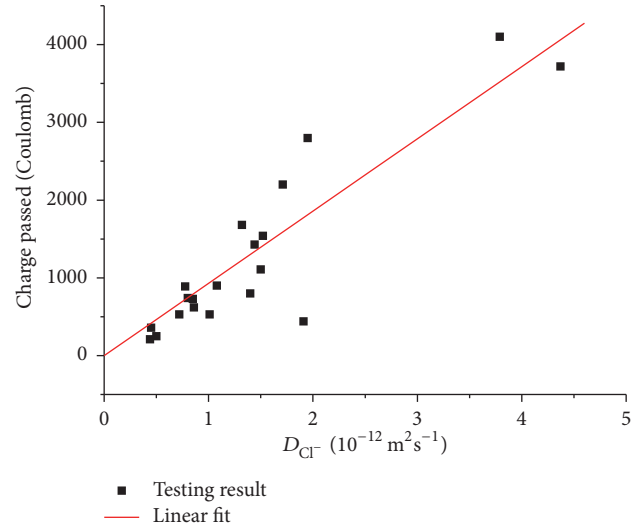


FIGURE 13: Relationship between chloride ion diffusion coefficient using ACIS and 6 h electric flux from ASTM C1202 tests.

structure characteristics and pore solution chemistry of concrete. Supplementary cementing materials such as silica fume, fly ash, and ground blast furnace slag may have a significant effect on the chemistry or electrical conductivity of pore solution, depending on the alkali content of the supplementary cementing material, replacement level, and age, which has little to do with the chloride permeability. ASTM C1202 method is susceptible to pore solution conductance. However, the proposed method eliminates the effect of pore solution conductivity on permeability by using a carefully designed technique. This effect may be an important reason for the moderate correlation between the two methods.

## 5. Conclusions

(1) High-frequency AC impedance spectroscopy can reflect the mesostructural properties of materials, which enables us to indirectly study the permeability of concrete. An equivalent circuit model with a clear physical meaning was adopted through an investigation of AC conduction paths in concrete. Through numerical fitting of the Nyquist plot of the measured impedance spectroscopy and a preset model, a parameter that characterizes diffusion resistance that depends on the interconnected porosity and pore solution conductivity was obtained. Based on the Einstein–Smoluchowski equation, the chloride ion diffusion coefficient was derived, and the proposed formula was modified to eliminate the influence of pore solution conductivity on diffusion coefficient measurement. Then, an accurate formula that reflects chloride ion diffusion resistance was obtained.

(2) With test block size, specimen pretreatment, impedance test parameters, equivalent circuit selection, and diffusion coefficient formula modification taken into consideration, a method of determining the chloride ion diffusion coefficient based on AC impedance spectroscopy was established. In addition, the test procedure was summarized for practical purposes.

(3) The relationship between the proposed method and the traditional ASTM C1202 method was established. Results showed that a certain but not very high degree of linear correlation exists, which can be attributed to the fact that ASTM C1202 method is essentially a conductance method influenced by pore solution conductivity, whereas pore solution conductivity has little effect compared with interconnected porosity on chloride ion diffusion behavior in concrete.

### Competing Interests

The authors declare that there is no conflict of interests regarding the publication of this paper.

### Acknowledgments

The authors acknowledge the support from National Natural Science Foundation of China (Grant nos. 51408379 and 51508350) and Natural Science Foundation of Hebei, China (Grant no. E2013210125).

### References

- [1] L. Kong and Y. Du, "Effect of lightweight aggregate and the interfacial transition zone on the durability of concrete based on grey correlation," *Indian Journal of Engineering and Materials Sciences*, vol. 22, no. 1, pp. 111–119, 2015.
- [2] A. E. Long, G. D. Henderson, and F. R. Montgomery, "Why assess the properties of near-surface concrete?" *Construction and Building Materials*, vol. 15, no. 2-3, pp. 65–79, 2001.
- [3] M. Cabeza, M. Keddad, X. R. Nóvoa, I. Sánchez, and H. Takenouti, "Impedance spectroscopy to characterize the pore structure during the hardening process of Portland cement paste," *Electrochimica Acta*, vol. 51, no. 8-9, pp. 1831–1841, 2006.
- [4] G. Dotelli and C. M. Mari, "The evolution of cement paste hydration process by impedance spectroscopy," *Materials Science and Engineering A*, vol. 303, no. 1-2, pp. 54–59, 2001.
- [5] M. Cabeza, P. Merino, X. R. Nóvoa, and I. Sánchez, "Electrical effects generated by mechanical loading of hardened Portland cement paste," *Cement and Concrete Composites*, vol. 25, no. 3, pp. 351–356, 2003.
- [6] P. Gu, P. Xie, J. J. Beaudoin, and R. Brousseau, "A.C. impedance spectroscopy (I): a new equivalent circuit model for hydrated portland cement paste," *Cement and Concrete Research*, vol. 22, no. 5, pp. 833–840, 1992.
- [7] G. Song, "Equivalent circuit model for AC electrochemical impedance spectroscopy of concrete," *Cement and Concrete Research*, vol. 30, no. 11, pp. 1723–1730, 2000.
- [8] M. Shi, Z. Chen, and J. Sun, "Determination of chloride diffusivity in concrete by AC impedance spectroscopy," *Cement and Concrete Research*, vol. 29, no. 7, pp. 1111–1115, 1999.
- [9] C. Andrade, "Calculation of chloride diffusion coefficients in concrete from ionic migration measurements," *Cement and Concrete Research*, vol. 23, no. 3, pp. 724–742, 1993.
- [10] J. M. Esteban and M. E. Orazem, "On the application of the Kramers-Kronig relations to evaluate the consistency of electrochemical impedance data," *Journal of the Electrochemical Society*, vol. 138, no. 1, pp. 67–76, 1991.
- [11] C. Shi, "Effect of mixing proportions of concrete on its electrical conductivity and the rapid chloride permeability test

(ASTM C1202 or ASSHTO T277) results," *Cement and Concrete Research*, vol. 34, no. 3, pp. 537–545, 2004.

## Research Article

# The Mechanical Properties of the Concrete Using Metakaolin Additive and Polymer Admixture

Adel Al Menhosh,<sup>1</sup> Yan Wang,<sup>2</sup> and Yu Wang<sup>1</sup>

<sup>1</sup>School of Computing, Science & Engineering, University of Salford, Manchester M5 4WT, UK

<sup>2</sup>School of Civil Engineering, Chongqing Jiaotong University, Chongqing 400074, China

Correspondence should be addressed to Yu Wang; [y.wang@salford.ac.uk](mailto:y.wang@salford.ac.uk)

Received 6 June 2016; Accepted 11 July 2016

Academic Editor: Peng Zhang

Copyright © 2016 Adel Al Menhosh et al. This is an open access article distributed under the Creative Commons Attribution License, which permits unrestricted use, distribution, and reproduction in any medium, provided the original work is properly cited.

Environmentally friendly and high performance concrete is very important for the applications in sewage and water treatment industry. Using mineral additives such as fly ash and silica fume has been proven to be an effective approach to improve concrete properties. This paper reports a study of the effect of using both polymer and metakaolin additives together on the mechanical and durability properties of concrete. Different proportions of the combination using two different polymers, metakaolin, and recycled fiber reinforcement have been studied. The effects of water-to-cement ratio and the curing methods have also been compared. At last an optimized mixture and curing method has been suggested.

## 1. Introduction

Using mineral additives such as fly ash and silica fume has been proven to be an effective approach to improving concrete properties. With the increasing of the environmental concern, in recent years [1], the use of metakaolin (MK) as an optional additive has also raised more and more interests [2]. As a supplementary cementitious material MK has the expected pozzolanic nature activated by tricalcium silicate (C3S) and tricalcium aluminate (C3A) [3]. When used as a partial replacement for cement, MK reacts with portlandite ( $\text{Ca}(\text{OH})_2$ ) to generate additional CSH gel which results in the increase of strength. Previous work by Khatib et al. [4] showed that the 20% replacement of cement using MK had resulted in a substantial 50% increase of the compressive strength of mortar. However, with over 30% replacement of cement by MK, the compressive strength started to decrease. It has also been shown that the sample containing 10% MK replacement displayed the best performance in terms of ultrasonic test. Justice [5] compared the effects of the use of two different types of MK on concrete workability and setting time. It was found that MK caused a considerable reduction in workability and reduced the setting time of

cement paste by 35–50%. The study also showed that the use of MK had increased the compressive strength, splitting tensile strength, flexural strength, and the elastic modulus of concrete samples. Guneyisi et al. [6] compared the effects of the use of silica fume and MK on the water sorptivity of concrete. It was observed that the water sorptivity decreases more when using MK additive than when using silica fume.

In concrete practice, polymers have been also commonly used as additives to improve concrete durability because of its effect on reducing water absorption. Styrene butadiene rubber (SBR) and poly vinyl acetate (PVA) are two polymers commonly used in concrete with the effect on reducing the pore spaces and connection [7]. Previous work [8] has found that while it increases the strength and decreases the water permeability, SBR can increase the workability of concrete as well. The work by Jamshidi et al. [9] also showed that a polymer admixture of the SBR, acrylic, and PVA generated a decrease in water permeability of the concretes. A work by W. J. Lewis and G. Lewis [10] showed that the workability of SBR modified concretes was much higher than that of normal concrete and increases with the increase of polymer content. However, the workable time was greatly reduced when compared with normal unmodified concrete.

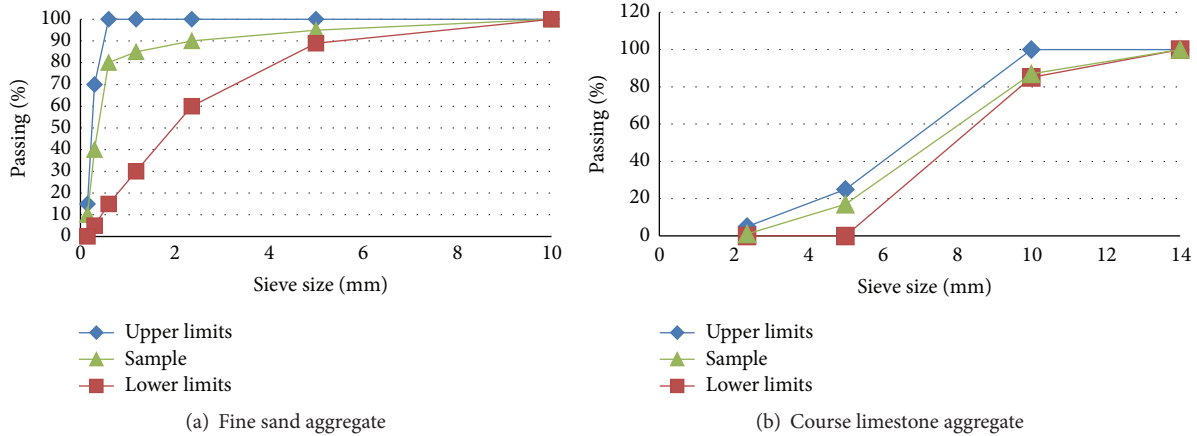


FIGURE 1: Particle size distribution.

Wang et al. [11] studied the physical and mechanical properties of SBR modified cement mortars using different polymer/cement ratio (p/c) and a constant water/cement ratio of 0.4. They also compared two curing methods, that is, wet cure for 2, 6, or 27 days by being immersed in 20°C water and mixed cure for 6 days by being immersed in 20°C water followed by 21 days at 20°C and 70% relative humidity (RH). The results showed that the mixed cure produced an improvement on the mortar properties. Ganiron Jr. [12] ever investigated the influence of polymer fiber on the strength of concrete. They added two kinds of polymer fibers, that is, polyvinyl alcohol and polyvinyl acetate, into concrete mixes. It was found that the polymer modified concrete of 2% p/c showed the highest compressive strength and that of 6% p/c displayed a similar result to that of the conventional concrete.

## 2. Experimental Investigation

This research aims to investigate the combined effect of using both MK and polymer together on the improvement of the concrete mechanical and durability properties. At first, control sample was made using a mixture of Portland cement, sand, and gravels. Second, modified concrete specimens were made by adding two types of polymer additives, that is, SBR and PVA, and partially replacing the cement using MK. Different water cement ratios were used for all of these mixtures. In addition, plastic and glass fiber made of recycled materials were used to reinforce the concrete mixtures. Experimental tests of the concrete mixtures after different setting time have been carried for mechanical properties, including compressive strength, splitting tensile strength, flexural strength, and, the durability related property, water absorption. The effects of using different curing methods have also been compared.

**2.1. Component Materials and Mixtures.** Portland limestone cement, the CEM II/A-LL (BS EN 197-1:2011), was used in the experiment. The cement properties have been listed in Table 1. The fine aggregate used sand, while the coarse aggregate was crashed limestone gravel with maximum

TABLE 1: Properties of the cement used.

Particulars	Unit	Value	Standard
Setting time—initial	Minutes	150	80–200
Compressive strength			
2 days	N/mm <sup>2</sup>	17	16–26
7 days	N/mm <sup>2</sup>	29	27–37
28 days	N/mm <sup>2</sup>	40	37–47

TABLE 2: Metakaolin properties.

Particulars	Value
Colour	White
ISO brightness	>82.5
−2 μm (mass%)	>60
+325 mesh (mass%)	<0.03
Moisture (mass%)	<1.0
Aerated powder density (kg/m <sup>3</sup> )	320
Tapped powder density (kg/m <sup>3</sup> )	620
Surface area (m <sup>2</sup> /g)	14
Pozzolanic reactivity (mg Ca(OH) <sub>2</sub> /g)	>950

size of 10 mm. The specific gravity of the limestone aggregate is 2.49. Their particle size distribution followed BS 882:1992 and BS 812:1992. Figure 1 shows the sieve analysis results. A premium metakaolin produced by Whitchem Ltd. (<http://whitchem.co.uk/>) was used in this study. Its properties have been shown in Table 2. Both SBR and PVA were used as polymer additives. Tables 3 and 4 have listed their properties, respectively. Table 5 lists the SBR and PVA composition in the polymer mixture studied. Alkali resistant glass fiber (GF) and a recycled polypropylene plastic fiber (PF) were also used in the study.

The control concrete mixture took the proportion of cement/sand/gravel as 1/1.5/3. The modified mixtures were made based on the control mix with the replacement of the cement using MK and a polymer mixture. The MK took 0, 10, 15, and 20% of the weight of cement, respectively, while the polymer mixture took 0, 2.5, 5, and 7.5%, respectively.

TABLE 3: Styrene butadiene rubber properties.

Particulars	Value
Brand	Cementone
Colour	White
Model name	SBR
Product type	Admixture
Resistance type	Water, chemical & abrasion resistance

TABLE 4: Polyvinyl acetate properties.

Particulars	Values
Typical performance data (approx.) application temperature	5°C–25°C.
Wet grab	10 minutes approx. at 15°C.
Tack development	10–90 minutes at 15°C.
Bonding	Maximum strength is attained in 24 hours.
Colour	White.
Form	Liquid.
Specific gravity	1.1 approx.
Composition	Polyvinyl acetate emulsion.

TABLE 5: The polymer mixture used in this study.

	Polymer composition		MK (% cement)
	SBR %	PVA %	
Study for optimizing the polymer mixture composition	0	0	15
	100	0	15
	80	20	15
	60	40	15
	50	50	15
	40	60	15
	20	80	15
	0	100	15
	5	15	15

TABLE 6: The mixtures proportion used in this study.

	Polymer (% cement)	MK (% cement)	Fiber (% cement)
Study for optimizing the polymer and MK combination	0/2.5/5/7.5	0	
	0/2.5/5/7.5	10	
	0/2.5/5/7.5	15	
	0/2.5/5/7.5	20	
Study for optimizing fiber content	0/5	0	0/5
	0/5	15	0/5

The added fiber took the 0, 2.5, and 5% of the cement weight of the control mixture. The mixtures are listed in Table 6. The effects of three water-to-cement ratios, 0.35, 0.4, and 0.45, were studied based on the control mix. The effects of three curing methods, the wet, dry, and moist, were also compared.

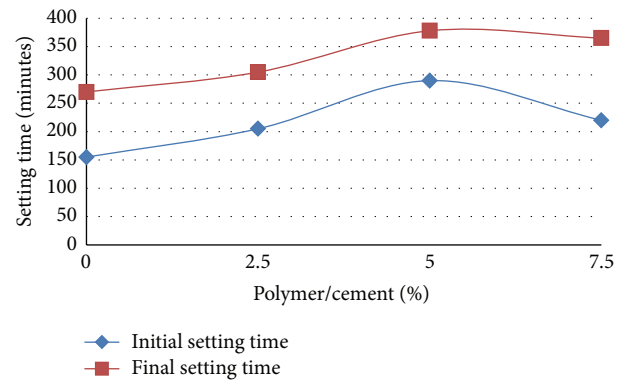


FIGURE 2: The setting time of polymer modified cement paste with 0% MK.

## 2.2. Experimental Tests

**Setting Time.** The initial and final setting time tests were conducted on cement pastes for a standard consistency. The consistence was measured using Vicat apparatus according to ASTM C187-86:1986. The sitting time was measured according to the penetration of a needle gauge according to ASTM C 191-82:1986

**Slump Test.** The workability of mixtures was tested following BS EN 12350-2:2009.

**Compressive Strength.** Compressive test was conducted using cubic samples with a dimension of 100 mm × 100 mm × 100 mm according to BS 1881 part 116:1983.

**Splitting Tensile Strength.** Splitting tensile test was conducted using cylindrical samples with a dimension of 150 mm (D) by 300 mm (L) according to BS 1881 part 117:1983.

**Flexural Strength.** Flexural test was conducted using prismatic samples with a dimension of 100 mm (D) by 100 mm (H) by 500 mm (L) by applying a concentrated load at the centre according to ASTM C293-02.

**Water Absorption.** Water adsorption test was conducted using cubic samples with the dimension the same as that used for compressive test according to BS 1881: part 122:2011.

## 3. Results and Discussions

Figures 2–4 have showed the results of the initial and final setting times. It can be seen that polymer has a significant effect on delaying setting time. The effect increases with the increase of polymer content. It also can be seen that the setting time accelerates with the increase of MK content. With the addition of both polymer and MK, it has been found that the mixture of 15% MK displayed a relatively stable setting time at varied polymer contents.

Figure 5 shows that the workability increases with the increase of polymer content but decreases with the increase of MK, and similar results were observed for all w/c ratios.

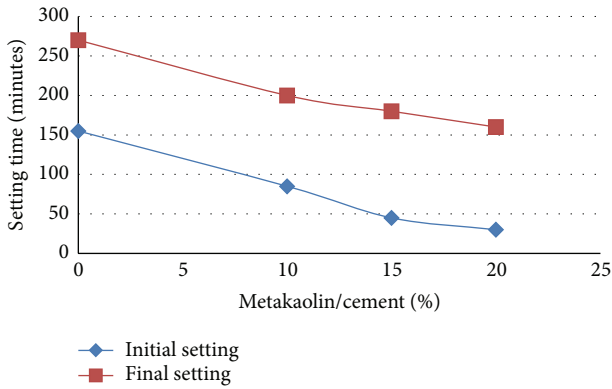


FIGURE 3: The setting time of MK modified cement paste with 0% polymer.

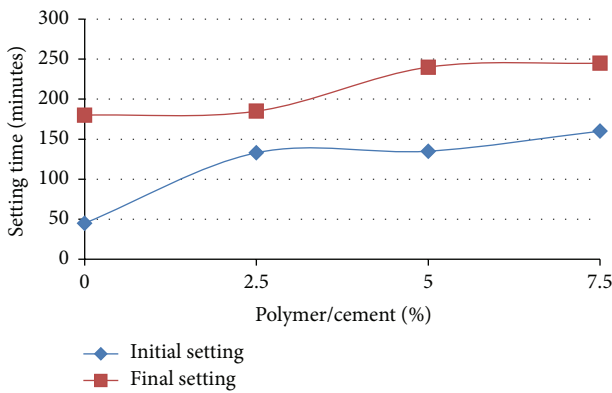


FIGURE 4: The setting time of polymer modified cement paste with 15% MK.

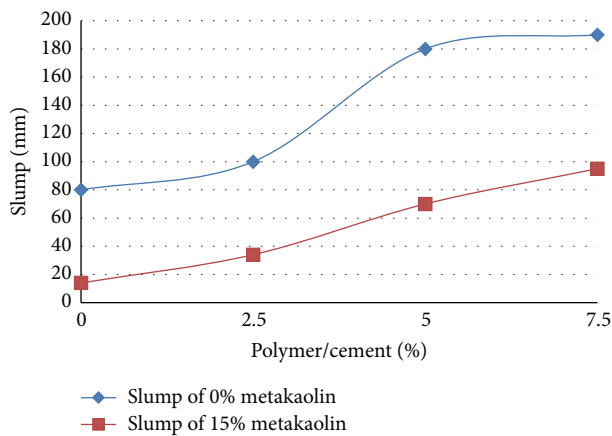


FIGURE 5: Effect of polymer and MK on workability for modified concrete with w/c 45%.

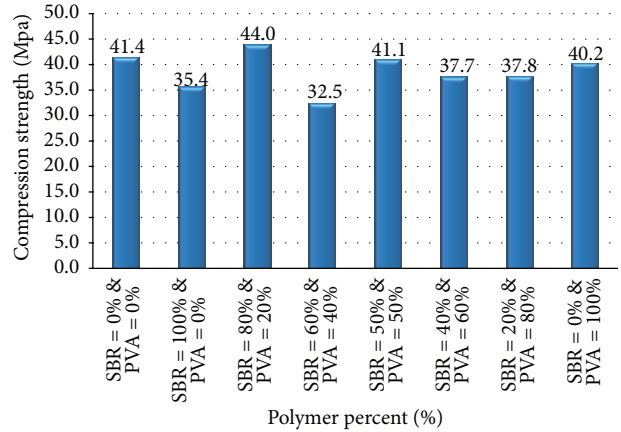


FIGURE 6: 28-day compressive strength of the concrete containing 5% polymer and 15% MK.

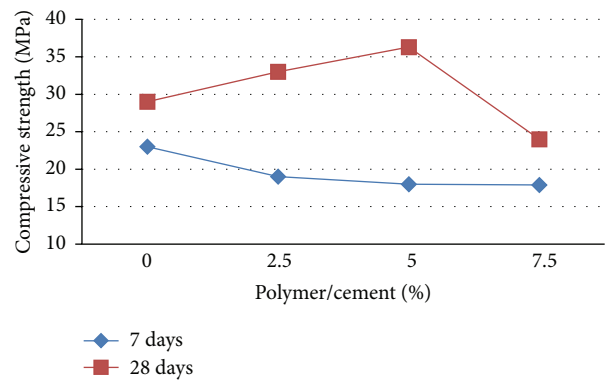


FIGURE 7: The compressive strength at different polymer contents with 0% m/c and w/c = 45%.

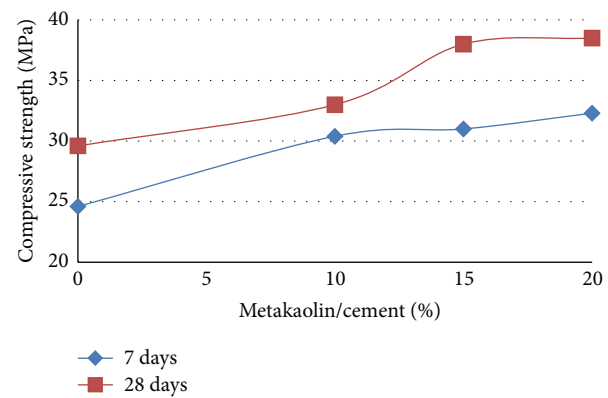


FIGURE 8: The compressive strength at different MK contents and 0% polymer.

The effect of the polymer of different composition of the SBR and PVA was studied. Figure 6 shows that the polymer consisting of 80% SBR and 20% PVA displays the highest compressive strength. Figures 7–9 show the effect of varied contents of the polymer, consisting of 80% SBR and 20% PVA, and MK on the compressive strength. It

can be seen that the mixture of 5% polymer and 15% MK displayed the highest compressive strength. It also can be seen that while the 28-day compressive strength decreases when polymer content exceeds 5%, however, both 7-day and 28-day compressive strengths increase with the increase of MK. Figures 10 and 11 show the effect of different curing methods

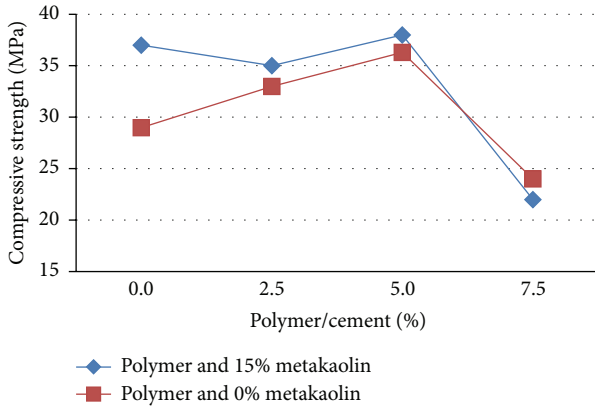


FIGURE 9: The compressive strength at different polymer contents at age of 28 days.

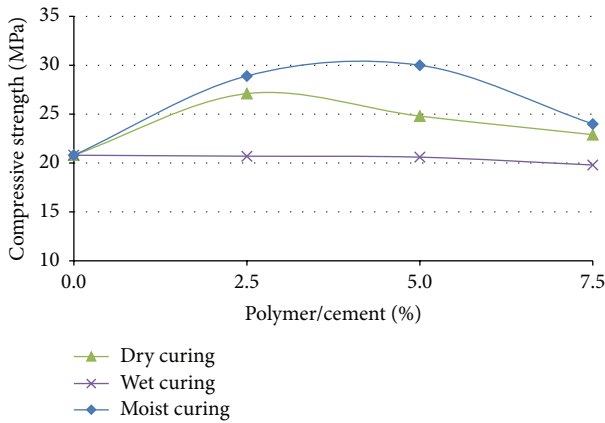


FIGURE 10: The effect of curing methods on the compressive strength at different polymer contents and 0% MK at age of 28 days.

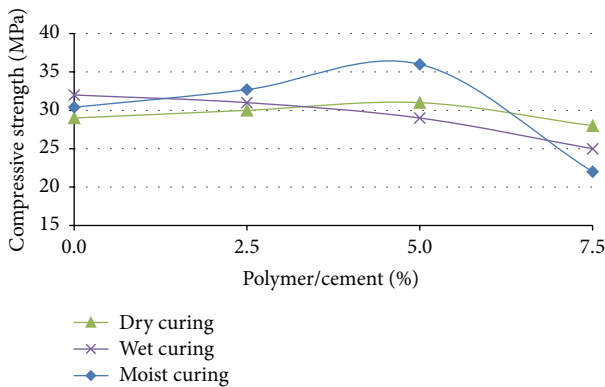


FIGURE 11: The effect of curing methods on the compressive strength at different polymer contents and 15% MK at age of 28 days.

on the compressive strength of the modified concretes. It can be seen that the moist curing generated the best results. Figure 12 shows the results using different types of coarse aggregates. It can be seen that limestone aggregate is better than normal aggregate.

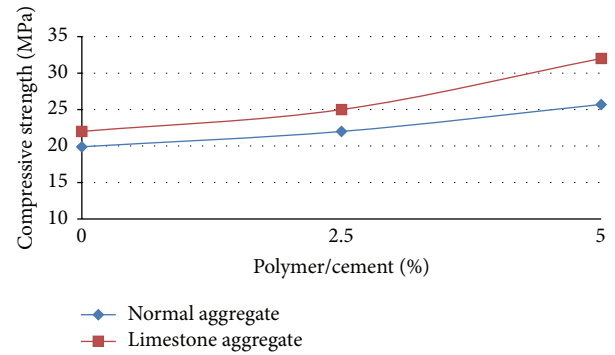


FIGURE 12: The effect of the aggregates type on the compressive strength at different polymer content and 0% MK at age of 28 days.

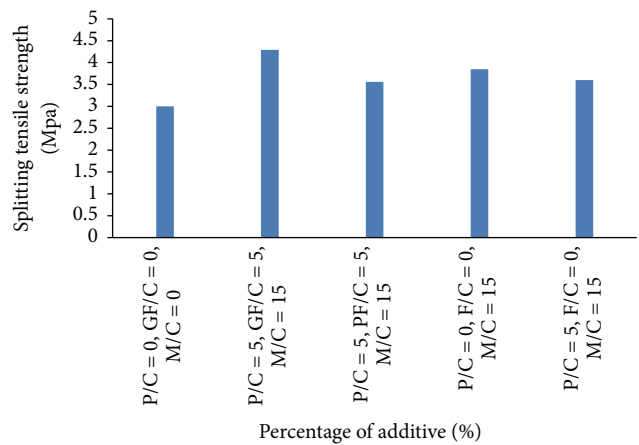


FIGURE 13: Splitting tensile strength at age of 28 days.

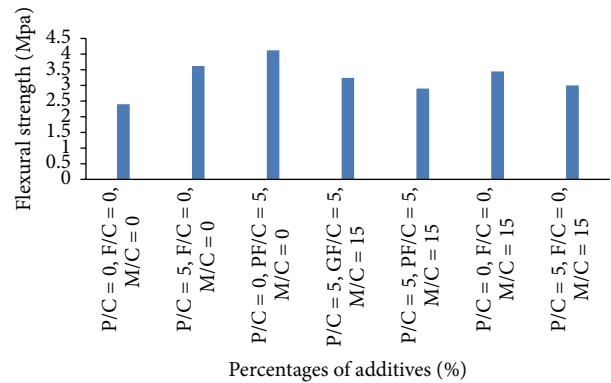


FIGURE 14: Flexural strength at age of 28 days.

Figure 13 shows the effect of plastic fiber (PF) and glass fiber (GF) on the splitting tensile strength. It can be seen that using glass fiber for reinforcement produced the highest splitting strength.

Figure 14 shows the effect of fiber reinforcement on flexural strength. It can be shown that the flexural strength has been improved with the fiber reinforcement. The use of glass fiber (GF) and polymer presents the best flexural strength. It also can be seen that using MK will enhance

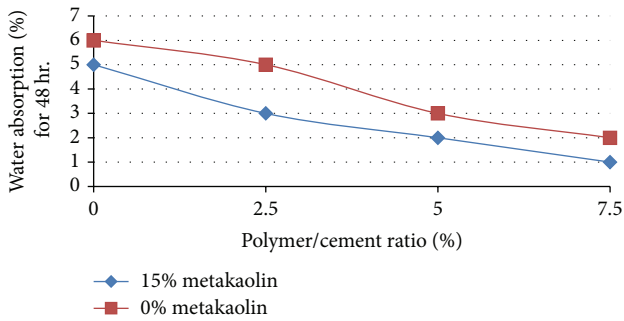


FIGURE 15: Water absorption at different polymer contents.

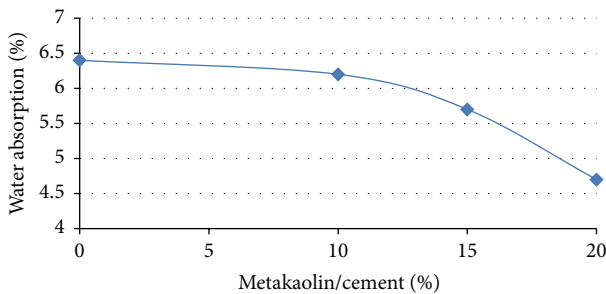


FIGURE 16: Water absorption at different MK contents and 0% polymer.

the flexural strength as well. However, using both MK and polymer together, the mixture shows a decrease in flexural strength. To explain this, further study is needed.

Figures 15 and 16 show the total adsorbed water percentage in terms of the weight of dry samples. It can be seen that, with the increase of polymer and MK content, the water absorption reduces remarkably. This might be due to a reduction in porosity as a result of the added polymer latex and the pozzolanic reaction of metakaolin.

#### 4. Conclusions

The following conclusions can be drawn from the reported experimental study:

- (i) Metakaolin will accelerate the setting time of cement pastes but reduce the workability of concrete. However, polymer has an inverse influence on the two properties.
- (ii) The polymer composition of 80% SBR and 20% PVA shows an optimized result when it works together with MK.
- (iii) The appropriate water/cement ratio is 0.45 for the concrete using polymer and metakaolin additives.
- (iv) The addition of 5% optimized polymer and 15% cement replacement using metakaolin generates an optimized concrete mixture for both strength and durability.
- (v) For the optimized polymer and MK mixture, the 5%, in terms of the cement weight, addition of the plastic

and glass fibers can effectively improve the tensile strength.

#### Competing Interests

The authors declare that they have no competing interests.

#### Acknowledgments

This work is a part of an ongoing Ph.D. project funded by the Iraqi Ministry of Higher Education and Scientific Research Scholarship Program.

#### References

- [1] K. Srinivasu, M. L. N. K. Sai, and N. V. S. Kumar, "A review on use of metakaolin in cement mortar and concrete," *International Journal of Innovative Research in Science, Engineering and Technology*, vol. 3, no. 7, pp. 14697–14701, 2014.
- [2] S. Aiswarya, A. G. Prince, and C. Dilip, "A review on use of metakaolin in concrete," *Engineering Science and Technology*, vol. 3, no. 3, pp. 592–597, 2013.
- [3] J. Ambroise, S. Maximilien, and J. Pera, "Properties of metakaolin blended cements," *Advanced Cement Based Materials*, vol. 1, no. 4, pp. 161–168, 1994.
- [4] J. M. Khatib, E. M. Negim, and E. Gjonbalaj, "High volume metakaolin as cement replacement in Mortar," *World Journal of Chemistry*, vol. 7, no. 1, pp. 7–10, 2012.
- [5] J. M. Justice, *Evaluation of Metakaolin for use as supplementary cementitious materials [M.S. thesis]*, The Academic Faculty, Georgia Institute of Technology, 2005.
- [6] E. Guneyisi, M. Gesoglu, S. Karaoglu, and K. Mermerdas, "Strength, permeability and shrinkage cracking of silica fume and metakaolin concretes," *Construction and Building Materials*, vol. 34, pp. 120–130, 2012.
- [7] D. W. Fowler, Ed., *Polymer Modified Concrete*, American Concrete Institute, Detroit, Mich, USA, 1987.
- [8] V. Bhikshma, K. J. Rao, and B. Balaji, "An experimental study on behavior of polymer cement concrete," *Asian Journal of Civil Engineering*, vol. 11, no. 5, pp. 563–573, 2010.
- [9] M. Jamshidi, H. R. Pakravan, and A. R. Pourkhorshidi, "Application of polymer admixtures to modify concrete properties: effects of polymer type and content," *Asian Journal of Civil Engineering*, vol. 15, no. 5, pp. 779–787, 2014.
- [10] W. J. Lewis and G. Lewis, "The influence of polymer latex modifiers on the properties of concrete," *Composites*, vol. 21, no. 6, pp. 487–494, 1990.
- [11] R. Wang, P.-M. Wang, and X.-G. Li, "Physical and mechanical properties of styrene-butadiene rubber emulsion modified cement mortars," *Cement and Concrete Research*, vol. 35, no. 5, pp. 900–906, 2005.
- [12] T. U. Ganiron Jr., "Influence of polymer fiber on strength of concrete," *International Journal of Advanced Science and Technology*, vol. 55, pp. 53–66, 2013.

## Research Article

# An Improved Micromechanical Framework for Saturated Concrete Repaired by the Electrochemical Deposition Method considering the Imperfect Bonding

Qing Chen,<sup>1,2</sup> Zhengwu Jiang,<sup>1</sup> Hehua Zhu,<sup>3,4</sup> J. Woody Ju,<sup>5</sup>  
Zhiguo Yan,<sup>3,4</sup> and Yaqiong Wang<sup>2</sup>

<sup>1</sup>Key Laboratory of Advanced Civil Engineering Materials, Ministry of Education, Tongji University, 4800 Cao'an Road, Shanghai 201804, China

<sup>2</sup>Shaanxi Provincial Major Laboratory for Highway Bridge and Tunnel, Chang'an University, Xi'an, Shaanxi 710064, China

<sup>3</sup>State Key Laboratory for Disaster Reduction in Civil Engineering, Tongji University, 1239 Siping Road, Shanghai 200092, China

<sup>4</sup>Key Laboratory of Geotechnical and Underground Engineering, Ministry of Education, Tongji University, 1239 Siping Road, Shanghai 200092, China

<sup>5</sup>Department of Civil and Environmental Engineering, University of California, Los Angeles, CA 90095, USA

Correspondence should be addressed to Zhengwu Jiang; [jzhw@tongji.edu.cn](mailto:jzhw@tongji.edu.cn)

Received 12 May 2016; Accepted 21 July 2016

Academic Editor: Song Han

Copyright © 2016 Qing Chen et al. This is an open access article distributed under the Creative Commons Attribution License, which permits unrestricted use, distribution, and reproduction in any medium, provided the original work is properly cited.

The interfaces between the deposition products and concrete are not always well bonded when the electrochemical deposition method (EDM) is adopted to repair the deteriorated concrete. To theoretically illustrate the deposition healing process by micromechanics for saturated concrete considering the imperfect interfaces, an improved micromechanical framework with interfacial transition zone (ITZ) is proposed based on our recent studies. In this extension, the imperfect bonding is characterized by the ITZ, whose effects are calculated by modifying the generalized self-consistent model. Meanwhile, new multilevel homogenization schemes are employed to predict the effective properties of repaired concrete considering the ITZ effects. Moreover, modification procedures are presented to reach the properties of repaired concrete with ITZs in the dry state. To demonstrate the feasibility of the proposed micromechanical model, predictions obtained via the proposed micromechanical model are compared with those of the existing models and the experimental data, including results from extreme states during the EDM healing process. Finally, the influences of ITZ and deposition product on the healing effectiveness of EDM are discussed based on the proposed micromechanical model.

## 1. Introduction

Over the past 20 years, many meaningful studies have been published on the electrochemical deposition method (EDM), which is a promising repairing approach for concrete in aqueous environment and has been applied to marine structures and other situations in which traditional repairing methods are limited [1–4]. The current literatures mainly focus on the experimental research, including specimen production [5–7], factors influencing the healing effectiveness of EDM [8–10], and assessments of the healing effectiveness of EDM [11–14]. However, there are few theoretical models pertaining

to mechanical properties during the EDM healing process. Recently, the authors present micromechanical frameworks to quantitatively describe the mechanical performance of EDM when it is used to heal cracked saturated concrete [15–18]. In these micromechanical models, the repaired saturated concrete is represented as three-phase composite composed of the intrinsic concrete, deposition products, and the water phase. During the healing process, the water phase will be replaced by the deposition products. Meanwhile, the effective medium methods, such as the self-consistent approach, the differential scheme, and the Mori-Tanaka method, are

adopted to estimate the effective properties of concrete during the healing process.

It is noted that the interfaces between the deposition products and the intrinsic concrete are assumed to be well bonded in previous models [15–18]. However, many experimental investigations have shown that the properties of the interfaces between the deposition products and the intrinsic concrete matrix are influenced by many factors, like the solution type and the current density [8–10, 12, 13], which implies that the perfect bonding assumption is not held reasonable all the time. In this extension, an improved micromechanical model is proposed by considering the imperfect bonding between the deposition product and the intrinsic concrete. The imperfect bonding is characterized by the interfacial transition zone (ITZ), whose effects are calculated by modifying the generalized self-consistent model. Instead of the effective medium method, the noninteraction solution of Ju and Chen [19] is modified to consider the effects of equivalent particle composed of water, deposition product, and ITZ. Meanwhile, new multilevel homogenization schemes considering the ITZ effects are employed to predict the effective properties of repaired concrete. Moreover, modification procedures are presented to reach the properties of repaired concrete with ITZ in the dry state.

Based on our recent works [15, 18], this paper presents an improved micromechanical framework to describe the healing process of saturated concrete considering the imperfect bonding between the deposition products and the concrete matrix. An outline of this paper is as follows: Section 2 illustrates the “noninteracting solutions” for the effective properties of two-phase composite. In Section 3, an improved micromechanical model is presented for the healed saturated concrete with imperfect bonding characterized by the ITZ. New multilevel homogenization procedures are proposed to estimate the effective properties of the healed concrete by taking the imperfect bonding into consideration in Section 4. Meanwhile, micromechanical procedures considering the ITZ effects are performed to modify the properties of repaired concrete in the dry state. Numerical examples including experimental validations and comparisons with existing micromechanical models are presented in Section 5, which also discusses the influences of the ITZ and deposition product on the healing effectiveness of EDM based on our proposed micromechanical framework. And some conclusions are reached in Section 6.

## 2. The “Noninteracting Solutions” for the Effective Properties of Two-Phase Composite

*2.1. The Effective Properties of the Composite.* One goal of continuum micromechanics is to estimate the effective elastic properties of the material defined on the representative volume element (RVE). The RVE is based on a “mesoscopic” length scale which is much larger than the characteristic length scale of particles (inhomogeneities) but smaller than the characteristic length scale of a macroscopic specimen [19]. Taking a two-phase composite as an example, the effective

elastic stiffness tensor  $\mathbf{C}_*$  of the composite is defined through the following:

$$\bar{\boldsymbol{\sigma}} = \mathbf{C}_* : \bar{\boldsymbol{\varepsilon}} \quad (1)$$

with

$$\begin{aligned} \bar{\boldsymbol{\sigma}} &\equiv \frac{1}{V} \int_V \boldsymbol{\sigma}(\mathbf{x}) d\mathbf{x} = \frac{1}{V} \left[ \int_{V_m} \boldsymbol{\sigma}(\mathbf{x}) d\mathbf{x} + \int_{V_i} \boldsymbol{\sigma}(\mathbf{x}) d\mathbf{x} \right], \\ \bar{\boldsymbol{\varepsilon}} &\equiv \frac{1}{V} \int_V \boldsymbol{\varepsilon}(\mathbf{x}) d\mathbf{x} = \frac{1}{V} \left[ \int_{V_m} \boldsymbol{\varepsilon}(\mathbf{x}) d\mathbf{x} + \int_{V_i} \boldsymbol{\varepsilon}(\mathbf{x}) d\mathbf{x} \right], \end{aligned} \quad (2)$$

where  $V$  is the volume of an RVE,  $V_m$  is the volume of the matrix, and  $V_i$  is the volume of the inhomogeneity.  $\bar{\boldsymbol{\varepsilon}}$  and  $\bar{\boldsymbol{\sigma}}$  are the volume-average strain and stress of the composite.

*2.2. The “Noninteracting Solutions” for the Effective Properties.* The effective stiffness tensor of two-phase composite containing spherical inhomogeneities can be derived through [19–21]

$$\mathbf{C}_* = [\mathbf{C}_m + \phi_i (\mathbf{C}_i - \mathbf{C}_m) : \mathbf{B}], \quad (3)$$

where  $\mathbf{C}_*$  is the effective elastic stiffness tensor of the composite;  $\mathbf{C}_m$  and  $\mathbf{C}_i$  are the elastic stiffness tensor of the matrix phase and the inhomogeneity, respectively;  $\mathbf{B}$  is the strain concentration tensor;  $\phi_i$  is the volume fraction of the inhomogeneity. According to our previous work, when the noninteraction solutions are considered, the “strain concentration tensor” can be defined through [21, 22]

$$\mathbf{B} = [(\mathbf{I} - \mathbf{S}\mathbf{H})(\mathbf{A} + \mathbf{S})\mathbf{A}]^{-1}, \quad (4)$$

with

$$\mathbf{H} = \phi_i (\mathbf{A} + \mathbf{S})^{-1}, \quad (5)$$

$$\mathbf{A} \equiv (\mathbf{C}_i - \mathbf{C}_m)^{-1} : \mathbf{C}_m, \quad (6)$$

where  $\mathbf{S}$  is Eshelby’s tensor, which depends on the properties of the matrix and the shape of the inclusions;  $\mathbf{I}$  defines the fourth-order isotropic identity tensor.

## 3. Micromechanical Model for Saturated Concrete Repaired Using EDM with the Imperfect Bonding

*3.1. The Micromechanical Approaches to Represent the Imperfect Bonding.* There are mainly two analytical models to represent the imperfect bonding between the inclusion phase and matrix phase [23–27]. One is the spring layer model, also known as the interface model, which involves a very thin interfacial zone of unspecified thickness [23–25]. The other is the interphase model, which describes the interfacial zone as a layer between particles and matrix of a specified thickness and of elastic constants different from those of the matrix and the particles [26, 27]. In this paper, the interphase model is utilized to represent the imperfect bonding between the deposition products and the intrinsic concrete matrix.

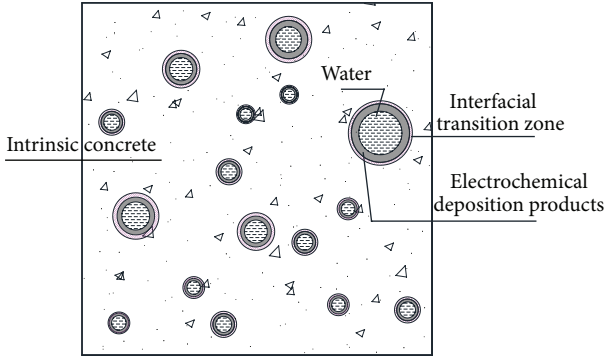


FIGURE 1: Micromechanical model for saturated concrete healed using EDM with interfacial transition zone (ITZ).

**3.2. Microstructure of Healed Saturated Concrete with ITZ.** The saturated concrete repaired by EDM is described as a multiphase composite composed of pores occupied by water, deposition products, mortar, coarse aggregates, and their interfaces [15–18]. The three traditional solid phases (i.e., mortar, coarse aggregates, and their interfaces) are merged into one matrix phase, namely, intrinsic concrete, in representative volume element [15–18]. Deposition products and water are considered as different inclusion phases in the saturated concrete. Furthermore, in this extension, the interfacial transition zone (ITZ) is considered with the interphase model to characterize the imperfect bonding phenomenon between the deposition product and the intrinsic concrete [8–10, 12, 13].

**3.3. Micromechanical Model for Saturated Concrete Healed Using EDM with the ITZ.** By representing the imperfect bonding with the ITZ, an improved micromechanical model for saturated concrete repaired by EDM can be proposed based on our previous work, which is exhibited in Figure 1. The matrix phase is the intrinsic concrete composed of mortar, coarse aggregates, and their interfaces. The inclusions contain the water, deposition products, and the ITZ. The saturated microcracks and microvoids in the concrete are supposed to be spheres, and the volume of the deposition product is assumed to be proportional to that of each spherical pore [15–18]. Since there is the ITZ in our proposed model, the healing process can be divided into two different stages, including the formation of ITZ and deposition product zone (DPZ). By predicting the effective properties of our model, the concrete's mechanical performance during the healing process is revealed theoretically and quantitatively.

## 4. Estimating the Effective Properties of Saturated Concrete Repaired Using EDM with ITZ

**4.1. Multilevel Homogenization Scheme for Estimating Effective Properties.** Previously published studies have shown that a homogenization stepping scheme is an effective way to obtain

the effective properties of multi-inclusion composites [28–41]. The multiphase micromechanical model used in the present study also employs a multilevel homogenization procedure. First, the equivalent inclusion is obtained by the first-level homogenization of the two-phase composite composed of water and deposition products, as shown in Figure 2. Second, the equivalent particle is attained by homogenizing the ITZ and the equivalent inclusion, as shown in Figure 3. Third, the effective properties of the equivalent homogeneous composite are calculated by the homogenization of the two-phase composite composed of equivalent particles and the intrinsic concrete matrix, as shown in Figure 4.

**4.2. The First-Level Homogenization for the Equivalent Inclusion Composed of Water and Deposition Products.** The three-phase sphere model presented by Christensen and Lo [42], that is, the generalized self-consistent model, is employed to conduct the first-level homogenization by modifying its inner- and outer-layer phases into the water phase and the deposition products, respectively. Let  $K_1$  and  $\mu_1$  ( $K_2$  and  $\mu_2$ ;  $K_F$  and  $\mu_F$ ) denote the bulk modulus and shear modulus of the water (deposition products and equivalent inclusions), respectively. The effective bulk modulus and shear modulus for the equivalent inclusion can be expressed by (7) and (8) as follows:

$$K_F = K_2 + \frac{\phi_{Fw} (K_1 - K_2) (3K_2 + 4\mu_2)}{3K_2 + 4\mu_2 + 3(1 - \phi_{Fw})(K_1 - K_2)}, \quad (7)$$

$$A \left( \frac{\mu_F}{\mu_2} \right)^2 + B \left( \frac{\mu_F}{\mu_2} \right) + C = 0, \quad (8)$$

with

$$\phi_{Fw} = \frac{V_{\text{wat}}}{V_{\text{wat}} + V_{\text{dep}}}, \quad (9)$$

where  $A$  and  $B$  are parameters depending on the properties of deposition product and water. See details for our previous work [15].  $\phi_{Fw}$  is the volume fraction of the water phase in the two-phase composite composed of the water and the deposition products,  $V_{\text{wat}}$  denotes the volume of the water, and  $V_{\text{dep}}$  signifies the volume of the deposition products.

**4.3. The Second-Level Homogenization for the Equivalent Particle Composed of the ITZ and the Equivalent Inclusion.** Let  $K_3$ ,  $\mu_3$ ,  $\nu_3$ , and  $V_{\text{itz}}$  represent the bulk modulus, shear modulus, Poisson's ratio, and volume of the ITZ and  $K_S$ ,  $\mu_S$  signify the bulk modulus and shear modulus of the equivalent particles made up of the ITZ and the equivalent inclusion.  $\phi_{\text{se}}$  is the volume fraction of the equivalent inclusion in the equivalent particle.  $K_S$  can be reached with (7) by replacing  $K_1$ ,  $K_2$ ,  $\mu_2$ ,  $\phi_{Fw}$ , and  $K_F$  with  $K_F$ ,  $K_3$ ,  $\mu_3$ ,  $\phi_{\text{se}}$ , and  $K_S$ , respectively.  $\mu_S$  can be similarly calculated by adopting Christensen and Lo's work [42] with the following expressions:

$$A' \left( \frac{\mu_S}{\mu_3} \right)^2 + B' \left( \frac{\mu_S}{\mu_3} \right) + C' = 0, \quad (10)$$

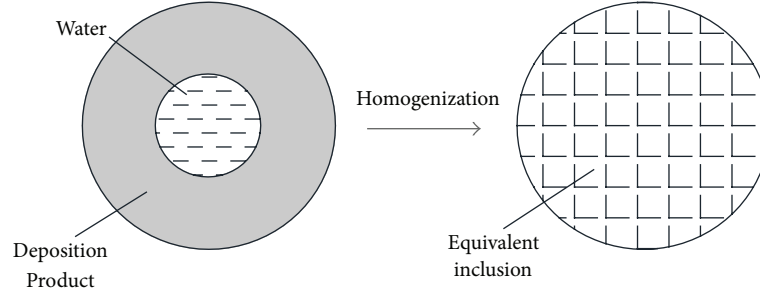


FIGURE 2: The equivalent inclusion obtained by the first-level micromechanical homogenization to the two-phase composite composed of the deposition products and water.

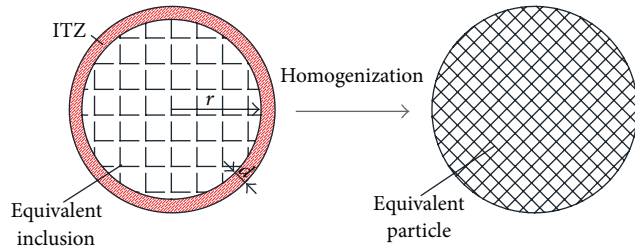


FIGURE 3: The equivalent particle attained by the second-level micromechanical homogenization to the two-phase composite made up of the ITZ and equivalent inclusion.

$$\begin{aligned}
 C' = & 4 \left[ \frac{\mu_F}{\mu_3} - 1 \right] (5\nu_3 - 7) \eta_\alpha \phi_{Se}^{10/3} \\
 & - 2 \left[ 63 \left( \frac{\mu_F}{\mu_3} - 1 \right) \eta_\beta + 2\eta_\alpha \eta_\gamma \right] \phi_{Se}^{7/3} \\
 & + 252 \left[ \frac{\mu_F}{\mu_3} - 1 \right] \eta_\beta \phi_{Se}^{5/3} \\
 & + 25 \left[ \frac{\mu_F}{\mu_3} - 1 \right] (\nu_3^2 - 7) \eta_\beta \phi_{Se} \\
 & - 3(7 + 5\nu_3) \eta_\beta \eta_\gamma,
 \end{aligned} \tag{11}$$

where

$$\begin{aligned}
 A' = & 8 \left[ \frac{\mu_F}{\mu_3} - 1 \right] (4 - 5\nu_3) \eta_\alpha \phi_{Se}^{10/3} \\
 & - 2 \left[ 63 \left( \frac{\mu_F}{\mu_3} - 1 \right) \eta_\beta + 2\eta_\alpha \eta_\gamma \right] \phi_{Se}^{7/3} \\
 & + 252 \left[ \frac{\mu_F}{\mu_3} - 1 \right] \eta_\beta \phi_{Se}^{5/3} \\
 & - 50 \left[ \frac{\mu_F}{\mu_3} - 1 \right] (7 - 12\nu_3 + 8\nu_3^2) \eta_\beta \phi_{Se} \\
 & + 4(7 - 10\nu_3) \eta_\beta \eta_\gamma, \\
 B' = & -4 \left[ \frac{\mu_F}{\mu_3} - 1 \right] (1 - 5\nu_3) \eta_\alpha \phi_{Se}^{10/3} \\
 & + 4 \left[ 63 \left( \frac{\mu_F}{\mu_3} - 1 \right) \eta_\beta + 2\eta_\alpha \eta_\gamma \right] \phi_{Se}^{7/3} \\
 & - 504 \left[ \frac{\mu_F}{\mu_3} - 1 \right] \eta_\beta \phi_{Se}^{5/3} \\
 & + 150 \left[ \frac{\mu_F}{\mu_3} - 1 \right] (3 - \nu_3) \nu_3 \eta_\beta \phi_{Se} \\
 & + 3(15\nu_3 - 7) \eta_\beta \eta_\gamma,
 \end{aligned}$$

with

$$\begin{aligned}
 \eta_\alpha = & \left[ \frac{\mu_F}{\mu_3} - 1 \right] (49 - 50\nu_F \nu_3) + 35 \left( \frac{\mu_F}{\mu_3} \right) (\nu_F - 2\nu_3) \\
 & + 35(2\nu_F - \nu_3), \\
 \eta_\beta = & 5\nu_F \left[ \frac{\mu_F}{\mu_3} - 8 \right] + 7 \left[ \frac{\mu_F}{\mu_3} + 4 \right], \\
 \eta_\gamma = & \frac{\mu_F}{\mu_3} [8 - 10\nu_3] + (7 - 5\nu_3), \\
 \phi_{Se} = & \frac{V_{wat} + V_{dep}}{V_{itz} + V_{dep} + V_{wat}},
 \end{aligned} \tag{12}$$

where  $V_{itz}$  denotes the volume of ITZ.

*4.4. The Third-Level Homogenization for the Equivalent Homogenous Composite Composed of the Equivalent Particle and Intrinsic Concrete.* The noninteraction solutions of [19] are adopted to get the effective properties of the repaired concrete. Let  $C_S$ ,  $C_4$ , and  $C_T$  represent the stiffness tensor of the equivalent particle, the intrinsic concrete, and the equivalent composite of the saturated concrete repaired by EDM with ITZ. For the isotropic matrix and spherical equivalent

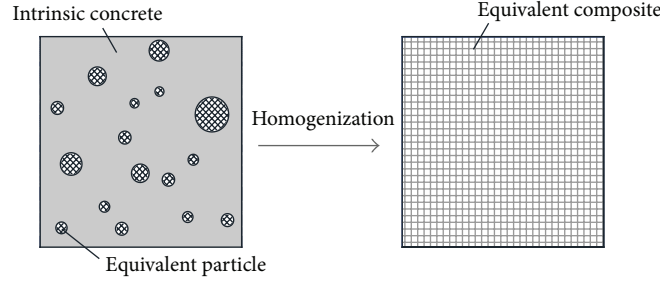


FIGURE 4: The equivalent composite of repaired concrete reached by the third-level micromechanical homogenization to the two-phase composite consisting of the intrinsic concrete and equivalent particle.

inclusions, the tensorial components of  $\mathbf{I}$ ,  $\mathbf{S}$ ,  $\mathbf{C}_S$ ,  $\mathbf{C}_4$ , and  $\mathbf{C}_T$  are as follows:

$$I_{ijkl} = \frac{1}{3}\delta_{ij}\delta_{kl} + \frac{1}{2}\left(\delta_{ik}\delta_{jl} + \delta_{il}\delta_{jk} - \frac{2}{3}\delta_{ij}\delta_{kl}\right),$$

$$S_{ijkl} = \frac{K_4}{3K_4 + 4G_4}\delta_{ij}\delta_{kl} + \frac{3(K_4 + 2G_4)}{5(3K_4 + 4G_4)}\left(\delta_{ik}\delta_{jl} + \delta_{il}\delta_{jk} - \frac{2}{3}\delta_{ij}\delta_{kl}\right), \quad (13)$$

$$C_{Sijkl} = K_S\delta_{ij}\delta_{kl} + \mu_S\left(\delta_{ik}\delta_{jl} + \delta_{il}\delta_{jk} - \frac{2}{3}\delta_{ij}\delta_{kl}\right),$$

$$C_{4ijkl} = K_4\delta_{ij}\delta_{kl} + \mu_4\left(\delta_{ik}\delta_{jl} + \delta_{il}\delta_{jk} - \frac{2}{3}\delta_{ij}\delta_{kl}\right),$$

$$C_{Tijkl} = K_T\delta_{ij}\delta_{kl} + \mu_T\left(\delta_{ik}\delta_{jl} + \delta_{il}\delta_{jk} - \frac{2}{3}\delta_{ij}\delta_{kl}\right),$$

where  $\delta_{ij}$  is the Kronecker delta.  $K_4$ ,  $\mu_4$  are, respectively, the bulk modulus and shear modulus of the intrinsic concrete, and  $K_T$ ,  $\mu_T$  are those of the equivalent composite of the saturated concrete repaired by EDM with ITZ, correspondingly. By replacing the matrix phase and inhomogeneities (inclusion phase) with the intrinsic concrete and the equivalent particle, the Ju and Chen model is modified to obtain the effective properties of the saturated concrete repaired by EDM with ITZ. By substituting (13) into (1)–(5), the effective bulk modulus and shear modulus of the saturated concrete repaired by EDM with ITZ are attained by the following equations after some derivations:

$$K_T = K_4 \left\{ 1 + \frac{3(1 - \nu_4)(K_S - K_4)\phi_{Tp}}{3(1 - \nu_4)K_4 + (1 - \phi_{Tp})(1 + \nu_4)(K_S - K_4)} \right\}, \quad (14)$$

$$\mu_T = \mu_4 \left\{ 1 + \frac{15(1 - \nu_4)(\mu_S - \mu_4)\phi_{Tp}}{15(1 - \nu_4)\mu_4 + (1 - \phi_{Tp})(8 - 10\nu_4)(\mu_S - \mu_4)} \right\},$$

with

$$\phi_{Tp} = \frac{V_{\text{wat}} + V_{\text{dep}} + V_{\text{itz}}}{V_{\text{wat}} + V_{\text{dep}} + V_{\text{itz}} + V_{\text{mat}}} = \frac{V_{\text{wat}} + V_{\text{dep}} + V_{\text{itz}}}{V_{\text{tot}}}, \quad (15)$$

where  $V_{\text{mat}}$  and  $V_{\text{tot}}$  mean the volume of the intrinsic concrete matrix and the total volume of the composite. With regard to the effect of water viscosity in pores of the saturated concrete [43–46],  $\mu_T$  should multiply the modification function as below [43]:

$$F = 1 + f_1\phi_{Tp}^2 + f_2\phi_{Tp}, \quad (16)$$

where  $f_1$  and  $f_2$  are parameters investigated by the experiment [43].

Furthermore, the Young modulus of unsaturated concrete can be obtained based on the theorem of elastic mechanics, provided that the bulk modulus and shear modulus are known. Hence,

$$E_T = \frac{9K_T\mu_T}{3K_T + \mu_T}, \quad (17)$$

where  $E_T$  is the Young modulus of the equivalent homogeneous composite (i.e., the healed saturated concrete).

**4.5. Modifications to Estimations of Effective Properties with ITZ in Dry Conditions.** Modifications should be made to our proposed framework when it is applied to estimate the properties of the saturated concrete repaired using EDM in the dry state [15].

Firstly, the properties pertaining to water should be replaced by those pertaining to air, and the water effect should be ignored. Secondly, since the pores should not be assumed to be spherical in the dry state, the similar modification coefficients,  $\chi_K$ ,  $\chi_\mu$ , and  $\chi_E$ , are introduced to reflect the influence of the crack (pore) shape in the following:

$$\chi_K = \frac{K_\alpha^*}{K_{\alpha=1}^*}$$

$$\chi_\mu = \frac{\mu_\alpha^*}{\mu_{\alpha=1}^*}$$

$$\chi_E = \frac{E_\alpha^*}{E_{\alpha=1}^*}$$

$$\alpha = \frac{1}{N} \sum_{i=1}^N \frac{a_i}{b_i},$$
(18)

where  $K_{\alpha=1}^*$ ,  $\mu_{\alpha=1}^*$ , and  $E_{\alpha=1}^*$  are the predicted effective bulk modulus, effective shear modulus, and Young's modulus, respectively, when the crack (pore) shape is spherical ( $\alpha = 1$ ). Moreover,  $K_\alpha^*$ ,  $\mu_\alpha^*$ , and  $E_\alpha^*$  are the predicted effective bulk modulus, effective shear modulus, and Young's modulus, respectively, when the pore shape is not spherical ( $\alpha < 1$ );  $\alpha$  is the equivalent aspect ratio of the pores;  $a_i$  and  $b_i$  are the lengths of the pores' minor and major axes, respectively; and  $N$  is the number of different pores in the concrete.

The results in [47] are modified to reach the above predicted effective properties. See details for [15]. However, due to the imperfect bonding effect,  $K_2$  and  $\mu_2$  in (37)–(43) of [15] should be replaced by  $K_{ave}$  and  $\mu_{ave}$ , which are obtained by the following expressions:

$$K_{ave} = 0.5 (\phi_{Md} K_2 + \phi_{Ml} K_3 + (1 - \phi_{Md} - \phi_{Ml}) K_4)$$

$$+ 0.5 \left( \frac{1}{(\phi_{Md}/K_2 + \phi_{Ml}/K_3 + (1 - \phi_{Md} - \phi_{Ml})/K_4)} \right),$$

$$\mu_{ave} = 0.5 (\phi_{Md} \mu_2 + \phi_{Ml} \mu_3 + (1 - \phi_{Md} - \phi_{Ml}) \mu_4)$$

$$+ 0.5 \left( \frac{1}{(\phi_{Md}/\mu_2 + \phi_{Ml}/\mu_3 + (1 - \phi_{Md} - \phi_{Ml})/\mu_4)} \right), \quad (19)$$

$$\phi_{Md} = \frac{V_{dep}}{V_{dep} + V_{itz} + V_{mat}},$$

$$\phi_{Ml} = \frac{V_{itz}}{V_{dep} + V_{itz} + V_{mat}}.$$

Furthermore, if ultrasound waves are employed to test the effective dynamic properties under dry conditions, the static properties should be modified to dynamic properties according to the relationship between them [15, 48].

## 5. Verification and Discussion

**5.1. Comparison with the Existing Model and EDM Experiments under Dry Conditions.** The predictions in this study are compared with the experimental data and the estimations of the existing models to verify the capacity of the proposed micromechanical framework for saturated concrete repaired by the EDM considering the imperfect bonding.

Firstly, the existing models [15] are utilized to verify our proposed micromechanical framework. The properties of intrinsic concrete and deposition products are from [15]. Four different types of ITZ properties are utilized as examples to perform the simulations, which are listed in Table 1. The ratio between the volume of ITZ and equivalent inclusion is 0.1. It is noted that the specific values for the thicknesses and properties of the ITZs are not our central focus here. In this

TABLE 1: Properties of four types of ITZs between the deposition products inclusion and the concrete.

	Bulk modulus (GPa)	Shear modulus (GPa)
Type 1	18.61	12.3
Type 2	18.61 * 0.8	12.3 * 0.8
Type 3	18.61 * 0.4	12.3 * 0.4
Type 4	18.61 * 0.2	12.3 * 0.2

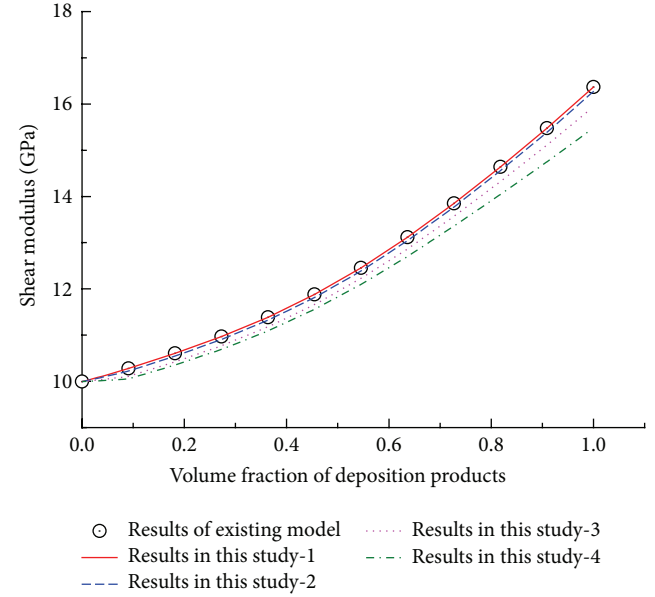


FIGURE 5: Comparisons of shear modulus between our predictions and those of existing model [15] during healing process, with 1, 2, 3, and 4 representing results obtained with the first, second, third, and fourth types of ITZ.

paper, we instead focus on the quantitative influence of the specified ITZs on the healing effects.

Figure 5 presents the comparisons of mechanical properties between our predictions and those of Zhu et al. [15] during healing process. From Figure 5, it can be observed that our predictions for shear modulus of repaired concrete are the same as those of Zhu et al. [15], when the properties of ITZ are equal to those of the deposition products, which implies that our proposed micromechanical model is capable of describing the healing process of saturated concrete with perfect interface. With the decrease of the IZT properties, the healed specimen demonstrates lower properties. Meanwhile, the results of the two different micromechanical models show that the values of effective shear modulus gradually increase during the healing process due to the accumulation of deposition products. As to the effective Young modulus, similar conclusions can be reached, which are exhibited by Figure 6.

Secondly, the dynamic Young moduli of the specimen before and after healing in Chen's experiment [14] are adopted to validate the proposed micromechanical model with ITZ in the dry state. The average initial porosity of the specimen is 0.299. The average pulse-velocity of its intrinsic concrete is

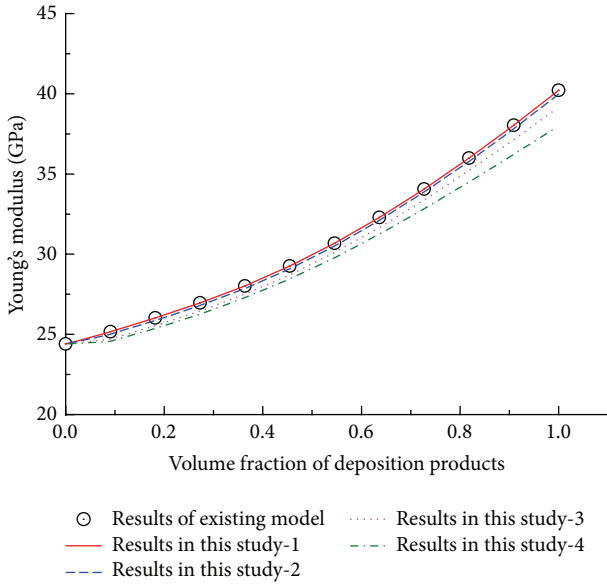


FIGURE 6: Comparisons of Young's modulus between our predictions and those of existing model [15] during healing process, with 1, 2, 3, and 4 representing results obtained with the first, second, third, and fourth types of ITZ.

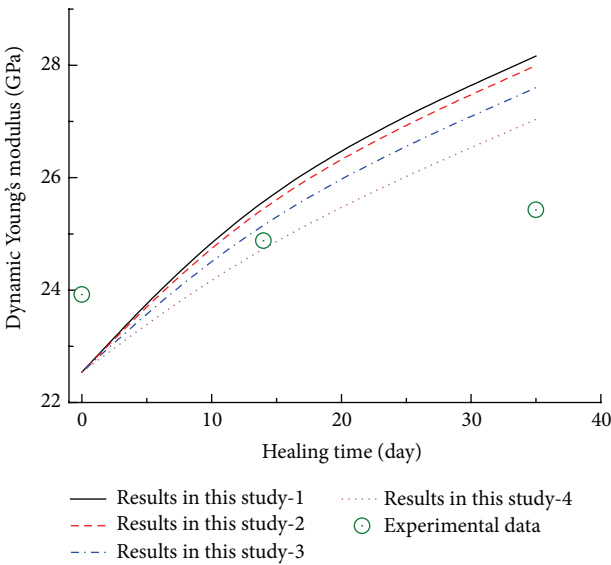


FIGURE 7: Comparison between the results obtained with the proposed model and those obtained experimentally [14] for the dynamic Young modulus in the dry state, with 1, 2, 3, and 4 representing results obtained with the first, second, third, and fourth types of ITZ.

5134.5 m/s. The density is 2537.9 kg/m<sup>3</sup> and Poisson's ratio is 0.229. As exhibited in Figure 7, the predictions considering the ITZ effects (i.e., results obtained with type 2, 3, and 4 ITZ properties) correspond better with the experimental data than those without taking ITZ effects into consideration (i.e., results reached with type 1 ITZ properties).

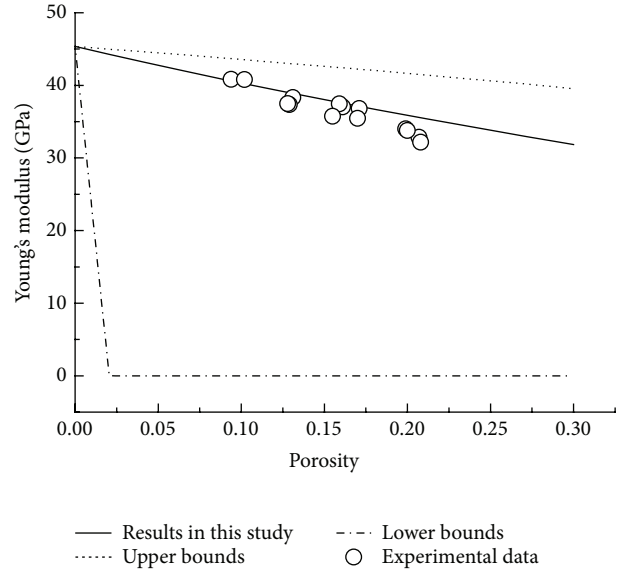


FIGURE 8: The comparison between the results obtained with the different micromechanical models and those obtained experimentally [48] for the static Young modulus of saturated concrete.

Thirdly, if there is absolutely no healing process in the concrete, the proposed model can predict the properties of the saturated concrete. Figure 8 exhibits the comparisons among our results, those obtained by the upper bounds, lower bounds, and the experimental data of Yaman et al. [48]. The comparisons show that the predictions herein agree well with the experimental data. In addition, if the saturated concrete has been completely healed by the EDM, there is no water effect and the healed concrete is effectively a two-phase composite with isotropic spherical inclusion phase with imperfect interfacial bonds. Furthermore, if the properties of ITZ are the same as those of inclusions, which implies that there are perfect interfaces between the inclusions and matrix, the proposed model can predict the two-phase composite with isotropic spherical inclusion phase. The work done by Cohen and Ishai [49] is employed to verify our proposed model at this state. Figures 9-10 present the comparisons among our results, the upper bounds, lower bounds, and the experimental data of Cohen and Ishai [49]. From Figures 9 and 10, it can be found that our predictions correspond with the experimental data well.

**5.2. Influences of ITZ Thickness and Electrochemical Deposition Product on the Healing Effectiveness.** The ITZ has a significant impact on the effective properties of the composite [23–27]. The volume fraction of ITZ in the equivalent particle can be represented as  $\phi_{ITZ} = 1 - (r/(r + d))^3$  from Figure 3, where  $d$  is the ITZ thickness. Since we focus on the quantitative influence of ITZ on the healing effectiveness of EDM, the exact value for  $d$  or  $\phi_{ITZ}$  is not the interest of this study. To investigate these effects quantitatively, three different values of  $\phi_{ITZ}$ , that is, 0.01, 0.1, and 0.2, are employed as examples. Figures 11 and 12 present the variations in the shear modulus and Young's modulus of the equivalent composite

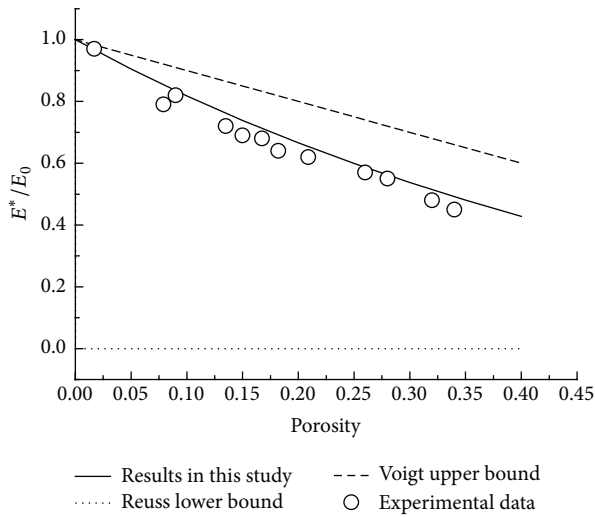


FIGURE 9: The comparison among the results obtained with the proposed micromechanical model, those obtained experimentally [49], those estimated by the Reuss lower bound, and the Voigt upper bound for the effective Young modulus of the porous matrix.

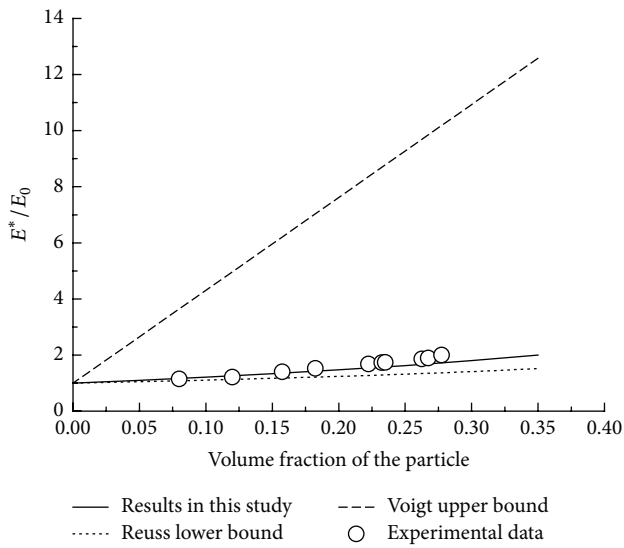


FIGURE 10: The comparison among the results obtained with the proposed micromechanical model, those obtained experimentally [49], those estimated by the Reuss lower bound, and the Voigt upper bound for the effective Young modulus of the nonporous composite.

of the healed saturated concrete with imperfect bonding. The properties of the equivalent composite gradually increase during the healing process. Furthermore, with the increase of the ITZ thickness, the equivalent composite demonstrates lower effective properties.

In addition, three types of deposition products from [15] are utilized as examples to illustrate their influence on the healing effectiveness. In these simulations,  $\phi_{ITZ} = 0.1$ . From Figure 13, it can be observed that the effective Young modulus increases during the healing process. Before the point of  $\phi_{ITZ} = 0.1$ , the improvement of Young's modulus is less than

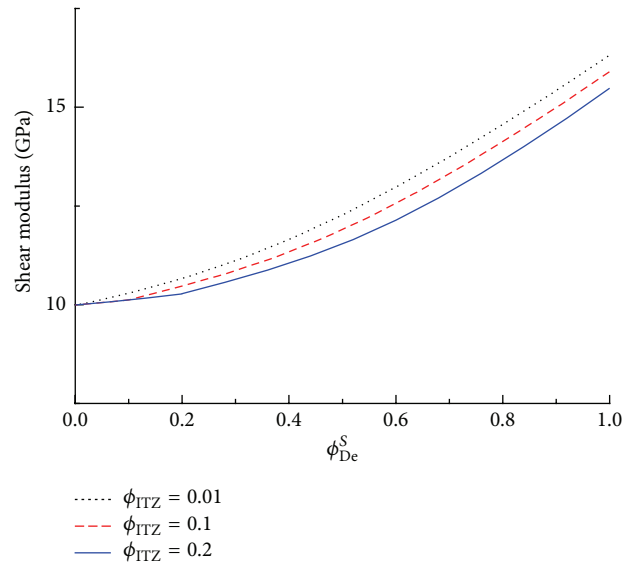


FIGURE 11: Influence of the ITZ on the shear modulus of repaired concrete during the healing process, where  $\phi_{ITZ}$  is the volume fraction of ITZ in the equivalent particle;  $\phi_{De}^S$  is the volume fraction of the deposition products in the equivalent particle.

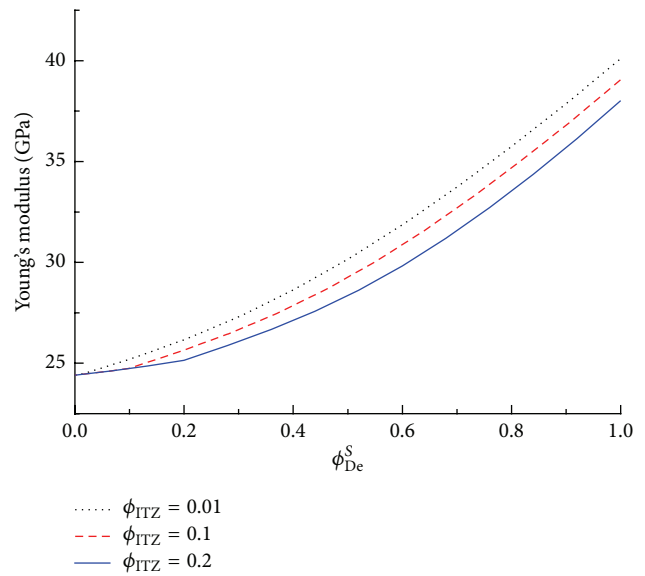


FIGURE 12: Influence of the ITZ on the Young modulus of repaired concrete during the healing process, where  $\phi_{ITZ}$  is the volume fraction of ITZ in the equivalent particle;  $\phi_{De}^S$  is the volume fraction of the deposition products in the equivalent particle.

those in the period after that point, because the properties of ITZ are smaller than those of DPZ. When the properties of the deposition products increase, the Young modulus of healed concrete becomes greater. As to the effective shear modulus, similar conclusions can be reached as Figure 14 shows.

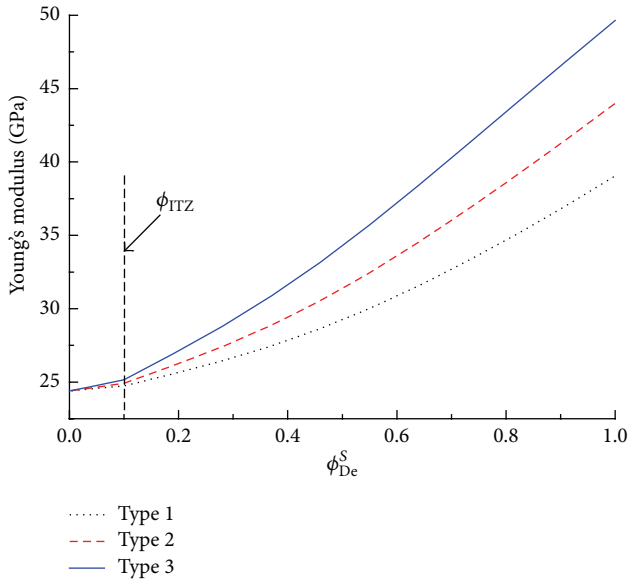


FIGURE 13: Influence of the properties of the deposition products on the Young modulus of repaired concrete during the healing process, where  $\phi_{ITZ}$  is the volume fraction of ITZ in the equivalent particle;  $\phi_{De}^S$  is the volume fraction of the deposition products in the equivalent particle.

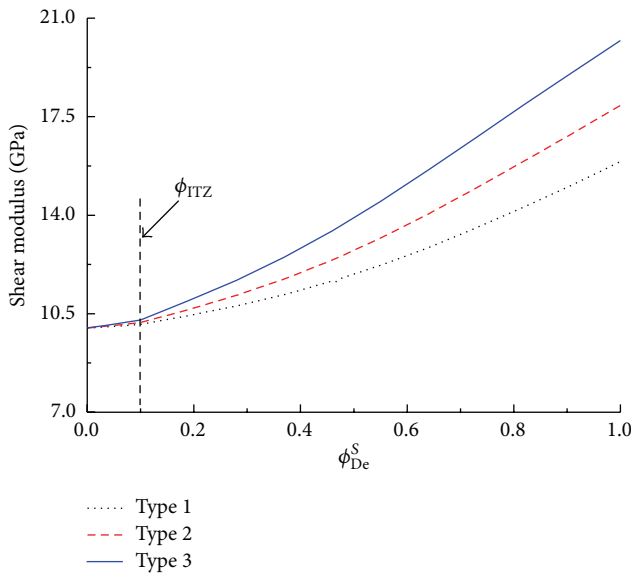


FIGURE 14: Influence of the properties of the deposition products on the shear modulus of repaired concrete during the healing process, where  $\phi_{ITZ}$  is the volume fraction of ITZ in the equivalent particle;  $\phi_{De}^S$  is the volume fraction of the deposition products in the equivalent particle.

## 6. Conclusions

The bonds between the deposition products and concrete are not always perfect when the electrochemical deposition method (EDM) is applied to repair the deteriorated concrete. As an extension of our recent studies, this paper proposes an improved micromechanical model with ITZ to theoretically

illustrate the deposition healing process by micromechanics and quantitatively describe the effective properties of saturated concrete repaired by EDM considering the imperfect bonding. To quantitatively consider the ITZ effects, a new multilevel homogenization scheme is proposed by incorporating the generalized self-consistent method and the noninteracting solutions of Ju and Chen's model together. Modification procedures are presented to obtain the properties of repaired concrete with ITZs in the dry state. Moreover, our predicted results are compared to available experimental data and the predictions of existing micromechanical models. The influences of the ITZ and deposition products on the healing effectiveness are discussed based on the proposed micromechanical model. From this study, the following main conclusions can be drawn:

- (1) The proposed micromechanical model with ITZ is both feasible and capable of describing the mechanical performance of saturated concrete during the EDM healing process with imperfect bonding.
- (2) For the special cases, the proposed model can predict the properties of saturated concrete repaired by EDM with perfect bonding, the properties of saturated concrete, and particle reinforced composite.
- (3) Based on our proposed model, the ITZ and deposition products play important roles in the healing effectiveness of EDM.

## Competing Interests

The authors declare that there are no competing interests regarding the publication of this paper.

## Acknowledgments

This work is supported by the National Key Basic Research and Development Program (973 Program, no. 2011CB013800) and National Natural Science Foundation of China (51508404, 51478348, 51278360, and 51308407). This work is also supported by Key Laboratory of Advanced Civil Engineering Materials (Tongji University), Program of Shanghai Science and Technology Commission (15DZ1205003), the 1000 Talents Plan Short-Term Program by the Organization Department of the Central Committee of the CPC, Research Program of State Key Laboratory for Disaster Reduction in Civil Engineering, the Scientific Platform Open Funds of Fundamental Research Plan for the Central Universities, Chang'an University (310821151113), and Natural Science Foundation of Shandong Province (ZR2013EEL019).

## References

- [1] M. Yokoda and T. Fukute, "Rehabilitation and protection of marine concrete structure using electrodeposition method," in *Proceedings of the International RILEM/CSIRO/ACRA Conference on Rehabilitation of Concrete Structures (RILEM '92)*, pp. 213–222, Melbourne, Australia, 1992.

- [2] H. Sasaki and M. Yokoda, "Repair method of marine reinforced concrete by electro deposition technique," in *Proceedings of the Annual Conference of Japanese Concrete Institute*, pp. 849–854, 1992.
- [3] Z. W. Jiang, W. T. Li, and Z. C. Yuan, "Influence of mineral additives and environmental conditions on the self-healing capabilities of cementitious materials," *Cement and Concrete Composites*, vol. 57, pp. 116–127, 2015.
- [4] W. T. Li, Z. W. Jiang, Z. H. Yang, N. Zhao, and W. Z. Yuan, "Self-healing efficiency of cementitious materials containing microcapsules filled with healing adhesive: mechanical restoration and healing process monitored by water absorption," *PLoS ONE*, vol. 8, no. 11, Article ID e81616, 2013.
- [5] J. S. Ryu, "New waterproofing technique for leaking concrete," *Journal of Materials Science Letters*, vol. 22, no. 14, pp. 1023–1025, 2003.
- [6] J. S. Ryu and N. Otsuki, "Experimental study on repair of concrete structural members by electrochemical method," *Scripta Materialia*, vol. 52, no. 11, pp. 1123–1127, 2005.
- [7] J.-J. Chang, W. Yeih, H.-M. Hsu, and N.-M. Huang, "Performance evaluation of using electrochemical deposition as a repair method for reinforced concrete beams," *Structural Longevity*, vol. 1, no. 2, pp. 75–93, 2009.
- [8] N. Otsuki and J.-S. Ryu, "Use of electrodeposition for repair of concrete with shrinkage cracks," *Journal of Materials in Civil Engineering*, vol. 13, no. 2, pp. 136–142, 2001.
- [9] J. S. Ryu, "Influence of crack width, cover depth, water–cement ratio and temperature on the formation of electrodeposits on the concrete surface," *Magazine of Concrete Research*, vol. 55, no. 1, pp. 35–40, 2003.
- [10] H.-Q. Chu and L.-H. Jiang, "Correlation analysis between concrete parameters and electrodeposition effect based on grey theory," *Journal of Wuhan University of Technology*, vol. 31, no. 7, pp. 22–26, 2009.
- [11] N. Otsuki, M. Hisada, J. S. Ryu, and E. J. Banshoya, "Rehabilitation of concrete cracks by electrodeposition," *Concrete International*, vol. 21, no. 3, pp. 58–62, 1999.
- [12] J.-S. Ryu and N. Otsuki, "Crack closure of reinforced concrete by electrodeposition technique," *Cement and Concrete Research*, vol. 32, no. 1, pp. 159–164, 2002.
- [13] Z. Jiang, F. Xing, Z. Sun, and P. Wang, "Healing effectiveness of cracks rehabilitation in reinforced concrete using electrodeposition method," *Journal Wuhan University of Technology, Materials Science Edition*, vol. 23, no. 6, pp. 917–922, 2008.
- [14] Q. Chen, *The stochastic micromechanical models of the multi-phase materials and their applications for the concrete repaired by electrochemical deposition method [Ph.D. thesis]*, Tongji University, Shanghai, China, 2014.
- [15] H. Zhu, Q. Chen, Z. Yan, J. W. Ju, and S. Zhou, "Micromechanical models for saturated concrete repaired by the electrochemical deposition method," *Materials and Structures/Materiaux et Constructions*, vol. 47, no. 6, pp. 1067–1082, 2014.
- [16] Q. Chen, H. Zhu, Z. Yan, T. Deng, and S. Zhou, "Micro-scale description of saturated concrete repaired by electrochemical deposition method based on Mori-Tanaka method," *Journal of Building Structures*, vol. 36, no. 1, pp. 98–103, 2015.
- [17] Q. Chen, H. H. Zhu, Z. G. Yan, J. W. Ju, T. Deng, and S. Zhou, "Micro-scale description of the saturated concrete repaired by electrochemical deposition method based on self-consistent method," *Chinese Journal of Theoretical and Applied Mechanics*, vol. 47, no. 2, pp. 367–371, 2015.
- [18] Q. Chen, Z. W. Jiang, Z. H. Yang et al., "Differential-scheme based micromechanical framework for saturated concrete repaired by the electrochemical deposition method," *Materials and Structures*, vol. 49, no. 12, pp. 5183–5193, 2016.
- [19] J. W. Ju and T. M. Chen, "Micromechanics and effective moduli of elastic composites containing randomly dispersed ellipsoidal inhomogeneities," *Acta Mechanica*, vol. 103, no. 1–4, pp. 103–121, 1994.
- [20] T. Mura, *Micromechanics of Defects in Solids*, Martinus Nijhoff, The Hague, Netherlands, 1987.
- [21] J. M. Qu and M. Cherkaoui, *Fundamentals of Micromechanics of Solids*, John Wiley & Sons, Hoboken, NJ, USA, 2006.
- [22] Q. Chen, H. H. Zhu, J. W. Ju et al., "A stochastic micromechanical model for multiphase composites containing spherical inhomogeneities," *Acta Mechanica*, vol. 226, no. 6, pp. 1861–1880, 2015.
- [23] J. Qu, "Eshelby tensor for an elastic inclusion with slightly weakened interface," *Journal of Applied Mechanics*, vol. 60, no. 4, pp. 1048–1050, 1993.
- [24] J. Qu, "The effect of slightly weakened interfaces on the overall elastic properties of composite materials," *Mechanics of Materials*, vol. 14, no. 4, pp. 269–281, 1993.
- [25] K. Yanase and J. W. Ju, "Effective elastic moduli of spherical particle reinforced composites containing imperfect interfaces," *International Journal of Damage Mechanics*, vol. 21, no. 1, pp. 97–127, 2012.
- [26] S. H. Nie and C. Basaran, "A micromechanical model for effective elastic properties of particulate composites with imperfect interfacial bonds," *International Journal of Solids and Structures*, vol. 42, no. 14, pp. 4179–4191, 2005.
- [27] Q. Chen, M. M. Nezhad, Q. Fisher, and H. H. Zhu, "Multi-scale approach for modeling the transversely isotropic elastic properties of shale considering multi-inclusions and interfacial transition zone," *International Journal of Rock Mechanics and Mining Sciences*, vol. 84, pp. 95–104, 2016.
- [28] Z. G. Yan, Q. Chen, H. H. Zhu, J. W. Ju, S. Zhou, and Z. W. Jiang, "A multi-phase micromechanical model for unsaturated concrete repaired using the electrochemical deposition method," *International Journal of Solids and Structures*, vol. 50, no. 24, pp. 3875–3885, 2013.
- [29] G. Q. Li, Y. Zhao, and S.-S. Pang, "Four-phase sphere modeling of effective bulk modulus of concrete," *Cement and Concrete Research*, vol. 29, no. 6, pp. 839–845, 1999.
- [30] N. B. Nguyen, A. Giraud, and D. Grgic, "A composite sphere assemblage model for porous oolitic rocks," *International Journal of Rock Mechanics and Mining Sciences*, vol. 48, no. 6, pp. 909–921, 2011.
- [31] J. W. Ju and T. M. Chen, "Effective elastic moduli of two-phase composites containing randomly dispersed spherical inhomogeneities," *Acta Mechanica*, vol. 103, no. 1–4, pp. 123–144, 1994.
- [32] J. W. Ju and X. D. Zhang, "Micromechanics and effective transverse elastic moduli of composites with randomly located aligned circular fibers," *International Journal of Solids and Structures*, vol. 35, no. 9–10, pp. 941–960, 1998.
- [33] J. W. Ju and L. Z. Sun, "A novel formulation for the exterior-point Eshelby's tensor of an ellipsoidal inclusion," *Journal of Applied Mechanics*, vol. 66, no. 2, pp. 570–574, 1999.
- [34] J. W. Ju and L. Z. Sun, "Effective elastoplastic behavior of metal matrix composites containing randomly located aligned

- spheroidal inhomogeneities. Part I: micromechanics-based formulation,” *International Journal of Solids and Structures*, vol. 38, no. 2, pp. 183–201, 2001.
- [35] J. W. Ju and K. Yanase, “Micromechanics and effective elastic moduli of particle-reinforced composites with near-field particle interactions,” *Acta Mechanica*, vol. 215, no. 1–4, pp. 135–153, 2010.
- [36] J. W. Ju and K. Yanase, “Micromechanical effective elastic moduli of continuous fiber-reinforced composites with near-field fiber interactions,” *Acta Mechanica*, vol. 216, no. 1–4, pp. 87–103, 2011.
- [37] L. Z. Sun and J. W. Ju, “Effective elastoplastic behavior of metal matrix composites containing randomly located aligned spheroidal inhomogeneities. Part II: applications,” *International Journal of Solids and Structures*, vol. 38, no. 2, pp. 203–225, 2001.
- [38] L. Z. Sun and J. W. Ju, “Elastoplastic modeling of metal matrix composites containing randomly located and oriented spheroidal particles,” *Journal of Applied Mechanics*, vol. 71, no. 6, pp. 774–785, 2004.
- [39] H. H. Zhu, Q. Chen, J. W. Ju et al., “Maximum entropy-based stochastic micromechanical model for a two-phase composite considering the inter-particle interaction effect,” *Acta Mechanica*, vol. 226, no. 9, pp. 3069–3084, 2015.
- [40] Q. Chen, H. H. Zhu, Z. G. Yan, J. W. Ju, Z. W. Jiang, and Y. Q. Wang, “A multiphase micromechanical model for hybrid fiber reinforced concrete considering the aggregate and ITZ effects,” *Construction and Building Materials*, vol. 114, pp. 839–850, 2016.
- [41] M. Mousavi Nezhad, H. H. Zhu, J. W. Ju, and Q. Chen, “A simplified multiscale damage model for the transversely isotropic shale rocks under tensile loading,” *International Journal of Damage Mechanics*, vol. 25, no. 5, pp. 705–726, 2016.
- [42] R. M. Christensen and K. H. Lo, “Solutions for effective shear properties in three phase sphere and cylinder models,” *Journal of the Mechanics and Physics of Solids*, vol. 27, no. 4, pp. 315–330, 1979.
- [43] H. L. Wang and Q. B. Li, “Prediction of elastic modulus and Poisson’s ratio for unsaturated concrete,” *International Journal of Solids and Structures*, vol. 44, no. 5, pp. 1370–1379, 2007.
- [44] Z.-W. Jiang, W.-T. Li, Z.-L. Deng, and Z.-G. Yan, “Experimental investigation of the factors affecting accuracy and resolution of the pore structure of cement-based materials by thermoporometry,” *Journal of Zhejiang University: Science A*, vol. 14, no. 10, pp. 720–730, 2013.
- [45] Z. W. Jiang, Z. P. Sun, and P. M. Wang, “Internal relative humidity distribution in high-performance cement paste due to moisture diffusion and self-desiccation,” *Cement and Concrete Research*, vol. 36, no. 2, pp. 320–325, 2006.
- [46] Z. W. Jiang, Z. P. Sun, and P. M. Wang, “Autogenous relative humidity change and autogenous shrinkage of high-performance cement pastes,” *Cement and Concrete Research*, vol. 35, no. 8, pp. 1539–1545, 2005.
- [47] J. G. Berryman, “Long-wave propagation in composite elastic media II. Ellipsoidal inclusion,” *Journal of the Acoustical Society of America*, vol. 68, no. 6, pp. 1820–1831, 1980.
- [48] I. O. Yaman, N. Hearn, and H. M. Aktan, “Active and non-active porosity in concrete—part I: experimental evidence,” *Materials and Structures/Materiaux et Constructions*, vol. 35, article 102, 2002.
- [49] L. Cohen and O. Ishai, “The elastic properties of three-phase composites,” *Journal of Composite Materials*, vol. 1, no. 4, pp. 390–403, 1967.